DIPLOMARBEIT

Identifying Viable Experimental Configurations for the Study of Correlated Electron-Photon Pairs in the Transmission Electron Microscope

zur Erlangung des akademischen Grades

Diplom-Ingenieur

im Rahmen des Studiums

Technische Physik

eingereicht von

Alexander Preimesberger
Matrikelnummer 01427641

durchgeführt am Atominstitut der Fakultät für Physik der Technischen Universität Wien

unter der Anleitung von

Assoz. Prof. Dr.rer.nat. Philipp Haslinger

Wien, 22.August 2023

Alexander Preimesberger Philipp Haslinger

Die approbierte gedruckte Originalversion dieser Diplomarbeit ist an der TU Wien Bibliothek verfügbar
The approved original version of this thesis is available in print at TU Wien Bibliothek.
TU Bibliothek Your knowledge hub

Abstract

Cathodoluminescence (CL) is the emission of light from a material, induced by the interaction with an incident electron. Setups for measuring it inside a transmission electron microscope allow for simultaneous measurements of both emitted CL photons and the transmitted electrons that produced them on a single particle level. Due to energy and momentum conservation, it is clear that each emitted photon corresponds to an energy loss and a momentum transfer to the electron.
Recent improvements in direct electron detectors, in particular those that use the ASIC Timepix3 are making it possible to study coherent CL on an event by event basis. This means that one can detect an individual electron and the individual photon it emits by verifying that they have been detected at the same time. One can consequently perform measurements on both particles.
In this work the key requirements, which are needed to do experiments in the single electron-single photon regime are outlined. An experimental investigation of four different setups concerning their suitability to this kind of experiment is presented: the thin film, the multi-slit mask, the bulk under aloof excitation and the microsphere under aloof excitation. Finally, in-detail measurements regarding the thin film are laid out, as this approach seems to be the most promising for future experiments as part of the ongoing Quantum Optics with Electron-Photon Pairs (QOEPP) project.

Die approbierte gedruckte Originalversion dieser Diplomarbeit ist an der TU Wien Bibliothek verfügbar
The approved original version of this thesis is available in print at TU Wien Bibliothek.
TU WIEN Bibliothek Your knowledge hub

Contents

1. Introduction 1

2. Electron Microscopy Fundamentals 3
2.1. Beam Formation . . . 3
2.2. Electron-Sample Interaction . . . 7
2.2.1. Inelastic Scattering . . . 8
2.2.2. Elastic Scattering and Imaging . . . 11

3. Measurement Setup 15
3.1. Electron Detection . . . 15
3.2. Electron Energy Loss . . . 20
3.3. Photon Collection . . . 21
3.4. Measurement Configurations . . . 23

4. Cathodoluminescence 24
4.1. The Cherenkov Effect . . . 26
4.1.1. Cherenkov Emission in the Wave Picture . . . 28
4.1.2. Energy and Momentum Conservation for Cherenkov Radiation 29
4.1.3. Photon Emission Probability . . . 31
4.2. Electron Recoil . . . 33
4.3. Distribution of Electron Recoil . . . 34

5. Coincidence Measurements 38
5.1. Average Rates . . . 40
5.2. Temporal Distributions . . . 41
5.3. Signal to Noise Ratio in Coincidence Measurements . . . 43
5.4. Correlations . . . 45

6. Cherenkov in Complex Geometries 47
6.1. Thin Membranes . . . 47
6.2. Aloof Configurations . . . 48

7. Momentum Measurement in a Thin Membrane - Limitations and Sources of Error 53
7.1. Initial Momentum Distribution . . . 53

Die approbierte gedruckte Originalversion dieser Diplomarbeit ist an der TU Wien Bibliothek verfügbar
The approved original version of this thesis is available in print at TU Wien Bibliothek.
TU WIEN Bibliothek Your knowledge hub

7.2. Elastic Scattering 55
7.3. Inelastic Scattering 55
7.4. Example: SNR of a Coincidence Measurement 57

8. Thin Specimen **62**
8.1. Thin Silicon Nitride 62
8.2. Thin Mica 65
8.3. Thin Crystalline Silicon 68

9. Further Setups **76**
9.1. Microspheres 76
9.2. Aloof Experiments 78
9.3. Multi-slit Masks 85

10. Conclusion and Outlook **89**

Bibliography **i**

A. Reciprocal Space **vii**

Die approbierte gedruckte Originalversion dieser Diplomarbeit ist an der TU Wien Bibliothek verfügbar
The approved original version of this thesis is available in print at TU Wien Bibliothek.
TU WIEN Bibliothek Your knowledge hub

Die approbierte gedruckte Originalversion dieser Diplomarbeit ist an der TU Wien Bibliothek verfügbar
The approved original version of this thesis is available in print at TU Wien Bibliothek.

1. Introduction

Cathodoluminescence (CL) has been studied since the first discovery of cathode rays in 1859 [1]: an electron impinging on a sample causes the emission of visible light, the spectrum of this light is characteristic for the material of the sample. In transmission electron microscopy, electrons penetrate the sample and are consequently imaged onto a detector using electron optics. The deflection of the electron by the sample, as well as the energy the electron looses to the sample, provide information on the samples structure and composition. The combination of these two techniques, i.e. measuring CL within the electron microscope, allows for the analysis of optical properties with sub-micrometer precision, which is extensively used in nanoscience and semiconductor research [2]. Less prominently, when used in a scanning transmission electron microscopy (STEM) configuration, this technique can collect CL photons while also measuring the transmitted electrons these photons originate from. This enabled researchers to correlate measurements on the emitted photons with measurements on the transmitted electrons. Due to energy and momentum conservation it is clear that each emitted photon corresponds to an energy loss and a momentum transfer to the electron and there have been a multitude of exciting works studying this connection [3][4][5][6].

In the past, most of these works studied correlations in aggregates of many electrons and photons: One would for example gather an electron energy loss spectrum made up of billions of electrons and a CL spectrum made up of millions of photons and find correlations between them. Recent improvements in electron detection, provided by direct electron detectors in general and the introduction of time resolution in cameras that use the ASIC Timepix3 in particular, are making it possible to study coherent CL on an event by event basis. This means that one can detect an individual electron and the individual photon it emits by verifying that they have been detected within a short enough time interval. In recent years this technique has been employed to resolve excitation lifetimes [6], suppress background in core loss EELS [7] and suppress noise in optical mode imaging [8].

The goal of Professor Haslinger's Quantum Optics with Electron Photon Pairs (QOEPP) project (supported by the Austrian Science Fund FWF under project number P 36041) is to leverage the ability to investigate correlated individual events in order to unveil new phenomena and open up an avenue to electron-photon coincidence experiments inspired by the quantum optics of photon-pairs. The first goal in this endeavor is to implement a scheme for the verification of

Die approbierte gedruckte Originalversion dieser Diplomarbeit ist an der TU Wien Bibliothek verfügbar
The approved original version of this thesis is available in print at TU Wien Bibliothek.
TU WIEN Bibliothek Your knowledge hub

entanglement of the electron and the photon.
In this work I will outline some key requirements, which are needed to do experiments in the single electron-single photon regime and I will present my investigation of four different setups concerning their suitability to this kind of experiment: the thin film, the multi-slit mask, the bulk under aloof excitation and the microsphere under aloof excitation. Finally, in-detail measurements regarding the thin film will be laid out, as this approach seems to be the most promising for future experiments in the QOEPP project.
In order to study electron-photon coincidence events, section 2 will introduce the fundamentals of electron microscopy and present the most relevant technical aspects of the setup, such as electron detection (Sec. 3.1), energy loss filtering (Sec. 3.2), photon detection (Sec. 3.3) and correlation in time between the electron and the photon.
A brief introduction to cathodoluminescence is given in section 4, followed by a more in depth look at the dominant source of coherent cathodoluminescence in dielectric materials, the Cherenkov effect (see Sec. 4.1). Section 4.2 explains, how the momentum imparted to the electron by the photon results in a measurable deflection.
In section 5 coincidence measurements are discussed, working out expected values for count rates, coincidence rates and noise.
The influence of sample geometry and the option of aloof photon excitation are discussed in section 6. Additionally, detailed simulations for photon excitation in a thin silicon membrane are presented. Limiting factors and potential sources of error for a momentum and energy measurement in the thin silicon membrane are presented in section 7.
Sections 8 to 9.3 discuss four experimental configurations regarding their suitability for conducting different types of coincidence experiments. A particular focus is placed on thin silicon samples (Sec. 8.3), as they have turned out to be the most promising platform for future experiments in Professor Haslinger's QOEPP project.

Die approbierte gedruckte Originalversion dieser Diplomarbeit ist an der TU Wien Bibliothek verfügbar
The approved original version of this thesis is available in print at TU Wien Bibliothek.
TU WIEN Bibliothek Your knowledge hub

2. Electron Microscopy Fundamentals

There are many different platforms for electron microscopy and experiments involving electrons in general, each with their respective strengths and challenges. Exciting research on quantum effects using free electrons can be done and is being done on all of them (see for example [9], [10], [11]). This work deals exclusively with transmission electron microscopy(TEM). There are two main reasons for this: Firstly, the TEM is unmatched in terms of electron detection capabilities. It allows the user to resolve the angle of deflection for each individual electron with sub-microradians precision, as well as to measure its energy to less than an electronvolt [1]. As this work deals with correlations between individual electrons and individual photons, it benefits greatly from being able to make precise measurements on the electron side.
Secondly, the higher acceleration voltage used in a TEM makes it easier to achieve phase matching between the electric field of the electron and the photon. I elaborate further on this point in section 4.1.
A detailed description of how a TEM works can be found in various textbooks such as [12], [13] or [14]. I will only briefly review those aspects that are of particular importance in the context of this work or that play a different role than they do in the regular microscopy context.

2.1. Beam Formation

In analogy to light microscopy, the formation of the electron beam is referred to as the illumination. The top part of the microscope, in which this process takes place is called the condenser. In modern TEMs the condenser typically consists of two to three magnetic lenses and multiple apertures. They can roughly be understood as follows:
The first condenser lens produces a demagnified image of the electron source (e.g. the sharp tip of a tungsten filament). By changing the current running through the C1 lens, the size of this virtual electron source can be tuned.

[1] or even on the order of tens of meV, when using a monochromator

Die approbierte gedruckte Originalversion dieser Diplomarbeit ist an der TU Wien Bibliothek verfügbar
The approved original version of this thesis is available in print at TU Wien Bibliothek.
TU WIEN Bibliothek Your knowledge hub

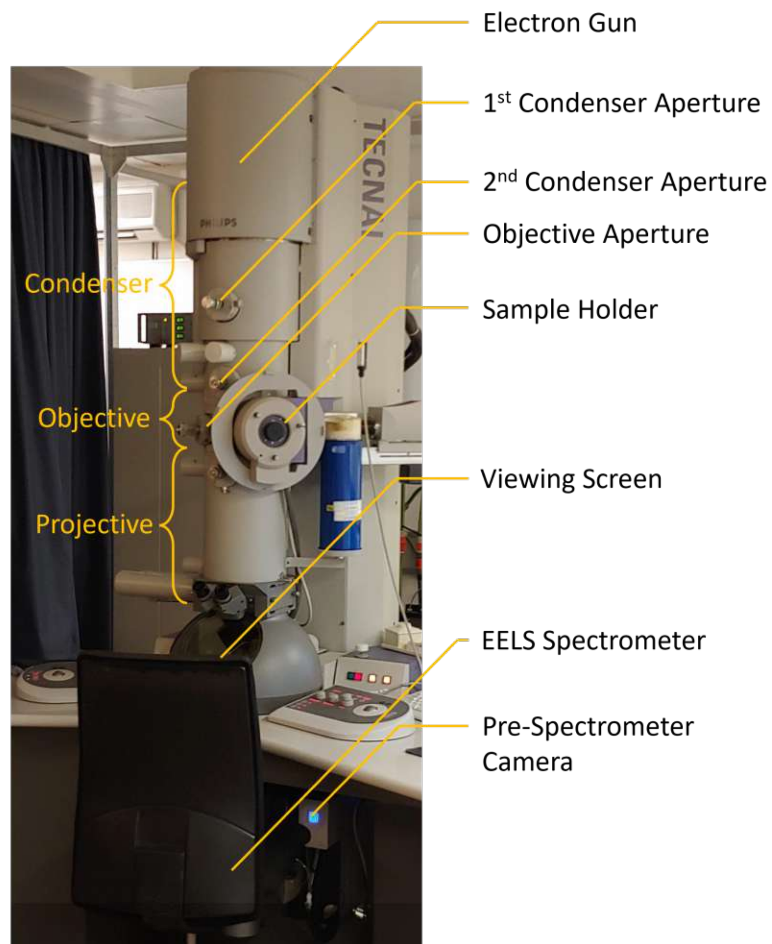

Figure 2.1.: Overview picture of the FEI Tecnai F20 at the University Service Center for Transmission Electron Microscopy at TU Wien (taken by Dominik Hornof).

Die approbierte gedruckte Originalversion dieser Diplomarbeit ist an der TU Wien Bibliothek verfügbar
The approved original version of this thesis is available in print at TU Wien Bibliothek.
TU WIEN Bibliothek Your knowledge hub

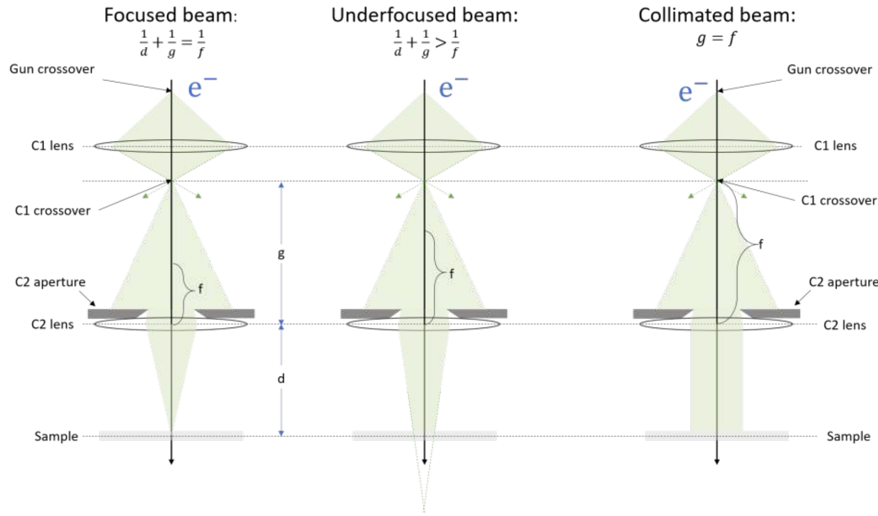

Figure 2.2.: Simplified sketch of a Condenser system in settings producing a focused (left), underfocused (center) or collimated beam (right). By changing the current through the C2 lens, its focal length can be adjusted, thereby producing a different illumination pattern on the sample.

From here the second condenser lens (C2 lens) projects this approximately point-like source onto the specimen. Figure 2.2 shows that varying the current in C2 influences both the size of the illuminated area on the sample as well as the angular distribution of the incoming electrons. In this context a smaller illuminated area will typically correspond to a broader angular distribution.
The electron beam is limited by the C2 aperture. While a smaller aperture can reduce both the illuminated area and the angular distribution, the product of the standard deviations $\sigma_{\mathbf{x}_\perp} \cdot \sigma_{\mathbf{p}_\perp}$ is limited by lens aberrations and, more fundamentally, by Heisenberg's uncertainty principle:

$$\sigma_{\mathbf{x}_\perp} \cdot \sigma_{\mathbf{p}_\perp} \geq \frac{\hbar}{2}$$

with $\hbar$ being Planck's constant (Heisenberg discussed his uncertainty relation in precisely this context in some of his first works on the topic, see [15]).
Depending on the application, it is often desirable to illuminate the sample either with a perfectly collimated beam or with a tightly focused beam.
Note that the setup illustrated in figure 2.2 is only one very simple implementation of a TEM illumination system, modern systems typically use more complex lens configurations to achieve smaller probes or more accurate collimation, for further detail on this refer to [12].

Die approbierte gedruckte Originalversion dieser Diplomarbeit ist an der TU Wien Bibliothek verfügbar
The approved original version of this thesis is available in print at TU Wien Bibliothek.
TU WIEN Bibliothek Your knowledge hub

In the context of a quantum experiment, it is useful to see the illumination process as the preparation of the electron's initial state. This state can be described both in position and momentum space in terms of wave packets, the following treatment (taken from [16, Chapter 2]) is non-relativistic and does not account for electron spin.
For a fully coherent collimated beam the electron wave function can be described as a plane wave with wave vector $\vec{k}$ and energy E traveling along the beam axis, that is limited by a circular aperture of radius R_{C2}. At the plane of the sample, it can be written as:

$$\psi_{\mathrm{collimated}}(\vec{r},t) = A(x,y)e^{i\vec{k}\cdot\vec{r}}e^{-i\frac{E}{\hbar}t}$$

with:

$$\vec{k} = \begin{pmatrix} 0 \\ 0 \\ k_{\parallel} \end{pmatrix}$$

and:

$$A(x,y) = \begin{cases} \sqrt{\frac{1}{\pi R_{\mathrm{C2}}^2}} & x^2+y^2 < R_{\mathrm{C2}}^2 \\ 0 & x^2+y^2 > R_{\mathrm{C2}}^2 \end{cases}$$

In the case of the focused beam, the wave function can be described as an airy disk in real space. This can be modeled by assuming a plane wave at the C2 lens which is restricted by the C2 aperture, similar to what has been presented above in the collimated case. The wave function $\psi_{\mathrm{aperture}}(x',y')$ is given at the C2 aperture and is focused onto the sample which is located on the focal plane of the C2 lens. This focusing corresponds to a Fourier transform of ψ_{aperture}, consequently the wave function at C2 can be taken to represent the wave function of the focused beam in k-Space :

$$\psi_{\mathrm{focus}}(\vec{k},t) = A(k_x,k_y)\cdot e^{-i\frac{E}{\hbar}t}$$

with:

$$A(k_x,k_y) = \begin{cases} \sqrt{\frac{1}{\pi k_{\mathrm{max}}^2}} & k_x^2+k_y^2 < k_{\mathrm{max}}^2 \\ 0 & k_x^2+k_y^2 > k_{\mathrm{max}}^2 \end{cases}$$

Rewriting this in cylindrical coordinates and following the derivation given in [16, Chapter 2], this yields:

$$\psi_{\mathrm{focus}}(\vec{r}) = 2[\frac{J_1(rk_{\mathrm{max}})}{rk_{\mathrm{max}}}]e^{ik_z z}e^{-i\frac{E}{\hbar}t}$$

Die approbierte gedruckte Originalversion dieser Diplomarbeit ist an der TU Wien Bibliothek verfügbar
The approved original version of this thesis is available in print at TU Wien Bibliothek.
TU Bibliothek WIEN Your knowledge hub

where $J_1(x)$ is a Bessel function of the first kind and $k_{\max}$ can be determined from the radius of the C2 aperture as:

$$k_x = \frac{x}{\lambda_e f}, k_y = \frac{y}{\lambda_e f} \implies k_{\max} = \frac{R_{C2}}{\lambda_e f}$$

where f is the focal length of the C2 lens and λ_e is the de Broglie wavelength of the electron.
Another concern for many potential experiments is the coherence of the initial electron wave function. High transverse and temporal coherence of the initial electron state is beneficial for high resolution imaging. In high resolution transmission electron microscopy (HRTEM) what is observed is almost exclusively phase contrast, consequently the contrast formation mechanism at play is precisely the interference between deflected and undeflected portions of the electron wave function [13, Chapter 4].
Generally speaking, the temporal coherence length of the electron beam can be improved by reducing the variance of the electron energy distribution [16, Chapter 2.8], this can be achieved by using colder field emission sources or using a monochromator on the initial beam. Measurements on the energy distribution of the field emission source of the Tecnai F20 that was used in this work can be found in section 8.3.
The transverse coherence width can be improved by reducing the effective transverse size of the electron source (towards a point source)[16, Chapter 2.9]. This does not necessarily mean reducing the physical size of the source, using electron optics and apertures to only accept electrons originating from a smaller volume within the source can also improve the transverse coherence width.
While central in the context of potential future experiments in the QOEPP project, coherence aspects concerning the electron are not particularly relevant for understanding the topics that are within the scope of this work. For precise definitions and detailed explanations of temporal and transverse coherence please refer to the cited works [13] and [16].

2.2. Electron-Sample Interaction

We typically prepare a given number of electrons per second in the initial state. The current can be chosen from more than a billion electrons per second (> 1.5 nA) down to just a couple of thousands (≈ 1 fA). By inserting no sample in the beam path, we can measure position-, momentum- and energy distribution of the electrons in that initial state.
When the electron interacts with the sample, it is scattered. In texts on electron microscopy it is typical to distinguish between elastic and inelastic scattering.

Die approbierte gedruckte Originalversion dieser Diplomarbeit ist an der TU Wien Bibliothek verfügbar
The approved original version of this thesis is available in print at TU Wien Bibliothek.
TU WIEN Bibliothek Your knowledge hub

Elastic scattering refers to processes in which the electron is deflected without loosing a measurable amount of its kinetic energy [16, Chapter 1.1]:

$$e^-(E_0, \vec{k}_0) \rightarrow e^-(E, \vec{k})$$

with $E_0 \approx E$. Inelastic scattering includes all processes in which the electron does change its kinetic energy:

$$e^-(E_0, \vec{k}_0) \rightarrow e^-(E, \vec{k}) + \hbar\omega$$

or:

$$e^-(E_0, \vec{k}_0) \rightarrow e^-(E, \vec{k}) + A^*$$

with $E_0 \neq E$ where A^* indicates an excited quantum state in the sample and $\hbar\omega$ represents the emission of a photon. Many different phenomena, such as the emission of Bremsstrahlung, the ejection of secondary electrons, the excitation of plasmons, phonons [2] and excitons, as well as many more fall into this category (see: [12, Chapter 4]).
As it is our goal to study electron-photon pairs, we are interested in those processes, that involve the emission of an optical photon, they will be discussed in detail in section 4. Section 3 will explain, how the emitted photons are detected experimentally.

2.2.1. Inelastic Scattering

Generally speaking, whenever the electron interacts with the sample, it undergoes one of many different processes i [3], each time transferring a discrete package of energy ($\Delta E = E_0 - E$) and momentum ($\Delta \mathbf{p} = \mathbf{p}_0 - \mathbf{p}$) and each occurring with a certain probability $P_i(\Delta E, \Delta \mathbf{p} | E_0, \mathbf{p}_0)$. This probability typically (with the exception of surface effects like transition radiation) increases with the interaction length L, which is given by the thickness of the sample i.e. $P_i = P_i(L)$ [18, Chapter 3.4]. Classically, electron scattering is treated as deflection of the electron trajectory, it can be described using the scattering cross section [18, Chapter 3.1]:

$$I_{\Omega_\mathrm{D},\varepsilon} = I_0 N \sigma_{\Omega_\mathrm{D},\varepsilon}$$

where $\sigma_{\Omega_\mathrm{D},\varepsilon}$ is the absolute scattering cross section, I_0 represents the number of electrons per second in the initial beam, I describes how many of these electrons are scattered into a given solid angle Ω_D and energy range ε that we imagine to

[2] In the past, the energy loss due to the excitation of a phonon was to small to be measured, this has changed with recent improvements in electron energy resolution, see: [17]

[3] Of course the same electron can interact with the sample multiple times via independent processes.

Die approbierte gedruckte Originalversion dieser Diplomarbeit ist an der TU Wien Bibliothek verfügbar
The approved original version of this thesis is available in print at TU Wien Bibliothek.
TU WIEN Bibliothek Your knowledge hub

be covered by a detector. Typically, σ is defined for a single scatterer and needs to be multiplied by the density of scatterers per unit area N.

The differential cross section $\frac{d^2\sigma}{d\Omega dE}$ is related to the total cross section $\sigma_{\Omega_{\mathrm{D}},\varepsilon}$ by:

$$\sigma_{\Omega_{\mathrm{D}},\varepsilon} = \int_{\Omega_{\mathrm{D}}} d\Omega \int_{\varepsilon} \frac{d^2\sigma(\phi,\theta,E)}{d\Omega dE} dE \tag{2.1}$$

Analogously to [18, Chapter 3.1], $\frac{d^2\sigma(\phi,\theta,E)}{d\Omega dE}$ is a scattering probability in unit area per scatterer (i.e. per atom), per unit of solid angle Ω, per unit of energy E. It is parameterized in spherical coordinates with θ being the polar angle with respect to the beam axis, leading to the usual relation $d\Omega = \sin(\theta) d\theta d\phi$.[4]
Consequently:

$$I_{\Omega_{\mathrm{D}},\varepsilon} = \int_{\Omega_{\mathrm{D}}} d\Omega \int_{\varepsilon} I(\phi,\theta,E) dE \tag{2.2}$$

with $I(\phi,\theta,E)$ referring to a number of electrons per second per unit of solid angle Ω per unit of energy E.
σ can summarize multiple processes and can be understood as the sum of multiple contributions σ_i, each characteristic for a distinct scattering process between the electron and the sample. It typically doesn't include the possibility of multiple and plural scattering, which in general need to be considered in order to explain the final intensity distribution measured.
The probability of one electron interacting with the sample more than once via the same interaction mechanism (e.g. plasmon excitation) is approximately $P_i(L)^2$. For a very thin sample, the influence of multiple scattering becomes negligible:

$$\lim_{L\to 0} P_i(L) = 0 \implies P_i(L)^2 \ll P_i(L) \tag{2.3}$$

for small enough values of L.
Under this condition the measured intensity on the detector is approximately (analogously to [18, Chapter 3.4]):

$$I(\phi,\theta,E) \approx \mathrm{SSD}(\phi,\theta,E) = I_0 (n_{\mathrm{a}} L \frac{d^2\sigma}{dE d\Omega} + \frac{d^2 P_{\mathrm{surface}}}{dE d\Omega}) \tag{2.4}$$

The cross section under the assumption that no multiple scattering occurs is referred to as the single scattering distribution SSD, the probability P_{Surface} summarizes scattering from surface interactions.

[4] In elastic processes for example, this differential cross section is only non-zero at $E \approx E_0$.

Die approbierte gedruckte Originalversion dieser Diplomarbeit ist an der TU Wien Bibliothek verfügbar
The approved original version of this thesis is available in print at TU Wien Bibliothek.
TU WIEN Bibliothek Your knowledge hub

How thin the sample has to be, in order to assume that multiple scattering is negligible, is determined by ℓ_i, the electron's mean free path with respect to the process i :

$$\frac{L}{\ell_i} \ll 1$$

In a setup in which the electron interacts with the sample in multiple ways, each with their respective mean free path ℓ_i, this means that at a certain thickness multiple scattering may be negligible for a process i while still being very likely for another process j, because $\ell_j < \ell_i$.
Typically, the scattering probability is simply modeled using the Lambert-Beer law [18, Chapter 2.6]:

$$P_i(L) = 1 - e^{-\frac{L}{\ell_i}} \tag{2.5}$$

And in this case the argument in Eq. 2.3 can be extended to:

$$\lim_{L\to 0} \frac{P_i(L)^2}{P_j(L)} = 0 \implies P_i(L)^2 \ll P_j(L)$$

for any pair of values ℓ_i, ℓ_j, for small enough values of L. In practice however, the minimal thickness of our sample is limited and the cross section for processes producing cathodoluminescence is significantly smaller than for other effects. For coherent emission from 100 nm of silicon, a probability of less than 1% per electron is expected (see section 4.1). The corresponding mean free path is given by:

$$\ell_{\mathrm{CL}} = \frac{-L}{\ln\left(1 - P_{\mathrm{CL}}\right)} \approx 10\ \mu\mathrm{m}$$

In comparison, a paper by Iakoubovskii et al. ([19]) gives the inelastic mean free paths for various materials. All given values are below 170 nm. These values refer to 200 keV electrons in amorphous materials and exclude energy losses above 150 eV and deflection angles over 20 mrad. Using a lower acceleration voltage or including a larger range of energy loss and deflection, one would expect even shorter mean free paths. Taking the values for pure amorphous silicon specifically, the combined mean free path for all inelastic processes is $\ell_{\mathrm{in}} = 145$ nm; the mean free path for the emission of plasmons alone is $\ell_{\mathrm{plasmon}} = 168$ nm. According to [20] the difference in inelastic mean free path between amorphous and crystalline silicon is small. Consequently, multiple inelastic scattering from plasmons is expected to be many times more likely than emission from the processes described by ℓ_{CL} on the typical thickness scales of a TEM sample.
Another paper by Iakoubovskii et al. [21] provides values for the elastic mean free path under the same conditions as [19], unfortunately this work does not include

Die approbierte gedruckte Originalversion dieser Diplomarbeit ist an der TU Wien Bibliothek verfügbar
The approved original version of this thesis is available in print at TU Wien Bibliothek.
TU WIEN Bibliothek Your knowledge hub

ℓ_{el}	130 nm	Elastic scattering (calculated according to Eq. 2.6, using $\ell_{\text{el}} = \frac{1}{\sigma_{\text{el}} n_{\text{Si}}}$)
ℓ_{in}	145 nm	All inelastic scattering (from [19]
ℓ_{Plasmon}	168 nm	Plasmon excitation (from [19]
ℓ_{other}	1 µm	Inelastic scattering excluding plasmons excitation (calculated from ℓ_{in}, ℓ_{Plasmon} assuming Eq. 2.5)
ℓ_{CL}	10 µm	Coherent CL (see section 4.1)

Table 2.1.: Mean free paths for 200 keV electrons in silicon with respect to various processes.

silicon. According to [18, Chapter 3.1] the elastic cross section can be calculated with accuracy better than 30% using an empirical formula proposed in [22]:

$$\sigma_{\text{el}} = \frac{(1.5 \cdot 10^{-24}\ \text{m}^2) Z^{(3/2)}}{\beta^2} [1 - \frac{Z}{596\beta}] \tag{2.6}$$

with $\beta = v_{\text{e}}/c$ being the velocity of the electron as a fraction of the speed of light and Z being the atomic number of the element considered. Using $\ell_{\text{el}} = \frac{1}{\sigma_{\text{el}} n_{\text{A}}}$, with the atomic density $n_{\text{A}} = 4.995 \cdot 10^{28}$ atoms/m^3 for silicon, this gives an elastic mean free path of 130 nm.
Table 2.1 summarizes the relevant values for amorphous silicon[5]. Therefore elastic scattering is also expected to be much more likely than the emission of cathodoluminescence.

2.2.2. Elastic Scattering and Imaging

Within a material, the potential varies depending on the distance to neighboring atoms; closer to the atomic nuclei, the fields are usually stronger. Therefore, the phase an electron picks up, will depend on where it traverses the sample. This mechanism gives rise to phase contrast, first described by Frits Zernike in the context of light microscopy (Nobel Prize 1953, see [23],[24]) which allows for the resolution of subatomic scales in electron microscopy. Assuming the TEM sample to be thin enough, it can be described as a phase object, (see [13, Chapter 3.4]) the electron's wave function can then be written as:

$$\psi_{\text{out}} = \psi_{\text{in}} \cdot e^{-iCV_{\text{p}}(x,y)} \tag{2.7}$$

[5]For elastic scattering, the difference in mean free path between crystalline and amorphous samples may be more significant, keeping this limitation in mind, these values will still be used as given to arrive at the estimates presented in section 7.

Die approbierte gedruckte Originalversion dieser Diplomarbeit ist an der TU Wien Bibliothek verfügbar
The approved original version of this thesis is available in print at TU Wien Bibliothek.
TU Bibliothek WIEN Your knowledge hub

with $C = \frac{2\pi\gamma m_e e \lambda_e}{h^2}$ [6] and $V_p = \int_L V(x,y,z)dz$ as the projected specimen potential. By using the weak phase object approximation, this yields:

$$\psi_{out} \approx \psi_{in} \cdot (1 - iCV_p(x,y))$$

So far we have included the initial wave function ψ_{in}, which is left out in [13, Chapter 3.4] but is present in other treatments of weak phase object approximation such as [16]. From now on a plane wave of amplitude 1 will be assumed for ψ_{in}.
The distribution on the back focal plane of the objective is given by the Fourier transform of ψ_{out} in x and y:

$$\psi_{out}(u,v) = \mathcal{F}_{x,y}[\psi_{out}(x,y)] \tag{2.8}$$
$$= \mathcal{F}_{x,y}[1 - iCV_p(x,y)] \tag{2.9}$$
$$= \delta(\vec{k}_\perp) - iC\mathcal{F}_{x,y}[V_p(x,y)] \tag{2.10}$$

with $u, v \propto k_x, k_y$. By forming the absolute square of the wave function, which corresponds to a probability density in k-space, we obtain:

$$|\psi_{out}|^2 = (1 - P_{el}) \cdot \delta(\vec{k}_\perp) + P_{el} \cdot |\mathcal{F}_{x,y}[V_p(x,y)]|^2 \tag{2.11}$$

i.e. the elastic scattering under these assumptions is determined by a scattering probability P_{el}, which is obtained by normalizing 2.10, and a scattering distribution given by the Fourier transform of the sample potential projected along the beam axis V_p.

The scattering amplitude, under the same assumptions as in [16, Chapter 4.3], is given by the expression:

$$f(\vec{k} - \vec{k}_0) \propto \mathcal{F}[V(\vec{r})](\vec{k} - \vec{k}_0) \tag{2.12}$$

which implies:

$$\frac{d\sigma}{d\Omega} \propto |f(\vec{k} - \vec{k}_0)|^2 \propto |\mathcal{F}[V(\vec{r})](\vec{k} - \vec{k}_0)|^2 \tag{2.13}$$

Here the solid angle is parameterized using $\vec{k}' = \vec{k} - \vec{k}_0$, therefore for small angles θ, one can use:

$$d\Omega \approx \frac{dk'_x dk'_y}{|\vec{k}_0|^2}$$

[6] In the book, a relativistic correction for the wavelength is applied, the difference is small in regular TEMs.

Die approbierte gedruckte Originalversion dieser Diplomarbeit ist an der TU Wien Bibliothek verfügbar
The approved original version of this thesis is available in print at TU Wien Bibliothek.
TU WIEN Bibliothek Your knowledge hub

The relation in Eq. 2.13 is already indirectly suggested in Eq. 2.11, in the two dimensional case k_x and k_y approximate the respective components of $\vec{k} - \vec{k}_0$.

A simple but very effective way of building a model of the specimen potential, is to assume an effective potential $V_{\text{atom}}(\vec{r})$ of each atom and model the total potential of a sample as a sum of many of these individual potentials located at each atom site $\vec{R}_i$ [25, Chapter 5.3]:

$$V(\vec{r}) = \sum_i \delta^3(\vec{R}_i - \vec{r}) * V_{\text{atom}}(\vec{r})$$

Where $\delta^3(\vec{R}_i - \vec{r}) * V$ is the convolution of those two functions. More sophisticated techniques for calculating the potential include various ab-initio methods, e.g. applying density functional theory [26]. The simple model is already very useful in many practical cases and very instructive, as it naturally introduces the role of the crystal lattice for elastic diffraction.
For atoms arranged in a periodical lattice $\vec{R}_i = n_1\vec{a}_1 + n_2\vec{a}_2 + n_3\vec{a}_3$ with the primitive lattice vectors $\vec{a}_i$:

$$\mathcal{F}[\sum_i \delta^3(\vec{R}_i - \vec{r})] = \sum_i \delta^3(\vec{G}_i - (\vec{k} - \vec{k}_0))$$

The position of the diffraction spots is given by the reciprocal lattice vectors $\vec{G}_i$, which are defined in accordance with [27], see Appendix A.

With the convolution theorem:

$$\mathcal{F}(f \cdot g) = \mathcal{F}(f) * \mathcal{F}(g)$$

and the identity 2.13 for the elastic scattering cross section:

$$\frac{d\sigma}{d\Omega} \propto |\mathcal{F}[\sum_i \delta^3(\vec{R}_i - \vec{r}) * V_{\text{atom}}(\vec{r})]|^2 \tag{2.14}$$

$$= |\sum_i \delta^3(\vec{G}_i - (\vec{k} - \vec{k}_0)) \cdot \mathcal{F}(V_{\text{atom}}(\vec{r}))|^2 \tag{2.15}$$

As the lattice constants of typical crystalline materials are typically in the range of a few Angstrom, the momentum transfer is typically on the order of 1/nm, which corresponds to an electron deflection in the mrad range for 200 keV electrons. As $V_{\text{atom}}(\vec{r})$ varies over an even smaller distance in real space, it corresponds to modulation of the wave function over a wide range in k-space. On the comparatively large scale of tens to hundreds of nanometers, there may be variations in the thickness and morphology of the sample. These inhomogeneities are reflected

Die approbierte gedruckte Originalversion dieser Diplomarbeit ist an der TU Wien Bibliothek verfügbar
The approved original version of this thesis is available in print at TU Wien Bibliothek.
TU WIEN Bibliothek Your knowledge hub

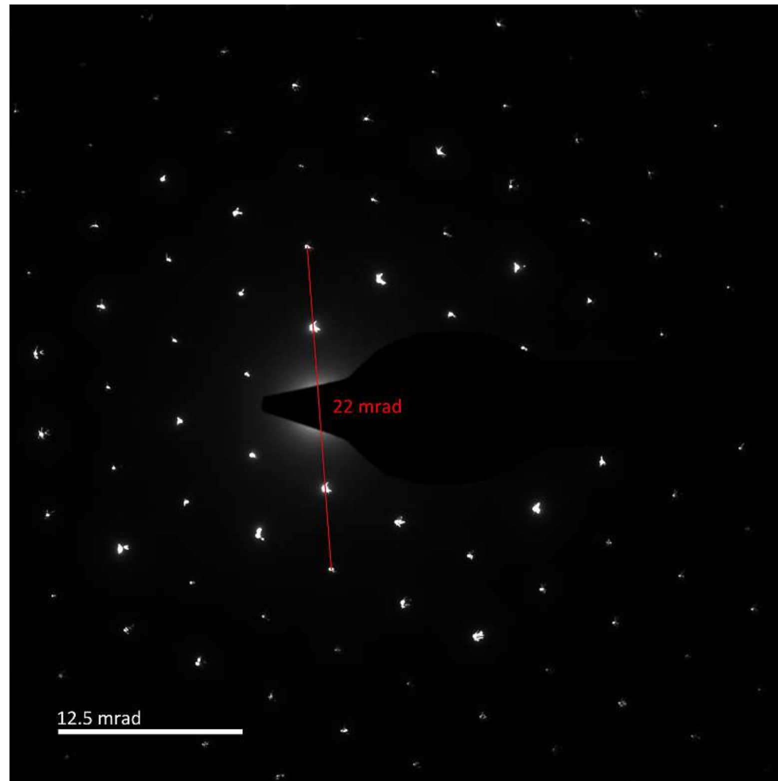

Figure 2.3.: TEM diffraction image of a crystalline sample (mica). The angles between the diffraction maxima are inversely proportional to the spacing of the crystal lattice.

in variations on a very small scale in k-space. The same is true for the emission of photons, which also leads to a small deflection in k-space, as will be shown in section 4.2.

Die approbierte gedruckte Originalversion dieser Diplomarbeit ist an der TU Wien Bibliothek verfügbar
The approved original version of this thesis is available in print at TU Wien Bibliothek.
TU WIEN Bibliothek Your knowledge hub

3. Measurement Setup

This section will describe the measurement setup that is going to be used for coincidence experiments in the Quantum Optics with Electron-Photon Pairs (QOEPP) project. Figure 3.1 gives a general overview of the setup: The electron is emitted from the electron gun and illuminates the sample which is mounted in a sample holder that allows for photon detection. As the electrons transition through the sample, they coherently emit photons which are collected in two ellipsoidal mirrors and guided out of the microscope column via two separate multimode fibers. Each of the fibers is connected to a single photon detection module (SPDM). A more detailed explanation of the photon detection is given in section 3.3. Whenever a photon is detected the single photon detection module produces a voltage signal which is time stamped by a dedicated time tagging device.
After transitioning through the sample, the magnetic lenses of the microscope project the electron onto the entrance aperture of the electron energy loss spectrometer. Depending on the lens settings, the electrons are either imaged in the near- or far field, measuring either position on the sample plane or transverse momentum (see section 3.1). The electron spectrometer images the incoming electron onto a Timepix3 direct detection camera which is able to detect and time the impact of individual electrons according to its internal clock.
Depending on the spectrometer settings it is either possible to resolve the energy of of the incoming electron or to obtain an energy filtered version of the image projected onto the spectrometer entrance aperture (see Sec. 3.2).
As the internal clocks of the time tagger and the Timepix3 camera are synchronized to a common external clock, it is possible to correlate the arrival times of the individual electrons and photons in post processing, this allows for the identification of coincident electron-photon pairs.

3.1. Electron Detection

In order to analyze the final state that is created by the interaction between electron and sample, it is necessary to resolve the distribution of detected electrons in both position and momentum.
Using the microscope in imaging mode, the focal lengths of its magnetic lenses are set to image the sample plane onto the plane of the detector below, approximately

Die approbierte gedruckte Originalversion dieser Diplomarbeit ist an der TU Wien Bibliothek verfügbar
The approved original version of this thesis is available in print at TU Wien Bibliothek.
TU WIEN Bibliothek Your knowledge hub

Die approbierte gedruckte Originalversion dieser Diplomarbeit ist an der TU Wien Bibliothek verfügbar
The approved original version of this thesis is available in print at TU Wien Bibliothek.
TU WIEN Bibliothek Your knowledge hub

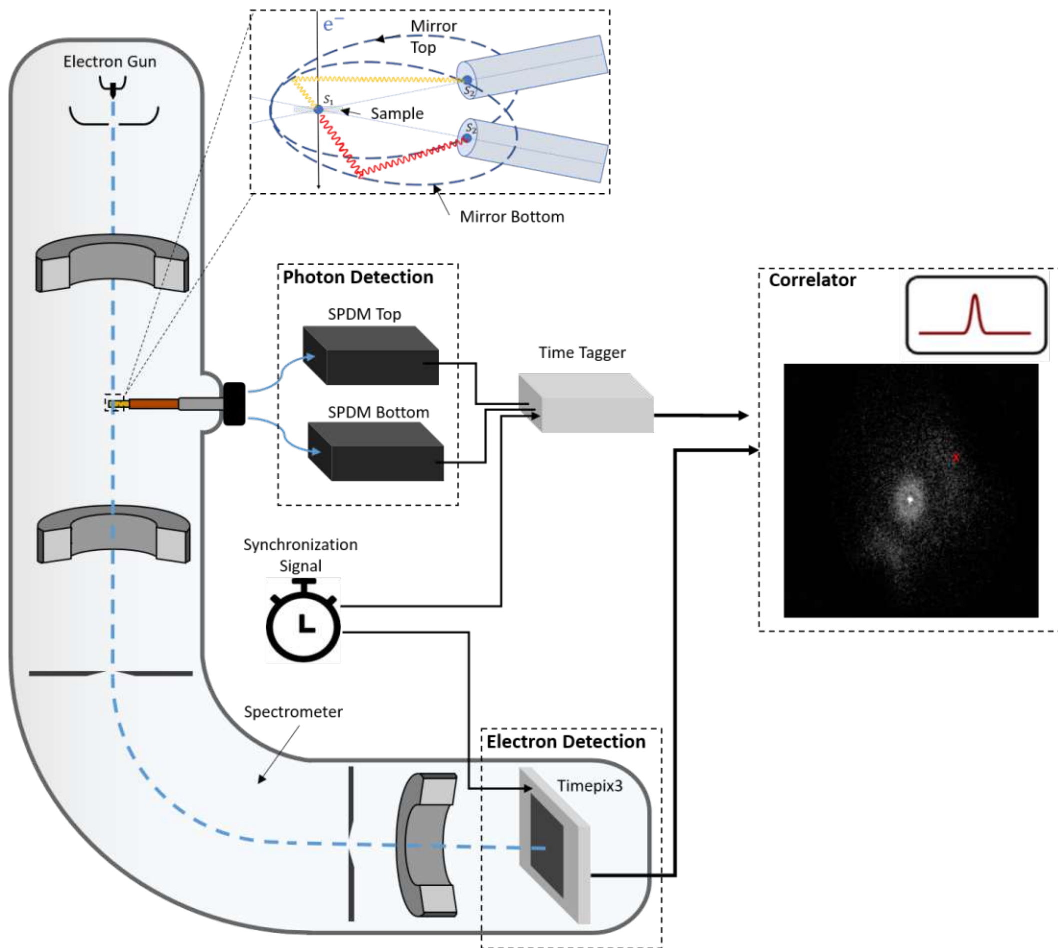

Figure 3.1.: Overview of the experimental setup to investigate electron-photon correlations. Electrons are emitted from the electron gun and accelerated onto the sample where they produce photons. The transmitted electrons are energy filtered in an electron energy loss spectrometer and projected onto a Timepix3 where they are detected and time stamped. The photons are collected using a pair of elliptical mirrors coupling into multimode optical fibers. Photons are detected using a single photon counting module (SPDM) and time stamped using a dedicated time tagger. By matching the respective time stamps, electrons that arrived in coincidence with a photon can be identified (symbolized by the red cross in the electron diffraction image).

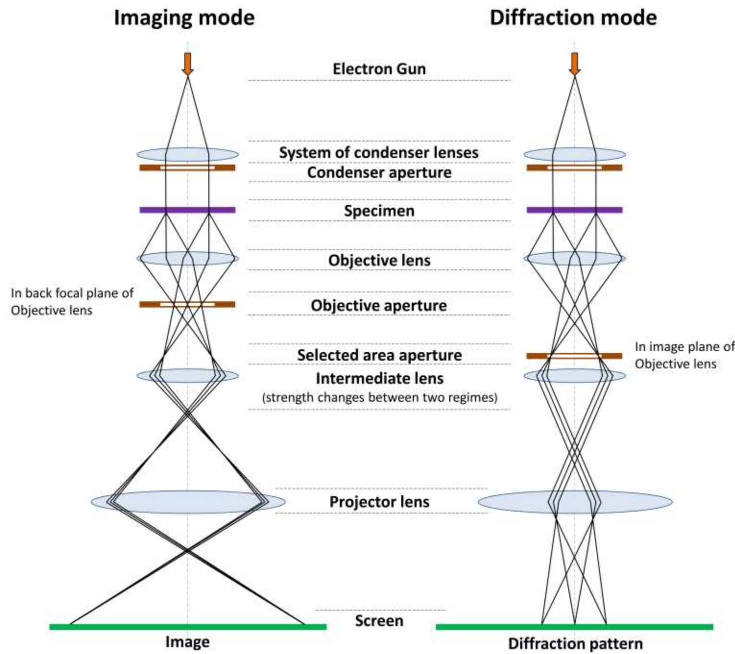

Figure 3.2.: Ray diagram of a transmission electron microscope in imaging mode (left) and diffraction mode (right). By changing the current through the intermediate lens, its focal length can be adjusted to either image the image plane of the objective lens (left, for imaging) or it can be set to image the back focal plane of the objective lens (right, for diffraction). (Image by Eric Kvaalen, taken from Wikimedia Commons [28])

reproducing time evolved exiting wave function ψ_{out}. The camera then detects the absolute square of this wave function.

The resolution achievable on the electron position is very good. The experiments considered in this project over the last year involve comparatively large structures, e.g. masks with features on the scale of micrometers, multi-slit masks with a periodicity of a few hundred nanometers or aloof setups, where the electron needs to pass within a range of a few tens of nanometers. Therefore the schemes that were considered are typically not limited by the microscope's spatial resolution.

Measurements in momentum space on the other hand need to be able to resolve the momentum transferred by individual photons, which result in deflection angles on the scale of microradians, as discussed in section 4.2.

The electron microscope used mostly in this project is a FEI Tecnai F20 with a Schottky source. It is equipped with a variety of detectors. The ones that were used for the preliminary experiments presented in this thesis are the Gatan Rio 16,

Die approbierte gedruckte Originalversion dieser Diplomarbeit ist an der TU Wien Bibliothek verfügbar
The approved original version of this thesis is available in print at TU Wien Bibliothek.
TU WIEN Bibliothek Your knowledge hub

a fiber-optically coupled CMOS camera which is located below the viewing screen of the TEM and the UltraScan 1000, a fiber coupled CCD device, located behind the Gatan Tridiem Electron energy spectrometer. The USTEM is currently in the process of upgrading the Tecnai F20 with the Timepix3 camera, located behind the electron spectrometer. The Timepix3 is a direct electron detection camera that can be read out on a event-by-event basis, i.e. each incident electron can be registered individually with a time resolution of a few nanoseconds. This is the camera that is actually going to be used to measure correlated electron photon pairs in the future.
In low angle diffraction mode, the Tecnai F20 can achieve camera lengths R of up to a kilometer pre-spectrometer the spectrometer itself provides another factor of 18 in magnification, when used in energy-filtered TEM (EFTEM) mode. Assuming a Nyquist sampling distance of $2.3 \cdot (\text{pixelsize})$ [29] and accepting the nominal camera length of 1 km, which is easily achievable, angular resolution of the electrons is not limited by these factors down to:

$$\Delta\alpha > \arctan\left(\frac{2.3 \cdot (\text{pixelsize})}{1000\ \text{m}}\right) \tag{3.1}$$

The resulting limits on resolution for each of the three cameras are given in table 3.1. Taking the additional magnification of the spectrometer into account, the limitation imposed by the camera resolution is certainly well below the diffraction limit imposed by the $R = 30\ \mu\text{m}$ wide C2 aperture:

$$\Delta\alpha_{\text{Rayleigh}} = \arcsin\left(1.22 \cdot \frac{\lambda}{d}\right) \approx 1.22 \cdot \frac{2.5\ \text{pm}}{30\ \mu\text{m}} \approx 100\ \text{nrad}$$

which corresponds to:

$$\Delta\alpha_{\text{FWHM}} = \arcsin\left(1.04 \cdot \frac{\lambda}{d}\right) \approx 87\ \text{nrad}$$

if one considers the full width half maximum of the airy disc instead of the position of the first minimum.

Name	Rio 16	UltraScan 1000	Timepix3
Type	CMOS	CCD	Hybrid pixel detector
Pixels	4096 x4096	2048 x 2048	256 x 256
Pixel size	9 µm	14 µm	55 µm
Minimal time resolution	-	-	1.6 ns (event driven)
Resolution limit @ R = 1 km	21 nrad	32 nrad	125 nrad

Table 3.1.: Overview of available cameras at USTEM. Resolution limits were calculated according to Eq. 3.1

Die approbierte gedruckte Originalversion dieser Diplomarbeit ist an der TU Wien Bibliothek verfügbar
The approved original version of this thesis is available in print at TU Wien Bibliothek.
TU WIEN Bibliothek Your knowledge hub

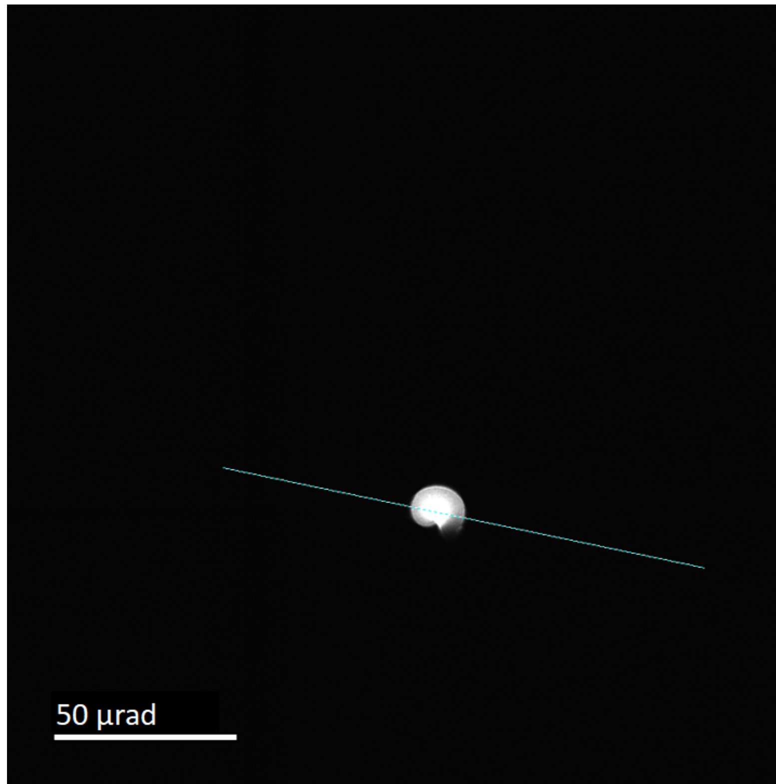

Figure 3.3.: TEM diffraction image measuring the momentum distribution of the initial electron beam without sample interaction.

Simply measuring the beam without a sample, it is normal to attain an angular distribution of $\Delta\alpha_{\mathrm{FWHM}} < 0.3$ µrad on our device (see Fig. 3.3), the additional broadening is due to various optical aberrations.

When working with the cameras at USTEM we try to keep the current on the detector below 3000 electrons per pixel per second on the Rio 16 and below 1000 electrons per pixel and second on the UltraScan 1000 in order to avoid damage to the respective device. The total current on the sensor that one can work with in diffraction mode, when imaging the undeflected beam depends on the camera length used, typical values are in the range of < 10 pA. The limiting factor when using the Timepix3 will probably be the limited readout rate of 40 million events per second. Each electron that hits the sensor typically deposits its energy into more than one pixel, triggering multiple detection events. Assuming that four events on average are triggered per electron impact, 40 million events per second correspond to roughly 10 million electron hits per second. This is equivalent to a current of approximately 1.5 pA.

Die approbierte gedruckte Originalversion dieser Diplomarbeit ist an der TU Wien Bibliothek verfügbar
The approved original version of this thesis is available in print at TU Wien Bibliothek.
TU WIEN Bibliothek Your knowledge hub

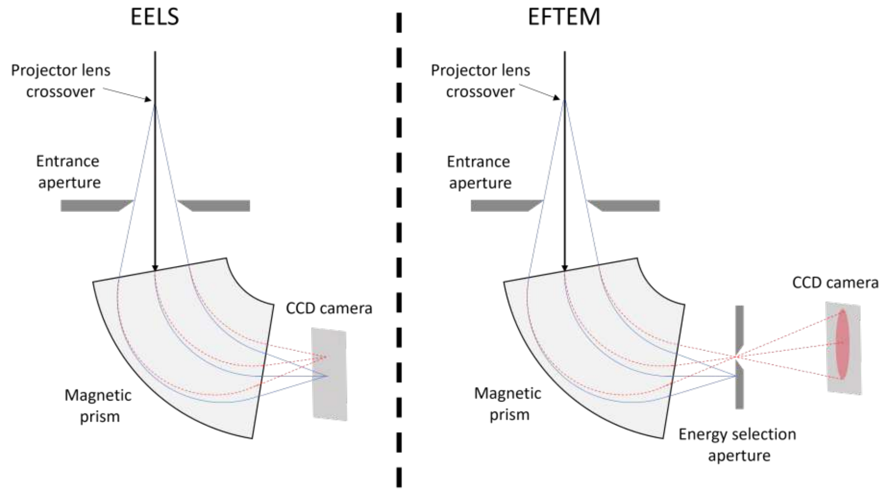

Figure 3.4.: Working principle of the Gatan image filter, set up for energy loss spectroscopy (left) and energy filtering (right). The electron beam enters the spectrometer through the entrance aperture, in the magnetic prism a homogeneous magnetic field pointing into the paper plane deflects the incoming electrons. The electron trajectory in the field is circular with its radius depending on the energy of the electron. In spectroscopy mode the electron energy loss distribution is imaged directly onto a CCD camera, in EFTEM mode a region in the energy loss spectrum is selected using an aperture and an image is produced on the CCD camera in a plane behind the aperture.

3.2. Electron Energy Loss

The energy of the measured electron can be analyzed by using an energy filter. As mentioned previously, the filter that was used for the measurements presented in this work is the Tridiem system by Gatan. The working principle of the Gatan image filter is illustrated in figure 3.4: When set to spectroscopy mode, a magnetic prism produces a constant magnetic field perpendicular to the electron beam (in Fig. 3.4 the field points out of the paper plane), the electrons proceed on a bent trajectory due to the Lorentz force, the bend radius depends on the kinetic energy of the electron. The spectrometer's entry slit is imaged onto the spectrometer camera and offset by an energy dependent amount. In energy-filtered TEM (EFTEM) mode, the energy is filtered using an aperture and then transformed back into an image, which results in a filtered version of the image that was input to the spectrometer by the projector.

When measuring electron energy, the knowledge that can be gained on $\frac{d\sigma_i}{d\Omega dE}$ is

Die approbierte gedruckte Originalversion dieser Diplomarbeit ist an der TU Wien Bibliothek verfügbar
The approved original version of this thesis is available in print at TU Wien Bibliothek.
TU WIEN Bibliothek Your knowledge hub

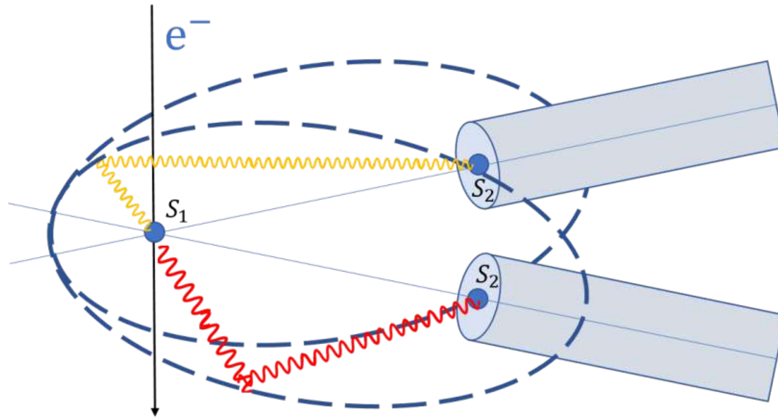

Figure 3.5.: Schematic illustration of the Vulcan system by Gatan: two ellipsoidal mirrors with overlapping focal points S_1 at the sample collect light and focus it onto the facets of two multi-mode fibers at focal points S_2.

limited by the initial energy distribution $\rho(E_0)$ of the electrons. The resulting energy distribution is a convolution $\rho(E_0) * \frac{d\sigma_i}{d\Omega dE}$. The width of $\rho(E)$ depends on the electron source used, the Schottky source of the Tecnai F20 is set to an extractor voltage of 4000 V by default, leading to full width half maximum of $\Delta E_{\text{FWHM}} \approx 1.0$ eV. Using a reduced extractor voltage of 3000 V, it can be lowered to:

$$\Delta E_{\text{FWHM}} = 0.7 \text{ eV}$$

3.3. Photon Collection

In order to be able to correlate electrons and photons, a setup is needed that allows for both particles to be detected simultaneously. The system used for the detection of photons throughout most of this work is the Vulcan system by Gatan (see figure 3.5). It consists of two ellipsoidal mirrors: one mounted above, one below the sample. The electron enters the holder through a hole in the upper mirror, penetrates the sample and is transmitted out of the holder through an aligned hole in the bottom mirror (both 500 µm in diameter). One of each mirror's two focal points overlap at the sample (S_1 in figure 3.5), collecting photons from a total solid angle of 7.2 steradian. The mirrors focus the light emitted from the sample to the respective focal points S_2. A multi-mode optical fibers with a core diameter of 400 µm and numerical aperture of 0.39 is placed at each of the focal points S_2, guiding the collected photons out of the microscope column and to the detector.

Die approbierte gedruckte Originalversion dieser Diplomarbeit ist an der TU Wien Bibliothek verfügbar
The approved original version of this thesis is available in print at TU Wien Bibliothek.
TU WIEN Bibliothek Your knowledge hub

Die approbierte gedruckte Originalversion dieser Diplomarbeit ist an der TU Wien Bibliothek verfügbar
The approved original version of this thesis is available in print at TU Wien Bibliothek.

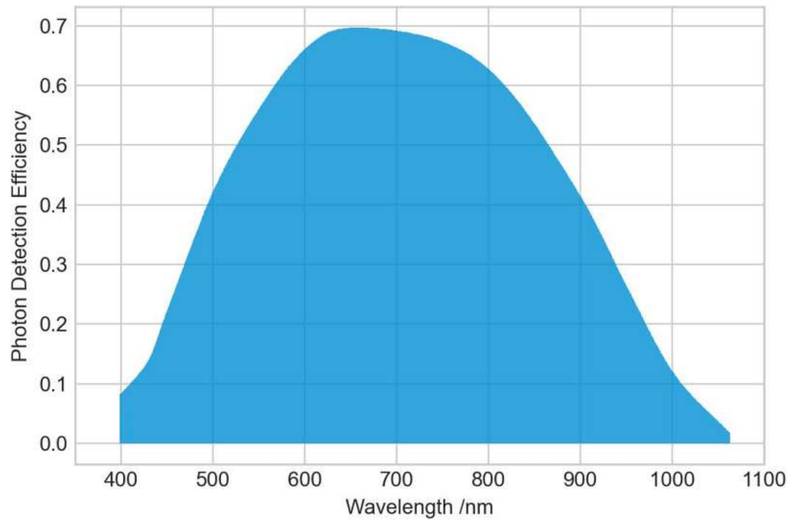

Figure 3.6.: Wavelength dependence of photon detection efficiency for the Excelitas AQRH Single photon counting module [30]

Cathodoluminescence covers a wide range of wavelengths, however our ability to detect photons is limited: we use a silicon based avalanche photodiode (Excelitas SPCM-AQRH-13-FC) in order to detect photon events. The module's quantum efficiency is wavelength-dependent, it is plotted in figure 3.6. We assume that the total detection efficiency α is a product of the collection efficiency α_{collect} at which the light emitted from the sample is collected from the sample and transmitted to the detector, with the quantum efficiency $\alpha_{\text{QE}}(\lambda)$:

$$\alpha = \alpha_{\text{collect}} \cdot \alpha_{\text{QE}}(\lambda)$$

Evidently, α_{collect} is also dependent on the wavelength to some degree, but we will assume it as constant over the wavelength range where the detector has any significant detection probability. The Vulcan system's collection solid angle is stated as 7.2 steradian by the manufacturer, corresponding to $\approx 58\%$ of full coverage. However, in our experience we typically only couple with an efficiency of 10% to 20% (mainly influenced by the alignment of the sample position). Coupling its 400 µm core multimode fibers to the SPCM-AQRH-13-FC photon detector, which has a sensitive detection area with a diameter of about 200 µm is not ideal, we assume losing a factor of 4 (from the ratio of these areas: $(400\ \mu\text{m})^2/(200\ \mu\text{m})^2 = 4$). Accounting for these inefficiencies, we will assume the estimate $\alpha_{\text{collect}} = 1\%$ where needed. Additionally, we will assume an average quantum efficiency of $\alpha_{\text{QE}} = 25\%$ over all photons in the energy range 1 eV to 3.5 eV, where needed.

TU WIEN Bibliothek Your knowledge hub

Microscope mode	Spectrometer mode	Measured	Filtered
Imaging	EFTEM	x, y,time	E_{kin},
Diffraction	EFTEM	$\frac{p_x}{p}, \frac{p_y}{p}$,time	E_{kin}
Imaging	EELS	E_{kin},time	x, y
Diffraction	EELS	E_{kin},time	$\frac{p_x}{p}, \frac{p_y}{p}$

Table 3.2.: Summary for various possible measurement configurations in the TEM

3.4. Measurement Configurations

As already described previously, four distinct measurements can be performed on the electron: transverse position x and y, deflection angle $\frac{p_x}{p}$ and $\frac{p_y}{p}$, kinetic energy E_{Kin} and arrival time t. Practically, the microscope can be set up to resolve either position, deflection angle or energy in a multi-outcome measurement using a potentially time-resolved pixelated detector. Using the microscopes various apertures, other properties can be restricted simultaneously if needed[1].
Table 3.2 summarizes the most relevant settings. When the spectrometer is set to spectrometry mode (EELS), position or momentum are automatically filtered by the use of the spectrometer entrance aperture. The desired region of the (x, y)- or $(\frac{p_x}{p}, \frac{p_y}{p})$-distribution can be selected by choosing an appropriate magnification and image shift or camera length and diffraction shift setting respectively.
Detectors like the Timepix3, which is going to be used in further experiments can include temporal resolution, i.e. they record not only at which pixel the electron has been detected, but also when. Consequently, time resolution can be obtained independently from the settings mentioned in table 3.2 and is therefore included as measured in each of them.
For example when an energy loss spectrum is recorded, one can collect electrons in diffraction mode and only accept electrons within a certain momentum range, additionally one can insert the SAD aperture to only except electrons from certain positions at the sample.

[1]In this case, one has to account for the fact that every aperture constitutes a measurement of the electron state and will therefore influence the outcome of consecutive measurements. One example of this effect is the broadening in the momentum distribution when inserting the selected area aperture: the electrons will be diffracted on the aperture.

Die approbierte gedruckte Originalversion dieser Diplomarbeit ist an der TU Wien Bibliothek verfügbar
The approved original version of this thesis is available in print at TU Wien Bibliothek.
TU WIEN Bibliothek Your knowledge hub

4. Cathodoluminescence

Cathodoluminescence (CL) is the emission of light from a material, induced by the interaction with an incident electron. Typically, this refers to wavelengths from the near infrared to the ultraviolet (200 nm - 1600 nm). The phenomenon was first observed in the mid 19th century with the invention of vacuum tubes. In 1879 W.S. Crooks delivered a lecture on cathodoluminescence to the British Association for the Advancement of Science in 1879 [31]. Since then it has been studied in much detail, a variety of review articles, such as [1],[32] or [33] provide an overview of the topic. Cathodoluminescence has been investigated in many contexts ranging from geology over material science and biology to the study of semiconductors and photonics. [1] claims that up until the early 2000s this research was mostly focused on spectroscopy i.e. only the energy distribution of the emitted photons was considered, ignoring other properties such as angular distribution, polarization and temporal distribution.

Multiple mechanism contribute to CL, in the context of this work, it is useful to distinguish between two fundamentally different types of processes: coherent cathodoluminescence and incoherent cathodoluminescence. In an incoherent process, the electron excites a quantum system within the sample, which decays after a characteristic lifetime t_{life}. The resulting photon is typically emitted in a random direction, is unpolarized and has no fixed phase relation to the field of the electron. Incoherent CL probes the excitable states of the sample. The resulting spectra can be linked to optical and electrical properties and related to other methods like optical spectroscopy. Prominent sources of incoherent CL include:

Band edge emission In semiconductors, electrons can be excited from the valence band into the conduction band. Consequently, they can de-excite, moving from the edge of the conduction band back to the valence band and emitting a photon corresponding to the resulting change in energy.

Emission from point defects Vacancies, (e.g. NV-centers in diamond) and dopant atoms can form energy levels suitable for producing CL.

In a coherent emission process, the electromagnetic field of the electron itself becomes radiative by interaction with the sample. The resulting photons maintain a

Die approbierte gedruckte Originalversion dieser Diplomarbeit ist an der TU Wien Bibliothek verfügbar
The approved original version of this thesis is available in print at TU Wien Bibliothek.
TU WIEN Bibliothek Your knowledge hub

fixed phase relation to the field of the exciting electron; they are typically polarized and emitted in a characteristic angular distribution [32]. Coherent processes include:

Cherenkov radiation is emitted from a charged particle (e.g. an electron) moving through a dielectric material at a velocity v_e that is faster than the speed of light in that material, which is determined by its refractive index n.

Transition radiation is produced by an electron approaching a conducting surface and inducing a mirror charge in the material. The system of counter propagating real charge and mirror charge can be seen as an oscillating dipole. Transition radiation is therefore only produced at interfaces.

Smith-Purcell emission takes place when a fast moving electron passes next to a periodic structure, such as an optical diffraction grating [34].

Plasmon excitation is coherent to the field of the exciting electron and decays coherently into a photon, however the decay is a random process with a characteristic lifetime.

In incoherent processes most of the correlation between a photon and the exciting electron is lost. The photon is not emitted instantaneously (e.g. within a characteristic lifetime t_{life} of the excitation), which reduces the temporal correlations. Since the overall momentum is not necessarily shared only between the electron and the photon, no momentum correlations are expected for incoherent processes on each electron photon pair. The energy loss of the exciting electron is merely an upper bound on the photon energy, as excited states can typically de-excite along multiple competing pathways.

In contrast, for coherent processes the electron and the photon are correlated in all of these quantities: Photons are emitted within the sample transition time, within a few photon wavelengths from the electron [1], obeying energy and momentum conservation.
In this work, we are interested in coherent CL, the most important emission mechanism in the systems considered here is the Cherenkov effect, which will be discussed in more detail in the following section.

[1] The excitation is caused by the electrons electric and magnetic fields, which are not localised. The phenomenon of aloof excitation suggests that the distance at which excitations can occur depend on the photon wavelength [35] this is suggested by the phenomenon

Die approbierte gedruckte Originalversion dieser Diplomarbeit ist an der TU Wien Bibliothek verfügbar
The approved original version of this thesis is available in print at TU Wien Bibliothek.
TU WIEN Bibliothek Your knowledge hub

4.1. The Cherenkov Effect

Cherenkov radiation is most prominently known as a bluish glow that emanates from a nuclear reactor as a result of the production of fast electrons in beta decay. It was first observed by Pavel Cherenkov in 1934 while studying "Compton electrons liberated in liquids in the process of scattering of γ-rays" [36]. The theoretical description of this phenomenon was found in 1937 by Ilya Frank and Igor Yevgenyevich Tamm [37] (all three received the Nobel prize for their work in 1958). What follows in this section is a summary of their findings.
In general Cherenkov radiation is emitted whenever a charged particle travels through a medium at a speed exceeding the speed of light in that medium. This is fact known as the Cherenkov condition:

$$v_{\mathrm{e}} > \frac{c}{n} \tag{4.1}$$

with v_{e} as the velocity of the incoming electron, c the speed of light in vacuum and n referring to the refractive index of the medium. A more precise formulation describes the k-vectors of photons that can be emitted by the Cherenkov effect (illustrated in figure 4.1). The electromagnetic wave must travel in phase with the electric field of the passing electron, i.e.:

$$\vec{k}_{\parallel} \cdot \vec{v}_{\mathrm{e}} \cdot t = |\vec{k}| \cdot \frac{c}{n} \cdot t$$

With $k_{\parallel}$ being the component of the k-vector that is parallel to the electron beam axis and $k_{\perp}$ being the component perpendicular to it:

$$\vec{k} = \vec{k}_{\perp} + \vec{k}_{\parallel}$$

The statement above directly implies the Cherenkov effect's second interesting feature:

$$\frac{\vec{k}_{\parallel}}{|\vec{k}|} = \frac{c}{n \cdot v_{\mathrm{e}}} \tag{4.2}$$

$$\cos(\theta_{\mathrm{Ch}}) = \frac{c}{n \cdot \beta} \tag{4.3}$$

with $\beta = \frac{v_{\mathrm{e}}}{c}$ referring to the electrons velocity as a fraction of the speed of light. Consequently, photons are always emitted at the Cherenkov angle θ_{Ch} with respect to the electron trajectory, it forms the so called Cherenkov cone (illustrated in figure 4.2).
For an infinitely long interaction region, this angular distribution would become arbitrarily sharp. In practice this is of course never the case, the angular distribution is washed out with a maximum at θ_{Ch}.

Die approbierte gedruckte Originalversion dieser Diplomarbeit ist an der TU Wien Bibliothek verfügbar
The approved original version of this thesis is available in print at TU Wien Bibliothek.
TU WIEN Bibliothek Your knowledge hub

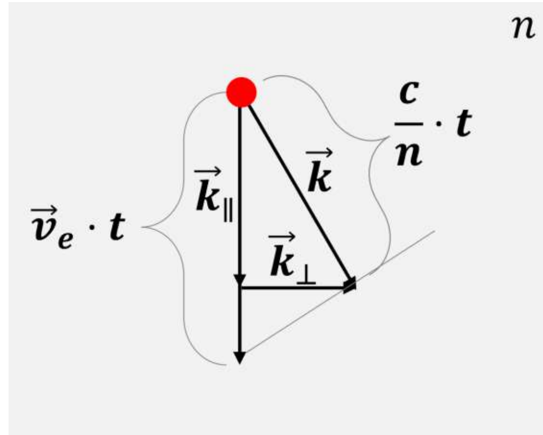

Figure 4.1.: Illustration of the restrictions on possible k-vectors for the photon due to the phase matching condition. The parallel component of the photon k-vector $k_{\parallel}$ multiplied by the distance the electron (represented by the red dot) travels within time t must equal the phase shift the photon accumulates over time t.

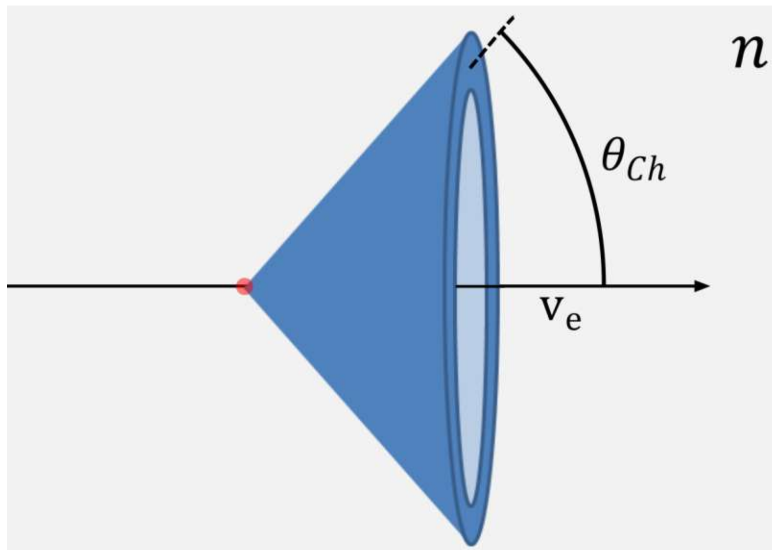

Figure 4.2.: Possible emission directions of Cherenkov radiation (blue cone) with respect to the electron velocity v_{e} when viewed in the far field, commonly referred to as the Cherenkov cone. The cone's opening angle is the characteristic Cherenkov angle θ_{Ch}.

Die approbierte gedruckte Originalversion dieser Diplomarbeit ist an der TU Wien Bibliothek verfügbar
The approved original version of this thesis is available in print at TU Wien Bibliothek.
TU WIEN Bibliothek Your knowledge hub

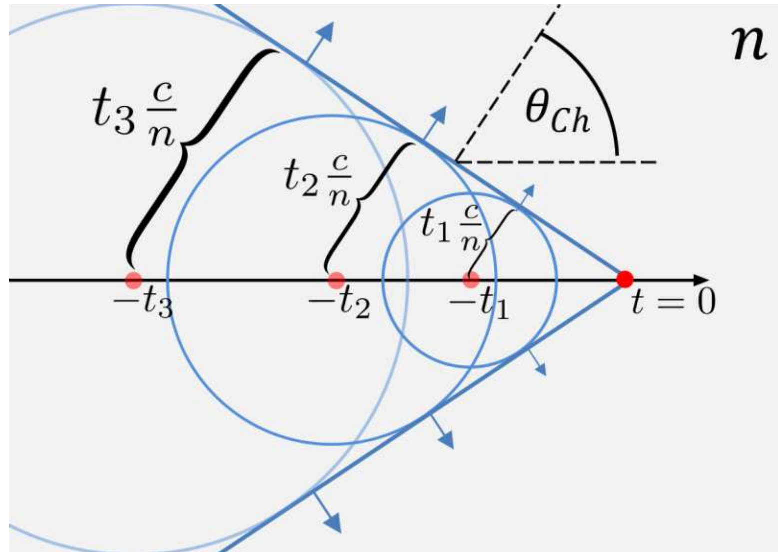

Figure 4.3.: For an electron (represented by the red dot) traveling fast enough through a medium of reflective index n (black arrow indicates electron velocity), spherical waves emitted at times t_i at different points along the electron trajectory interfere constructively along a wavefront (blue line) propagating at θ_{Ch} to the electron path.

Detailed theoretical descriptions of the Cherenkov effect can be found in various textbooks such as [38]. In order to gain a qualitative understanding, there are two very instructive ways of looking at the Cherenkov effect, which are worth highlighting. The first one is an intuition that is very similar to the idea of the ultrasonic boom.

4.1.1. Cherenkov Emission in the Wave Picture

Figure 4.3 shows a charged particle moving through a dielectric medium with a constant speed v_{e} at different points in time t_i. As the electron passes a given point $x(t_i)$, the medium at that point gets polarized: as the electron approaches, the electric field at that point increases, peaks when the electron is closest and decreases again, as it continues onward. Let's assume that this perturbation in the electric and magnetic field propagates as a spherical wave from that point. We see that for $v_{\mathrm{e}} > \frac{c}{n}$ there is a wave front at an angle θ_{Ch} where all the spherical waves emitted at different points in time are in phase and interfere constructively. The effective electric field that the electron experiences, is oriented in such a way that the particle is slowed down and deflected by it. This is obviously necessary in order to satisfy the conservation of energy and momentum between the electron and

Die approbierte gedruckte Originalversion dieser Diplomarbeit ist an der TU Wien Bibliothek verfügbar
The approved original version of this thesis is available in print at TU Wien Bibliothek.
TU WIEN Bibliothek Your knowledge hub

the photon. In this picture of the Cherenkov effect, it arises from the polarizability of the material and its field is shaped by the interference between the waves emitted from different points on the electrons trajectory, a process which is classically describable using Maxwell's equation.

4.1.2. Energy and Momentum Conservation for Cherenkov Radiation

Another way of understanding the Cherenkov effect highlights the emission of individual photons and the conservation of energy and momentum.
Assuming a refractive index that doesn't depend on the angular frequency ω, i.e. a medium that is not dispersive, the dispersion relation is simply:

$$k = \frac{2\pi}{\lambda} = \frac{\omega \cdot n}{c} \Leftrightarrow w = \frac{c}{n} \cdot k$$

This relationship defines the allowed combinations of energy and momentum that photons can carry inside the medium. Equally, for electrons the non-relativistic dispersion relation is:

$$E = \frac{p^2}{2m_\mathrm{e}}$$

Written in terms of k and ω :

$$\omega = \frac{\hbar k^2}{2m_\mathrm{e}}$$

Figure 4.4a show these two dispersion relations as well as the relativistically corrected dispersion relation for the electron. Figure 4.4b illustrates that the point with the lowest electron energy, that still permits Cherenkov radiation, is the point where $\frac{\mathrm{d}\omega_\mathrm{e}}{\mathrm{d}k_\mathrm{e}} = \frac{\mathrm{d}\omega_\gamma}{\mathrm{d}k_\gamma}$. Using the dispersion relations from above, this expression yields the familiar Cherenkov condition from Eq.: 4.1 [2].
Figure 4.5 makes this point more intuitive: below the Cherenkov threshold, i.e. at $\beta < \frac{1}{n}$, the momentum of an electron after losing the energy needed to produce a blue photon plus the momentum of said blue photon can not match the initial electron momentum at any angle. At higher electron velocities, the momenta only match for the Cherenkov angle θ_Ch. While the emission angle of the photon is independent of its wavelength, the electron recoil isn't (described in further detail in section 4.2).

[2] This observation of course has limited validity as it is restricted to the 1 dimensional dispersion relation.

Die approbierte gedruckte Originalversion dieser Diplomarbeit ist an der TU Wien Bibliothek verfügbar
The approved original version of this thesis is available in print at TU Wien Bibliothek.
TU WIEN Bibliothek Your knowledge hub

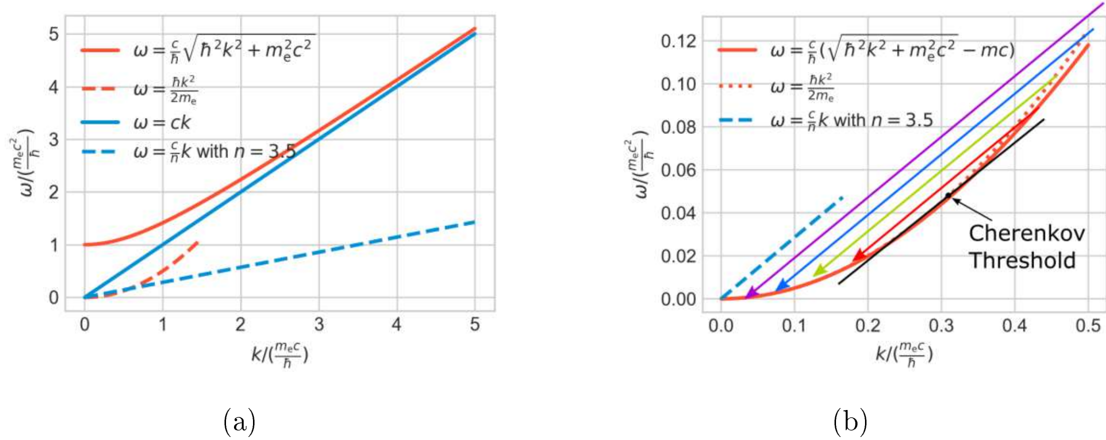

(a) (b)

Figure 4.4.: (a) Dispersion relations for electrons and photons in a material with refractive index n. (b) Condition for photon emission in one dimension: Cherenkov emission can only occur at energies exceeding the point at which the slope of the electron's dispersion relation equals the slope of the photon dispersion relation. Colored arrows represent emission processes in which energy and momentum can be conserved between the electron and the photon.

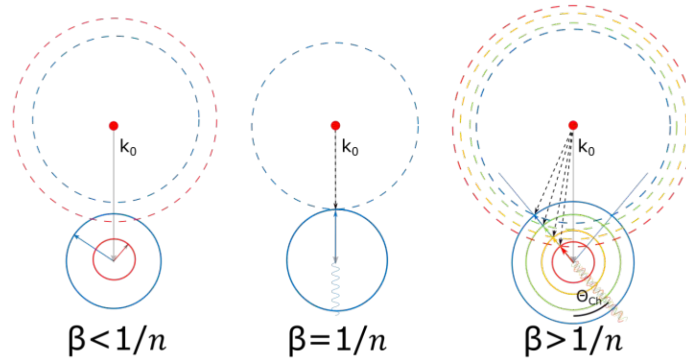

Figure 4.5.: Possible k-vectors for photons of energy $\hbar\omega_i$ (solid lines) and electrons of energy $E_0 - \hbar\omega_i$ (dashed lines) for different values of $n\beta$. Colors represent different photon energies $\hbar\omega_i$. Energy and momentum conservation can only be fulfilled for a combination of k-vectors for which the solid and the dashed circle of the respective color intersect. For $\beta < 1/n$ this is never fulfilled, for $\beta = 1/n$ it is fulfilled for photons traveling along the beam axis. For $\beta > 1/n$ it is fulfilled for photons of any energy that are emitted at an angle θ_{Ch} to the beam axis. Note that the corresponding electron deflection angle (dashed black arrows) still depends on the photon energy.

Die approbierte gedruckte Originalversion dieser Diplomarbeit ist an der TU Wien Bibliothek verfügbar
The approved original version of this thesis is available in print at TU Wien Bibliothek.
TU WIEN Bibliothek Your knowledge hub

4.1.3. Photon Emission Probability

The emission of Cherenkov photons is a probabilistic process. Assuming an electron moving in an infinitely large volume of a transparent material with refractive index n, the emitted energy per electron and unit of length $(\frac{dE}{dx})_{\text{rad}}$ can be calculated by solving Maxwell's equation. The calculation can be found in [38], the result given in SI units is:

$$(\frac{dE}{dx})_{\text{rad}} = \frac{(ze)^2}{4\pi\epsilon_0 c^2}\int_{\epsilon(\omega)>(1/\beta^2)} \omega(1-\frac{1}{\beta^2\frac{\epsilon(\omega)}{\epsilon_0}})d\omega$$

where $z{\cdot}e$ is the charge of the particle (for electrons $z=1$) and $\epsilon(\omega)$ is the dielectric function of the material. For transparent media, absorption can be neglected, i.e. $\frac{\epsilon(\omega)}{\epsilon_0} \approx n^2(\omega)$.
With Eq. 4.1, the expression can be written as:

$$(\frac{dE}{dx})_{\text{rad}} = \frac{e^2}{4\pi\epsilon_0 c^2}\int_{\epsilon(\omega)>(1/\beta^2)} \omega(1-\cos^2(\theta_{\text{Ch}}(\omega)))d\omega \tag{4.4}$$

$$= \frac{e^2}{4\pi\epsilon_0 c^2}\int_{\epsilon(\omega)>(1/\beta^2)} \omega\sin^2(\theta_{\text{Ch}}(\omega))d\omega \tag{4.5}$$

By using the relations $\omega = \frac{2\pi c}{\lambda}$ and $d\omega = -\frac{2\pi c}{\lambda^2}d\lambda$, we can write this as an integral over λ:

$$(\frac{dE}{dx})_{\text{rad}} = \frac{e^2}{4\pi\epsilon_0 c^2}\int_{\epsilon(\lambda)>(1/\beta^2)} \frac{(2\pi c)^2}{\lambda^3}\sin^2(\theta_{\text{Ch}}(\lambda))d\lambda \tag{4.6}$$

The spectrum of emitted energy is therefore:

$$\frac{d}{d\lambda}(\frac{dE}{dx})_{\text{rad}} = \frac{e^2}{4\pi\epsilon_0 c^2}\frac{(2\pi c)^2}{\lambda^3}\sin^2(\theta_{\text{Ch}}(\lambda)) \tag{4.7}$$

As a probability of photon emission P_{Ch}:

$$\Gamma_{\text{Ch}}(\lambda) = \frac{\mathrm{d}^2 P_{\text{Ch}}}{\mathrm{d}\lambda dx} = (\frac{d^2E}{d\lambda dx})_{\text{rad}}\cdot\frac{1}{\hbar\omega} \tag{4.8}$$

$$= (\frac{d^2E}{d\lambda dx})_{\text{rad}}\cdot\frac{\lambda}{2\pi\hbar c} \tag{4.9}$$

$$= \frac{2\pi e^2}{4\pi\epsilon_0\hbar c}\frac{1}{\lambda^2}\sin^2(\theta_{\text{Ch}}(\lambda)) \tag{4.10}$$

$$= \frac{2\pi\alpha}{\lambda^2}\sin^2(\theta_{\text{Ch}}(\lambda)) \tag{4.11}$$

Die approbierte gedruckte Originalversion dieser Diplomarbeit ist an der TU Wien Bibliothek verfügbar
The approved original version of this thesis is available in print at TU Wien Bibliothek.
TU WIEN Bibliothek Your knowledge hub

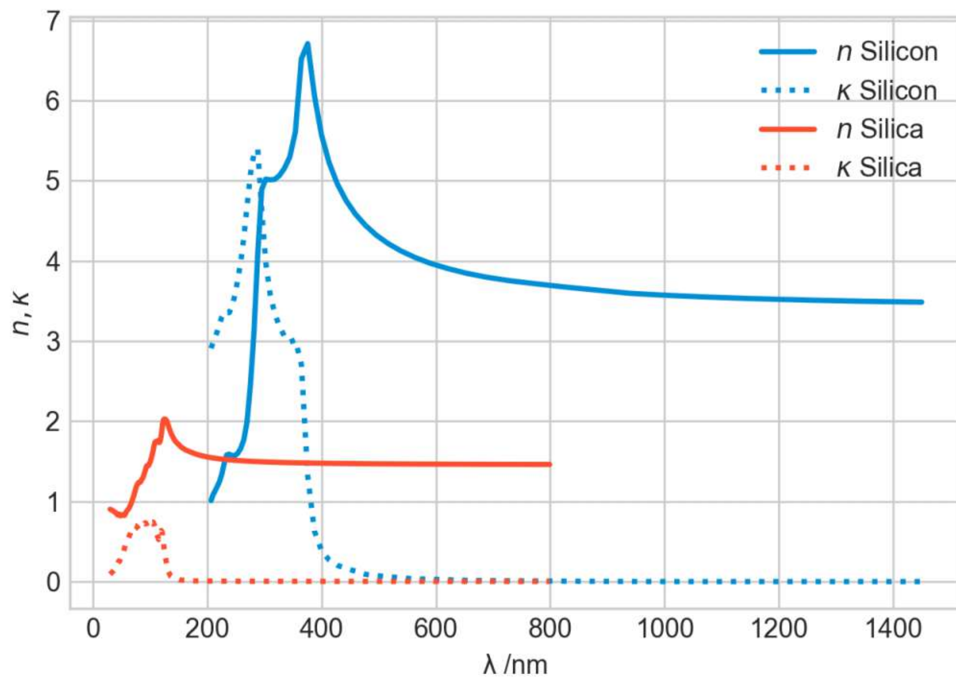

Figure 4.6.: Refractive indices n and absorption coefficients κ for crystalline silicon and silica glass (SiO2) from [41] and [42]

with $\alpha = \frac{e^2}{4\pi\varepsilon_0\hbar c}$ being the fine-structure constant. Looking at these equations, one would assume that it would be likely for the electron to emit large portions of its energy at very short wavelength Cherenkov photons. However for realistic materials this is not the case. Firstly, at UV wavelengths all materials become absorbing because at some point the photon energy to exceeds the ionization energy of the material, making it impossible to have a large enough band gap. For pushing towards this limit with suitable high band gap materials is an active field of research [39]. Secondly the refractive index drops off towards 1 at short enough. This facts is well known in the field of X-ray-optics, see [40, Chapter 4]. Figure 4.6 shows the refractive indices n and absorption coefficients κ for two prominent examples: Silicon and Silica glass. The refractive indices show a clear drop-off at 100 nm and 200 nm respectively. For 200 keV of acceleration voltage, the minimal refractive index n at which the Cherenkov condition can still be met is 1.43, below this value there is no Cherenkov emission.

Die approbierte gedruckte Originalversion dieser Diplomarbeit ist an der TU Wien Bibliothek verfügbar
The approved original version of this thesis is available in print at TU Wien Bibliothek.
TU WIEN Bibliothek Your knowledge hub

4.2. Electron Recoil

As stated previously, the emission of a Cherenkov photon implies a deflection of the electron from its original trajectory. For an acceleration voltage of $U_0 = 200$ kV it is necessary to determine the deflection angle relativistically. In the laboratory frame the energy of the incoming electron is given by:

$$E_0 = m_\mathrm{e} \cdot c^2 + E_\mathrm{Kin}$$

with:

$$E_\mathrm{Kin} = e \cdot U_0$$

where m_e is the electron mass and e is the elementary charge. As a function of particle velocity, the energy is given by:

$$E_0 = m_\mathrm{e} \cdot \gamma \cdot c^2 = m_\mathrm{e} \cdot c^2 \cdot \sqrt{\frac{1}{1-\beta^2}}$$

where:

$$\beta(E_0) = \frac{v(E_0)}{c}$$

Therefore:

$$\beta = \sqrt{1 - \frac{m_\mathrm{e}^2 \cdot c^4}{E_0^2}}$$

The incoming electron's four momentum is given by:

$$\mathbf{p}_0 = \begin{pmatrix} \frac{E_0}{c} \\ \vec{p}_0 \end{pmatrix} = m_\mathrm{e} \cdot \gamma \cdot \begin{pmatrix} c \\ \vec{v} \end{pmatrix} = \begin{pmatrix} \frac{E_0}{c} \\ 0 \\ 0 \\ -m_\mathrm{e} \cdot \gamma \cdot v_\mathrm{e} \end{pmatrix}$$

Additionally, the Cherenkov condition 4.1 defines the four-momentum of the outgoing photon as a function of its wavelength:

$$\mathbf{p}_\gamma = \begin{pmatrix} \frac{\hbar\omega}{c} \\ \vec{e}_\perp \cdot \hbar|k| \cdot \sin(\theta_\mathrm{Ch}) \\ -\hbar|k| \cdot \cos(\theta_\mathrm{Ch}) \end{pmatrix}$$

$|k| = \frac{2\pi n}{\lambda}$ in this case refers to the photon momentum in the material, $\vec{e}_\perp$ is the unit vector perpendicular to the initial electron trajectory.
Assuming that four momentum is conserved between the electron and the emitted photon, the final momentum $\mathbf{p}_f$ can be calculated:

$$\mathbf{p}_f = \mathbf{p}_0 - \mathbf{p}_\gamma = \begin{pmatrix} \frac{E_0 - \hbar\omega}{c} \\ -\vec{e}_\perp \cdot \hbar|k| \cdot \sin(\theta_\mathrm{Ch}) \\ -m_\mathrm{e} \cdot \gamma \cdot v_\mathrm{e} + \hbar|k| \cdot \cos(\theta_\mathrm{Ch}) \end{pmatrix}$$

Die approbierte gedruckte Originalversion dieser Diplomarbeit ist an der TU Wien Bibliothek verfügbar
The approved original version of this thesis is available in print at TU Wien Bibliothek.
TU WIEN Bibliothek Your knowledge hub

The deflection angle θ_e with respect to the initial electron trajectory is therefore:

$$\theta_\mathrm{e} = \arctan(\frac{\hbar|k| \cdot \sin(\theta_\mathrm{Ch})}{m_\mathrm{e} \cdot \gamma \cdot v_\mathrm{e} - \hbar|k| \cdot \cos(\theta_\mathrm{Ch})}) \tag{4.12}$$

4.3. Distribution of Electron Recoil

As discussed in 4.2, the distribution of wavelength λ of emitted Cherenkov photons in the bulk limit is given by Eq.4.11.

$$\Gamma_\mathrm{Ch}(\lambda) = \frac{\mathrm{d}^2 P_\mathrm{Ch}}{\mathrm{d}\lambda dx} = \frac{2\pi\alpha}{\lambda^2} \sin^2(\theta_\mathrm{Ch}(\lambda)) \tag{4.13}$$

The deflection of the electron due to the emission of a photon can be written as a function of λ (see Eq. 4.12):

$$\theta_\mathrm{e}(\lambda) = \arctan(\frac{\hbar|k| \cdot \sin(\theta_\mathrm{Ch}(\lambda))}{m_\mathrm{e} \cdot \gamma \cdot v_\mathrm{e} - \hbar|k| \cdot \cos(\theta_\mathrm{Ch}(\lambda))})$$

If $\theta_\mathrm{e}(\lambda)$, given by Eq. 4.12 is an invertible function, the probability distribution over the deflection angle is given by:

$$\frac{d^2 P_\mathrm{Ch}}{d\theta_\mathrm{e} dx} = \frac{d^2 P_\mathrm{Ch}}{d\lambda dx} \cdot |\frac{d\lambda}{d\theta_\mathrm{e}}|$$

The full expression can be calculated analytically, however it is more instructive to look at a strong simplification. For the case of $n = \mathrm{const}$ and for visible wavelengths, one can approximate:

$$\theta_\mathrm{e}(\lambda) \approx \frac{\hbar|k| \cdot \sin(\theta_\mathrm{Ch})}{m_\mathrm{e} \cdot \gamma \cdot v_\mathrm{e} \cdot (1 - \frac{\hbar|k| \cdot \cos(\theta_\mathrm{Ch})}{m_\mathrm{e} \cdot \gamma \cdot v_\mathrm{e}})}$$

taking the photon momentum to be small compared to the initial electron momentum, i.e. $\hbar|k| \ll m_\mathrm{e} \cdot \gamma \cdot v_\mathrm{e}$, one sees that:

$$\theta_\mathrm{e}(\lambda) \propto \frac{1}{\lambda} \tag{4.14}$$

$$\frac{d^2 P_\mathrm{Ch}}{d\lambda dx} \propto \frac{1}{\lambda^2} \tag{4.15}$$

Therefore:

$$\frac{d^2 P_\mathrm{Ch}}{d\theta_\mathrm{e} dx} = \frac{d^2 P_\mathrm{Ch}}{d\lambda dx} \cdot \frac{1}{|\frac{d\theta_\mathrm{e}}{d\lambda}|} \propto \frac{1}{\lambda^2} \cdot \frac{1}{\frac{1}{\lambda^2}} \approx \mathrm{const}$$

Die approbierte gedruckte Originalversion dieser Diplomarbeit ist an der TU Wien Bibliothek verfügbar
The approved original version of this thesis is available in print at TU Wien Bibliothek.
TU WIEN Bibliothek Your knowledge hub

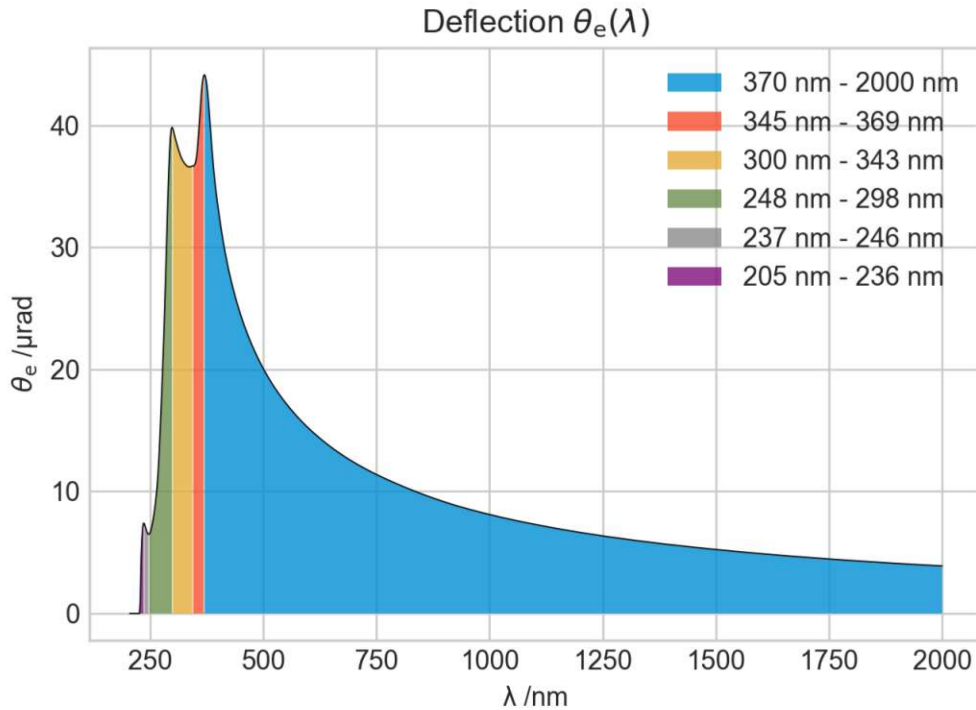

Figure 4.7.: Deflection angle due to Cherenkov emission in crystalline silicon as a function of wavelength. Colors delimit monotonous segments.

In this very simplified case, electrons that emit a Cherenkov photon are deflected by the corresponding angle. The probability distribution of photon wavelengths, lead to a uniform distribution in the deflection angle θ_e. Deviations from this behavior in $\frac{d^2P_\mathrm{Ch}}{d\theta_\mathrm{e}dx}$ for realistic materials is due to the change in θ_Ch and therefore due to dispersion, i.e. $n = n(\lambda)$.

Figure 4.7 shows the deflection angle θ_e as a function of λ, taking into account the dispersion of silicon, which is shown in figure 4.6. As is the case for all realistic dispersion relations, $\theta_\mathrm{e}(\lambda)$ is not monotonous, therefore the relation describing $\frac{d^2P_\mathrm{Ch}}{d\theta_\mathrm{e}dx}$ is more complicated: $\theta_\mathrm{e}(\lambda)$ must be divided into monotonous segments $\theta_\mathrm{i}'(\lambda)$ over the corresponding wavelength intervals $\mathcal{I}_i$, this is also indicated in figure 4.7.

Die approbierte gedruckte Originalversion dieser Diplomarbeit ist an der TU Wien Bibliothek verfügbar
The approved original version of this thesis is available in print at TU Wien Bibliothek.
TU WIEN Bibliothek Your knowledge hub

$\frac{d^2 P_{\mathrm{Ch}}}{d\theta_{\mathrm{e}} dx}$ is then given by a sum over the individual contributions of these segments:[3]

$$\frac{d^2 P_{\mathrm{Ch}}}{d\theta_{\mathrm{e}} dx} = \sum_i \int_{\mathcal{I}_i} d\lambda' \delta(\theta_{\mathrm{e}}(\lambda') - \theta_{\mathrm{e}}(\lambda)) \cdot \frac{d^2 P_{\mathrm{Ch}}}{d\lambda dx} \cdot |\frac{d\lambda}{d\theta_{\mathrm{e}}}|$$

This indicates that photons at different wavelengths deflect electrons into the same deflection angle. In silicon, the extinction coefficient κ suppresses Cherenkov emission in the ultraviolet, making contributions of $\lambda < 350$ nm irrelevant. In order to account for this, I simply multiply $\frac{d^2 P_{\mathrm{Ch}}}{d\lambda dx}$ by a factor accounting for the extinction of light in the medium [43, Chapter 4]:

$$P_{\mathrm{Lambert-Beer}}(\lambda) = L \cdot \frac{d^2 P_{\mathrm{Ch}}}{d\lambda dx} \cdot e^{-\frac{4\pi\kappa L}{\lambda}}$$

Figure 4.8 shows the probability density over θ_{e} assuming an interaction length L of 100 nm in bulk silicon, when taking into account the extinction coefficient κ. The symbol λ refers to the wavelength of the photon in vacuum.

[3] As is to be expected, the deflection probability density diverges where $\frac{d\theta_{\mathrm{e}}}{d\lambda}(\lambda) = 0$, the function is still integrable: Any interval $\mathcal{I} = [(\theta_{\mathrm{e}})_{\mathrm{min}}, (\theta_{\mathrm{e}})_{\mathrm{max}}]$ corresponds to multiple wavelength intervals $\mathcal{I}_i' = [\lambda_{\mathrm{min}}, \lambda_{\mathrm{max}}]$ where $\lambda \in \mathcal{I}_i' \implies \theta_{\mathrm{e}}(\lambda) \in \mathcal{I}$. As the probability of photon emission into any wavelength interval $P_{\mathrm{Ch}}(\lambda \in \mathcal{I}_i')$ is bounded according to Eq. 4.11, $P_{\mathrm{Ch}}(\theta_{\mathrm{e}} \in \mathcal{I})$ is bounded by the sum of of the probabilities for photon emission into these intervals:

$$P_{\mathrm{Ch}}(\theta_{\mathrm{e}} \in \mathcal{I}) < \sum_i P_{\mathrm{Ch}}(\lambda \in \mathcal{I}_i')$$

Die approbierte gedruckte Originalversion dieser Diplomarbeit ist an der TU Wien Bibliothek verfügbar
The approved original version of this thesis is available in print at TU Wien Bibliothek.
TU WIEN Bibliothek Your knowledge hub

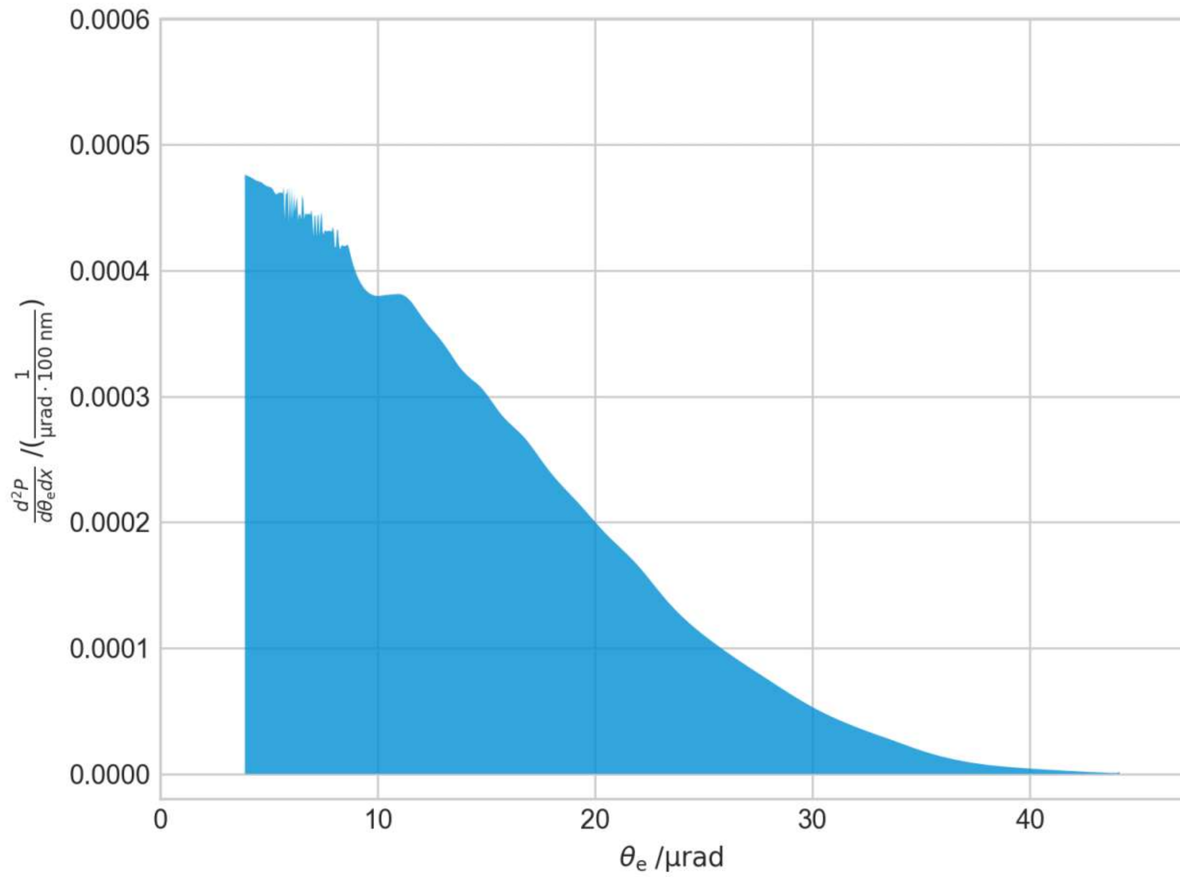

Figure 4.8.: Probability density an electron to be deflected by a deflection angle θ_e due to the emission of a Cherenkov photon, for an interaction length of 100 nm in silicon, normalized to 1 µrad.

Die approbierte gedruckte Originalversion dieser Diplomarbeit ist an der TU Wien Bibliothek verfügbar
The approved original version of this thesis is available in print at TU Wien Bibliothek.
TU WIEN Bibliothek Your knowledge hub

5. Coincidence Measurements

What has been explained so far on Cherenkov emission, elastic and inelastic scattering is well established theory. In the light of this interpretation it seems natural to talk about individual electrons emitting individual photons. Most experiments performed so far however did not include correlated measurements of one individual electron and one individual photon. What was observed instead were typically electron and photon distributions [4][5]. One would for example collect an electron energy loss spectrum and a spectrum of the emitted light and note that the distribution of lost electron energy roughly corresponds to the energy of the emitted light. Or one would measure the angular distribution of the photons and the angular distribution of the electrons and note that both could be explained by the electron emitting a photon and, due to conservation of momentum, receiving a kick.

As already mentioned in section 4, photons emitted by coherent processes are emitted in phase with the field of the emitting electron. This fact leads to a strong correlation between the detection time of the emitted photon and the detection time of the electron that has undergone emission. In this section I will explain how and under which condition this correlation can be utilized to identify which photon was emitted by which electron.

To illustrate the basic principle a simple situation is considered: The beam is focused onto a sample and irradiates it with i electrons per second. An ideal electron lens images the illuminated spot on the sample plane onto the detector.

One electron enters the sample and emits a photon at time t_0, both electron and photon continue propagating through the experimental setup and are finally detected at the respective times t_e and t_γ. The transition times from the sample to the respective detectors $t_\mathrm{e} - t_0$ and $t_\gamma - t_0$ and the corresponding detector delays are known, therefore the time delay between the two signals $\Delta t_{\mathrm{e}\gamma} = t_\mathrm{e} - t_\gamma$ that corresponds to simultaneous emission from the sample can be determined. As our photon and our electron indeed arrive with this delay, the two detection events are grouped together and labeled as one coincidence event.

In this work, the term "coincidence event" refers to a pair of one photon detection and one electron detection, that is classified to have been part of the same coherent emission process.

Unfortunately due to various reasons (e.g. the sample thickness, detector jitter, electron energy spread,...) the transition and detection times are not fixed but

Die approbierte gedruckte Originalversion dieser Diplomarbeit ist an der TU Wien Bibliothek verfügbar
The approved original version of this thesis is available in print at TU Wien Bibliothek.
TU WIEN Bibliothek Your knowledge hub

randomly distributed. Their expected values $\mathbb{E}[t_e - t_0]$ and $\mathbb{E}[t_\gamma - t_0]$ can be determined which gives us an expected time delay $\mathbb{E}[\Delta t_{e\gamma}] = \mathbb{E}[t_e - t_\gamma]$. In order to still register the electron photon pair from above, we have to accept electron detections and photon detections not only if their delay is precisely $\mathbb{E}[\Delta t_{e\gamma}]$ but for all delays within an interval $[\mathbb{E}[\Delta t_{e\gamma}] - \tau/2, \mathbb{E}[\Delta t_{e\gamma}] + \tau/2]$, with the bin with $\tau > 0$.
The situation described above will be referred to from now on as a "true coincidence event": an electron emits a photon, both particles get detected, their time delay is within the accepted interval and they are *correctly* classified as having been part of the same coherent emission process.
As soon as we extend the allowed values for $\Delta t_{e\gamma}$ to a finite interval, we open up the possibility of registering "false coincidence events", i.e. pairs of detections that are *wrongly* classified as having been part of the same coherent emission process.
Let's for example consider an alternative situation, this time taking into account the detection probabilities for both the electron and the photon are smaller than one: *Two* electrons traverse the sample in short succession ($|t_1 - t_2| < \tau$), one emits a photon but doesn't get detected in the electron detector, the other gets detected but hasn't emitted a photon. The two detections are registered at an acceptable value of $\Delta t_{e\gamma}$ and yield a false coincidence event.
Practically, the experiment will be conducted by sorting all detections into time bins of duration τ, each of these time bins is a realization of one of five distinct situations, which are relevant for interpreting coincidence experiments:

No electron detected No electron is detected within the time bin.

Excluded More than one electron or more than one photon was detected.

No Coincidence (true negative) Only an electron was detected, it did not coherently emit a photon.

Missed coincidence event (false negative) Only an electron was detected, the corresponding coherently emitted photon was not detected.

True coincidence event (true positive) Precisely one electron was detected in coincidence with its corresponding coherently emitted photon.

False coincidence event (false positive) Precisely one electron was detected in the same time bin as an uncorrelated photon.

These different categories of events are illustrated in figure 5.1.
By characterizing the experimental setup, the proportion of true and false coincidence events can be determined. Intuitively, the lower the fraction of false coincidence events is, the more reliable observations on electron-photon pairs are. The rest of this section is going to present this characterization.

Die approbierte gedruckte Originalversion dieser Diplomarbeit ist an der TU Wien Bibliothek verfügbar
The approved original version of this thesis is available in print at TU Wien Bibliothek.
TU WIEN Bibliothek Your knowledge hub

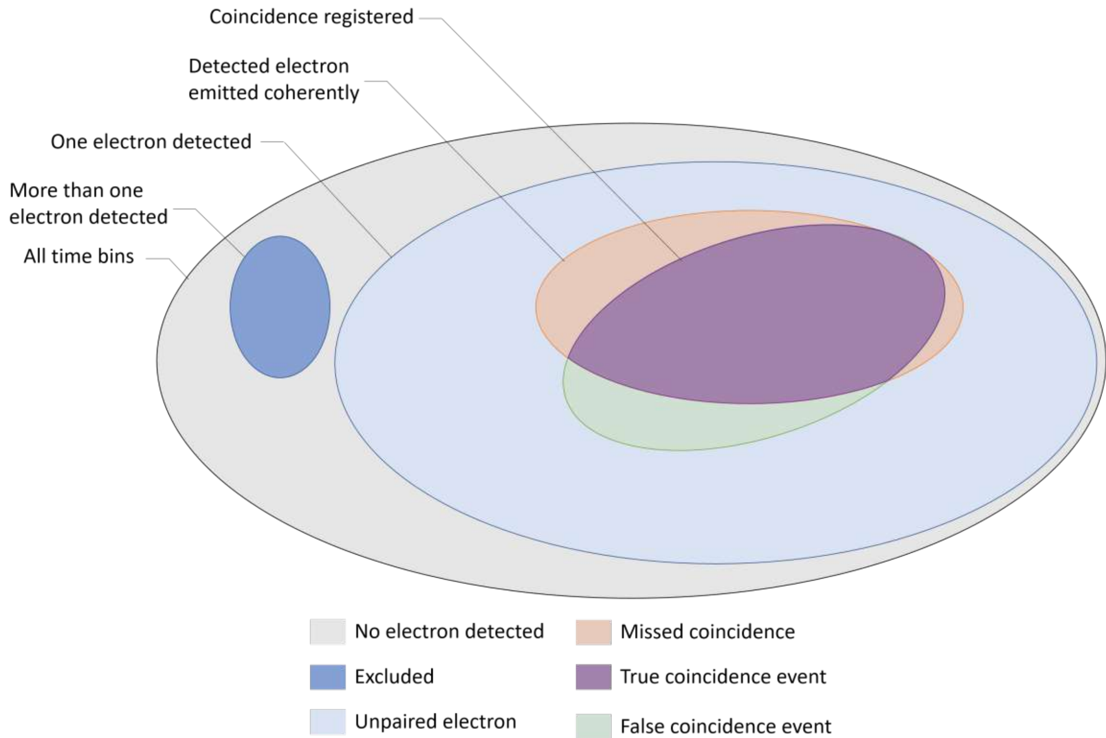

Figure 5.1.: This figures graphically illustrates possible outcomes for each time bin of length τ. Ellipses represent subsets of all time bins, all time bins contained in an ellipse fulfill the condition stated in its label. Colors indicate the relevant categories the time bins can fall into. This classification does not take the possibility of multiple photons falling into the same time bin into account.

5.1. Average Rates

The sample is irradiated with i electrons per second, therefore the rate R_e of detected electrons per second is approximately:

$$R_\mathrm{e} \approx i \cdot \alpha_\mathrm{e} + R_\mathrm{eDC} \tag{5.1}$$

where α_e is the probability of detecting an electron and R_eDC is the electron detector's dark count rate, which is typically very low. The statement is approximate because all detectors deviate from this ideal behavior to some extend, e.g. due to having a certain dead time after each detection within which no second electron can be detected. It's assumed that the detector is operated far below its saturation level.

Die approbierte gedruckte Originalversion dieser Diplomarbeit ist an der TU Wien Bibliothek verfügbar
The approved original version of this thesis is available in print at TU Wien Bibliothek.
TU WIEN Bibliothek Your knowledge hub

The detected rate of photon counts is approximately given by:

$$R_\gamma \approx i\alpha_\gamma p + R_{\gamma\mathrm{DC}} \tag{5.2}$$

where p is the average number of photons emitted by each electron and α_γ[1] is the probability of photon detection, this term includes factors like the limited collection angle of the detection system or the quantum efficiency of the detectors. $R_{\gamma\mathrm{DC}}$ is the dark count rate of the photon detector. Note that p includes both the average number of coherent photons emitted directly p_{coh} and the average number of photons emitted via an excitation decaying later in time p_{in}:

$$p = p_{\mathrm{coh}} + p_{\mathrm{in}}$$

Once again Eq.5.1 is only approximate, the issue of dead time brings in an additional complication as it explicitly suppresses counts from multiple coherent photons emitted by the same electron. However photon emission probabilities are typically small and electron currents can be easily reduced to a level at which Eq. 5.1 is a good approximation.

5.2. Temporal Distributions

The emission of electrons from the source is modeled as an equiprobable distribution in time, electrons are emitted independently from each other at random times with an average rate of i electrons per second.[2] The probability to find n_e electrons within any given time interval τ is therefore given by a Poissonian distribution [44]:

$$\mathcal{P}_\lambda(n_\mathrm{e}) = \frac{\lambda^{n_\mathrm{e}} e^{-\lambda}}{n_\mathrm{e}!}$$

where $\lambda = i\tau$ is the expected value of the amount of electrons in that interval. Coming back to the example of two electrons passing through the column in close succession, this relation can be used to calculate the probability of encountering two or more electrons in the same time interval:

$$\mathcal{P}_{i\tau}(n_\mathrm{e} \geq 2) = 1 - e^{-i\tau} - i\tau e^{-i\tau} \tag{5.3}$$

[1] This quantity is assumed to be a constant parameter of the setup here, however as it can depend on the emission angle and wavelength of the photon, this is a simplification.

[2] This assumption is commonly used, even though theoretically antibunching between the electrons due to Coulomb repulsion and the electrons fermionic nature, however the effect must be very small [44].

Die approbierte gedruckte Originalversion dieser Diplomarbeit ist an der TU Wien Bibliothek verfügbar
The approved original version of this thesis is available in print at TU Wien Bibliothek.
TU Bibliothek Your knowledge hub WIEN

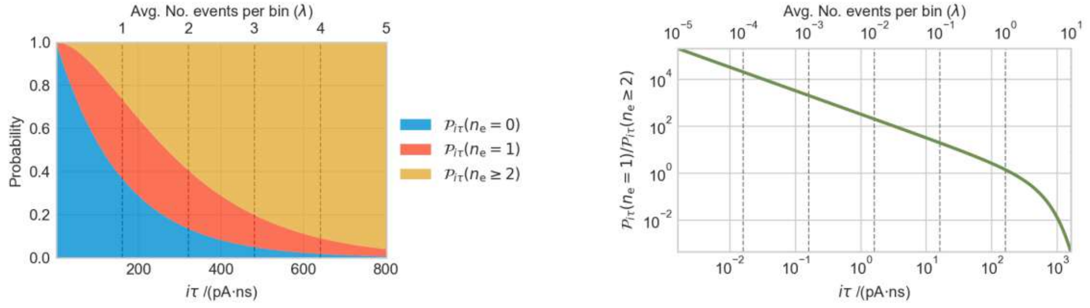

(a) Fractions of time bins containing 0, 1, and ≥ 2 electrons as a function current i and bin width τ assuming a Poissonian distribution.

(b) Fraction of bins containing 1 electrons divided by fraction of bins containing 2 or more.

Figure 5.2.

The result is illustrated in figure 5.2, it decreases significantly for low currents and short time intervals.

The probability distribution of the number of coherently emitted photons per electron highly depends on the situation considered (as dicussed for various cases in [45]). The experiment described in [46] is similar to our situation in that it features a passive sample coherently interacting with the electron beam. Here photons are emitted according to a Poissonian distribution defined by the average number of emitted photons. However, the sample in this publication is highly mode- and wavelength selective, which is central a condition in the derivation of the corresponding theoretical description and does not hold in our case.

As the possibility of multiple photon emission is disregarded in the scope of this work, we will assume the coherent photon emission probability to be:

$$P_\gamma(n_{\text{coh}} = 0) \approx 1 - p_{\text{coh}} \tag{5.4}$$

$$P_\gamma(n_{\text{coh}} = 1) \approx p_{\text{coh}} \tag{5.5}$$

$$P_\gamma(n_{\text{coh}} > 1) \approx 0 \tag{5.6}$$

$$\tag{5.7}$$

Being more precise and taking multiple electrons into account, a binomial distribution has to be assumed, as the process can occur for any electron independently:

Die approbierte gedruckte Originalversion dieser Diplomarbeit ist an der TU Wien Bibliothek verfügbar
The approved original version of this thesis is available in print at TU Wien Bibliothek.
TU WIEN Bibliothek Your knowledge hub

$$P_\gamma(n_{\mathrm{coh}}|n_{\mathrm{e}}) = \mathcal{B}(n_{\mathrm{coh}} \mid p_{\mathrm{coh}}, n_{\mathrm{e}}) \tag{5.8}$$

$$= \begin{cases} \binom{n_{\mathrm{e}}}{n_{\mathrm{coh}}} p_{\mathrm{coh}}^{n_{\mathrm{coh}}} (1-p_{\mathrm{coh}})^{n_{\mathrm{e}}-n_{\mathrm{coh}}} & \text{for} \quad n_{\mathrm{coh}} \in \{0,1,\ldots,n_{\mathrm{e}}\}, \\ 0 & \text{otherwise.} \end{cases} \tag{5.9}$$

The probability for exactly one coherent emission from exactly one electron to occur in any given time interval is therefore:

$$\mathcal{P}_{i\tau}(n_{\mathrm{e}}=1) \cdot P_\gamma(n_{\mathrm{coh}}=1|n_{\mathrm{e}}=1) = i\tau e^{-i\tau} \cdot p_{\mathrm{coh}} \tag{5.10}$$

The background processes that need to be considered, can also be described as following a Poissonian distribution. For electron and photon dark counts:

$$\lambda_{\mathrm{eDC}} = \tau R_{\mathrm{eDC}}$$

and

$$\lambda_{\gamma\mathrm{DC}} = \tau R_{\mathrm{DC}}$$

For incoherent photons:

$$\lambda_{\mathrm{in}} = \tau i p_{\mathrm{in}}$$

5.3. Signal to Noise Ratio in Coincidence Measurements

Eq. 5.2 gives the probability to encounter precisely one electron and one coherently emitted photon in any given time bin. By multiplying this expression with the number of time bins per second, which is given by $\frac{1}{\tau}$, an expression for the rate of coincidence events per second can be obtained. Multiplying this rate with the electron detection efficiency α_{e} and the photon detection efficiency α_γ yields an expression for the expected number of true coincidence events per second:

$$\begin{aligned} R_{\mathrm{Coin}} &= \frac{1}{\tau}\alpha_{\mathrm{e}}\alpha_\gamma \mathcal{P}_{i\tau}(n_{\mathrm{e}}=1) \cdot P_\gamma(n_{\mathrm{coh}}=1|n_{\mathrm{e}}=1) \\ &= i\alpha_{\mathrm{e}} e^{-i\tau} \cdot \alpha_\gamma p_{\mathrm{coh}} \end{aligned}$$

In order to estimate the number of false coincidence events, two main contributions are considered:

TU WIEN Bibliothek Your knowledge hub
Die approbierte gedruckte Originalversion dieser Diplomarbeit ist an der TU Wien Bibliothek verfügbar
The approved original version of this thesis is available in print at TU Wien Bibliothek.

- The probability to detect a coincidence between a noise photon and an electron is given by the rate at which incoherent photons are detected and the dark count rate. For each of these detections on the photon side, there is a probability of detecting exactly one electron in the same time interval τ, given by a Poissonian distribution:

$$R_{\text{Wrong }\gamma} = (i\alpha_\gamma p_{\text{in}} + R_{\gamma\text{DC}}) \cdot \tau(i\alpha_{\text{e}} + R_{\text{eDC}}) \cdot e^{-\tau(i\alpha_{\text{e}}+R_{\text{eDC}})} \tag{5.11}$$

- An upper bound on the probability to detect a coherently emitted photon in coincidence with a wrong electron can be estimated by looking at Eq. 5.2. The rate corresponding to the probability to find $n_{\text{e}} > 1$ electrons in the same time bin, one or more of them coherently emitting a photon, again neglecting higher orders of p_{coh} and detecting exactly 1 out of these n_{e} electrons [3] is given by:

$$R_{\text{Wrong e}^-} = \frac{1}{\tau}\sum_{n_{\text{e}}>1}(n_{\text{e}}\alpha_\gamma p_{\text{coh}}) \cdot \mathcal{P}_{\text{i}\tau}(n_{\text{e}}) \cdot n_{\text{e}}\alpha_{\text{e}}(1-\alpha_{\text{e}})^{n_{\text{e}}-1} \tag{5.12}$$

$$= \alpha_\gamma p_{\text{coh}}\tau i^2 e^{-i\tau} \cdot 2\alpha_{\text{e}}(1-\alpha_{\text{e}}) + O(\tau^2, i^3) \tag{5.13}$$

The factor $n_{\text{e}}\alpha_{\text{e}}(1-\alpha_{\text{e}})^{n_{\text{e}}-1}$ is the probability of drawing exactly one out of n_{e} samples from a binominal distribution with probability α_{e}.

In conclusion, for $i\tau << 1$, the (true) coincidence rate is proportional to i and the noise (false coincidence rate) ignoring the contribution of dark counts is at least [4] proportional to i^2 and τ. Therefore it is desirable to measure at the lowest practical current (limited by the available measurement time and the long term stability of the instrument) and the best attainable time resolution (limited by the jitter of the instrument).
The signal to noise ratio, defined analogously to [47] is given by:

$$\text{SNR} = \frac{R_{\text{Coin}}\sqrt{T}}{\sqrt{R_{\text{Coin}} + R_{\text{Wrong }\gamma} + R_{\text{Wrong e}}}} \tag{5.14}$$

It increases with the square root of the total measurement time T.

[3] This expression neglects the contribution of electron dark counts, which is typically a reasonable assumption, as the dark count rate of modern direct detection cameras are very low. The full expression including this contribution is:

$$R_{\text{Wrong e}^-} = \frac{1}{\tau}\sum_{n_{\text{e}}>1}(n_{\text{e}}\alpha_\gamma p_{\text{coh}}) \cdot \mathcal{P}_{\text{i}\tau}(n_{\text{e}}) \cdot [n_{\text{e}}\alpha_{\text{e}}(1-\alpha_{\text{e}})^{n_{\text{e}}-1} + \tau R_{\text{eDC}}(1-\alpha_{\text{e}})^{n_{\text{e}}}] \cdot e^{-\tau R_{\text{eDC}}}$$

[4] to be understood as: $R_{\text{Wrong e}^-} = O(i^2)$ and $R_{\text{Wrong }\gamma} = O(i^2))$ for small values of i and τ

Die approbierte gedruckte Originalversion dieser Diplomarbeit ist an der TU Wien Bibliothek verfügbar
The approved original version of this thesis is available in print at TU Wien Bibliothek.
TU WIEN Bibliothek Your knowledge hub

5.4. Correlations

Having established criteria to correctly determine electron-photon pairs, this section will summarize qualitatively what is needed for measurements on the two constituent particles of these electron-photon pairs to yield correlated results.

The pairs of potential measurements considered are:

- Transverse[5] electron momentum with transverse photon momentum
- Position of the electron with position of the photon (by imaging the sample plane onto the detector)
- Electron energy with photon energy
- Time of electron detection with time of photon detection (as already discussed in section 5)

Firstly, a setup is needed that allows for both the electron and the photon to be detected. On the photon side this is a question of material and geometry: we are for the most part interested in transparent media, i.e. the photon should be produced in a material from which it can escape. The geometry should not block the photon from being transmitted to the detector. On the electron side this means that the electron needs to be transmitted through the sample (or pass very close to it, see section 6.1). As electrons interact strongly with matter, they are typically not able to penetrate more than a couple of hundreds of nanometers of material, where materials with a high atomic number Z show a larger extinction than low Z materials.
Secondly, coherent emission should occur with high probability in the setup. As already stated in section 4, clear correlations between measurements on the photon and measurements on the electron are only expected for coherent emission processes, while incoherent emission contributes only to noise (see section 5.3). In our experiments, Cherenkov radiation is the process of interest that we wish to optimize for. We therefore favor high acceleration voltages and materials with a large refractive index, additionally a large interaction region between the electron and the material is favorable, as the emission probability scales linearly with the interaction length. (see section 4.1)
Thirdly, the setup should preserve correlations between electron and photon. In order to **preserve correlations in detection time**, unknown delays on both electron and photon should be avoided, the most obvious source of this is jitter on the respective detectors.

[5]"Transverse" meaning perpendicular to the beam axis in this context.

Die approbierte gedruckte Originalversion dieser Diplomarbeit ist an der TU Wien Bibliothek verfügbar
The approved original version of this thesis is available in print at TU Wien Bibliothek.
TU WIEN Bibliothek Your knowledge hub

Preserving correlations in energy implies avoiding unknown changes in energy to both particles. The photon energy is preserved in all cases that have been considered over the course of this project so far. Electron energy can vary because there is a probability of an electron to undergo multiple inelastic scattering processes when interacting with the sample. These are to be avoided either by minimizing the interaction length between electron and material (potentially at the cost of a lower photon production probability) or by having the electrons interact with the sample in an aloof configuration. Alternatively, an upper bound on the electron energy loss can be implemented by detecting coincidences after the electron energy filter.

We have to assume that **preserving correlations in momentum** is the biggest challenge. As it is the case for electron energy, multiple scattering of the electron should be avoided, especially elastic scattering is undesirable, because it cannot be dealt with by filtering the electron energy loss. On the photon side, elastic photon scattering occurs in principle at every mirror and every interface between two media. Correlation can be lost, when the changes to photon momentum are unknown. Consider for example a photon that is transmitted through a narrow slit, the photon will be diffracted to a random angle and (directional) correlation to the electron momentum will be lost.

Correlations in position can equally be lost due to scattering on both the electron and the photon side. A practically relevant example is the emission of photons into guided modes: Imagine a photon being emitted inside a thin film at position x, it can propagate inside the film to position x' before being scattered out of the material, an imaging system observing the surface of the film would detect the photon at x'.

Die approbierte gedruckte Originalversion dieser Diplomarbeit ist an der TU Wien Bibliothek verfügbar
The approved original version of this thesis is available in print at TU Wien Bibliothek.
TU WIEN Bibliothek Your knowledge hub

6. Cherenkov in Complex Geometries

The theory of Cherenkov radiation presented so far has referred to the bulk case: a charged particle moving in an infinite bulk of dielectric material without boundaries. This is the case that produces the characteristic angular distribution of the Cherenkov effect. However, the coherent emission from a (micro-/nano-) structure generally depends on the structure's geometry. Various papers discuss cathodoluminescence in different geometries, in this work three situations are particularly interesting: emission in a thin film at normal incidence, aloof emission near a plane interface and aloof emission from a sphere, all of which are discussed in [48] (The first two cases have already first been treated in 1968 and 1983 respectively, see [49] and [35]).

6.1. Thin Membranes

The most promising of the configurations that were investigated experimentally, is a thin membrane of crystalline silicon. A large area of the membrane is illuminated using a collimated electron beam. The boundary conditions of a thin slab modify the probability for coherent photon emission significantly. For our particular experiment, theoretical predictions for this case were kindly provided by Dr. Andrea Konečná from CEITEC, Brno [50]. They were calculated assuming a point-like charge traversing the sample at normal incidence, by solving Maxwell's equations in Fourier space, taking the dielectric function ϵ for crystalline silicon measured in [51] and ignoring the material's magnetic permeability, i.e. setting $\mu = 1$. The calculations include simulated broadening due to energy and momentum spread in the initial beam by convolution with a realistic energy distribution for our device (see figure 8.8) and a Gaussian distribution in deflection angle with a full width half maximum of 1 µrad.
Figure 6.1 shows the resulting probability density for energy loss and deflection per electron $\frac{d^2 P_{\mathrm{coh}}}{dE d\theta_{\mathrm{e}}}$ given in $\frac{1}{\mathrm{µrad} \cdot \mathrm{eV}}$ for a 100 nm thick membrane.
In this treatment, the boundary terms introduce significant surface contributions. This is seen as a high probability density on the so-called light line. The light line is the linear relation between deflection angle and energy that would correspond to

Die approbierte gedruckte Originalversion dieser Diplomarbeit ist an der TU Wien Bibliothek verfügbar
The approved original version of this thesis is available in print at TU Wien Bibliothek.
TU WIEN Bibliothek Your knowledge hub

the dispersion relation of light emitted perpendicular to the beam. The deflection angle θ_e is given by:

$$\theta_e \approx \frac{\hbar Q}{p_0}$$

where $\hbar Q$ is the transverse momentum transfer of the photon and p_0 is the initial momentum of the electron. The light line is defined by:

$$E = \hbar Q c$$

which, assuming Q to be the absolute of the wave vector of the photon, corresponds to the dispersion of a photon in vacuum.

In the thin sample, Cherenkov emission inside the material is confined to guided modes. The number of available modes is determined by the thickness of the material, in figure 6.1, (i.e. for 100 nm) one mode is available for most visible wavelengths, with a second one beginning to branch off from the light line just above 2.5 eV. As also discussed in section 4.1.3, the large extinction coefficient of silicon in the ultraviolet strongly suppresses photon generation in the bulk for energies above 3.5 eV. A simple rule for the minimum material thickness that can support a guided mode of a given wavelength, is defined in analogy to the criterion for standing waves in a Fabry Pérot interferometer: $d_\mathrm{min} = \frac{\lambda}{2 \cdot n}$ [52].

The total probability of coherently emitting a photon in the visible range can be obtained by integrating over the calculated probability density. By integrating over the energy range between 1.5 eV and 3 eV in the entire interval of deflection angles shown in figure 6.1 a total probability of 0.57% per electron is obtained.

Figure 6.1 also shows a comparison between the full simulation done by Andrea Konečná and the heuristic model presented in section 4.3. The heuristic model ignores boundary conditions and doesn't account for broadening in energy and deflection angle due to the initial beam. While giving results on the right order of magnitude in both the range of θ_e and total emission probability and qualitatively showing a similar behavior (i.e. approximately linear decline in probability with higher deflection angle), the heuristic model deviates significantly from the full simulation.

6.2. Aloof Configurations

The term "aloof" interaction refers to a situation in which an electron is scattered inelastically when passing very close to a material. Marks et Al. observed inelastic scattering near a MgO surface under these conditions in 1982 [53].

Designing a setup in which the electron interacts with the sample in an aloof configuration has some obvious advantages when intending to study coincident pairs of electrons and photons:

Die approbierte gedruckte Originalversion dieser Diplomarbeit ist an der TU Wien Bibliothek verfügbar
The approved original version of this thesis is available in print at TU Wien Bibliothek.
TU WIEN Bibliothek Your knowledge hub

Die approbierte gedruckte Originalversion dieser Diplomarbeit ist an der TU Wien Bibliothek verfügbar
The approved original version of this thesis is available in print at TU Wien Bibliothek.

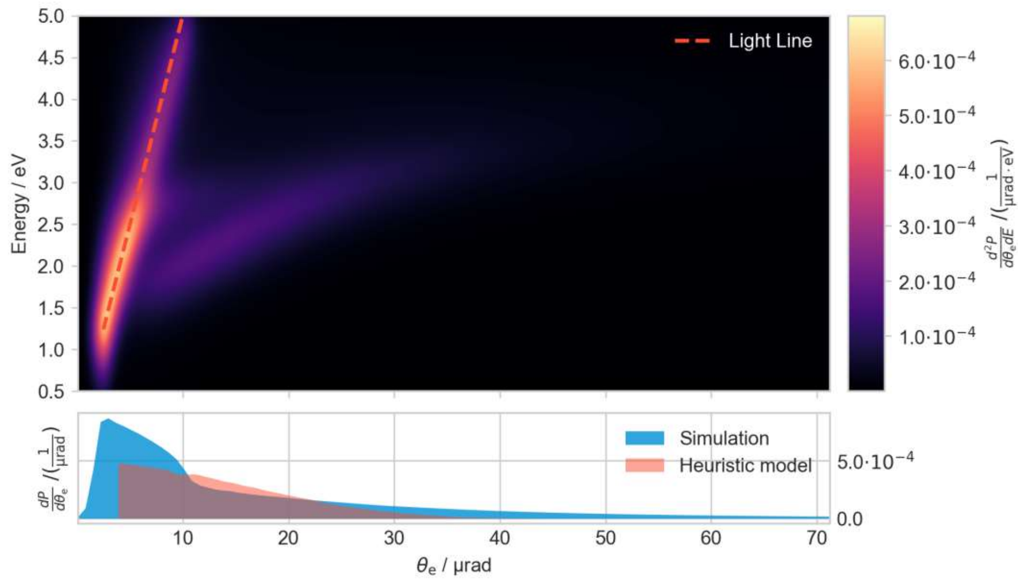

Figure 6.1.: Simulation of probability density for electron energy loss and deflection for a 100 nm thick crystalline silicon membrane. The graph below shows the simulated data from above summed over all possible values for energy for each bin in θ_e, giving a probability density of the observed deflection angle. The simpler model presented in section 4.2 is plotted in red for comparison.

TU WIEN Bibliothek Your knowledge hub

Die approbierte gedruckte Originalversion dieser Diplomarbeit ist an der TU Wien Bibliothek verfügbar
The approved original version of this thesis is available in print at TU Wien Bibliothek.
TU Bibliothek WIEN Your knowledge hub

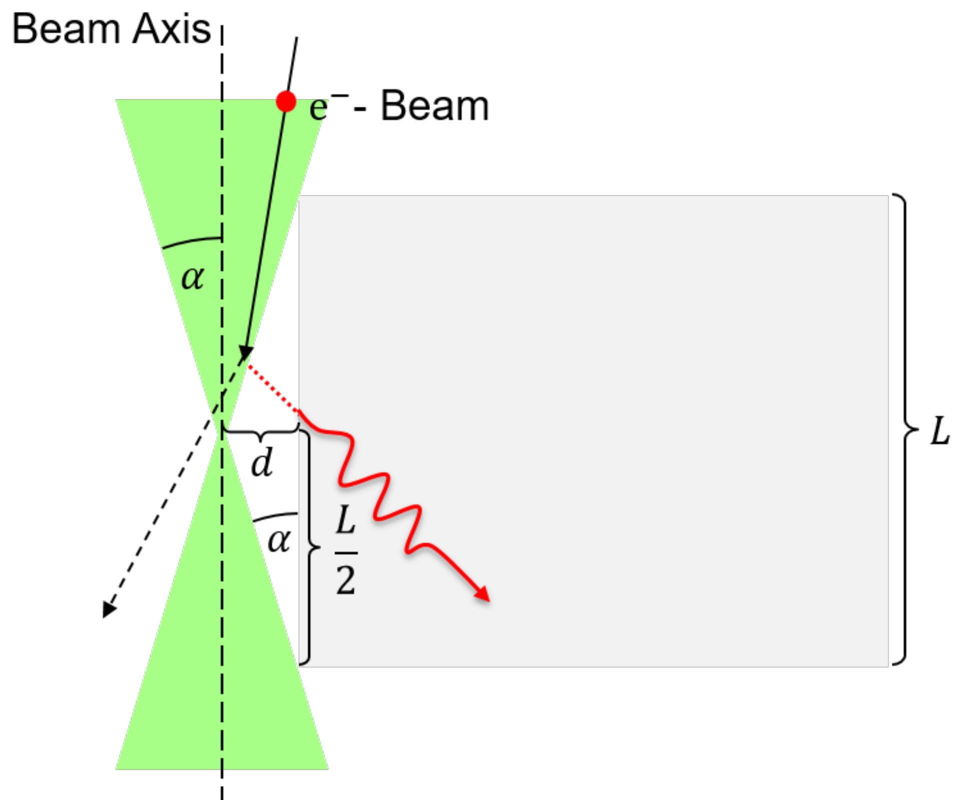

Figure 6.2.: Illustration of Experiment in aloof configuration. A focused electron beam with an opening angle α passes next to a sample at distance d. The larger this distance, the lower the probability to produce a photon. The geometry of the setup determines the maximum interaction length L. The black arrow illustrates on arbitrary classical electron trajectory that would be possible in this configuration.

Firstly only minimal elastic scattering on the electron side is to be expected.
Secondly inelastic scattering on the electron side is greatly reduced. In electron microscopy nearly all relevant interactions are mediated by the electromagnetic field, the probability of an interaction that causes an energy transfer of ΔE_γ decreases as function of $\frac{r}{\lambda_\gamma}$, where r is the distance and $\lambda_\gamma = c \cdot \frac{\hbar}{\Delta E_\gamma}$ is the photon wavelength associated with that energy [35]. This means that inelastic scattering processes linked to a large energy transfer are strongly reduced. By choosing an appropriate distance, contributions corresponding to higher energy are more strongly suppressed. The fraction of total intensity observed, that is due to Cherenkov emission therefore increases.
Thirdly, in contrast to a configuration in which the electron has to penetrate the sample, an aloof setup in principle allows for an arbitrarily long interaction length which may allow for an increase in coherent emission.
Unfortunately the aloof configuration also includes significant disadvantages, not least among which is the considerable experimental overhead that is added by alignment and the management of drift in the microscope as well as charging in the sample: The Beam has to be positioned very precisely, typically within 100 nm of the sample surface and the sample orientation must be aligned very precisely with respect to the beam. Some surface charging is unavoidable, which complicated the tasks mentioned above and can cause distortions in the beam.
Looking at the geometry of the aloof configuration more closely, it becomes obvious, that the interaction probability of the electron can actually not be increased arbitrarily. No matter how the sample is illuminated, the incoming electron always has a certain angular distribution, under focused illumination one can approximate this distribution by stating that electrons arrive within a semi-angle α. Neglecting the effect of diffraction at the condenser aperture, α is given by:

$$\alpha = \arctan(\frac{r_{\mathrm{C2}}}{f})$$

where f is the focal distance between the C2 aperture and the focal plane and r_{C2} refers to the radius of the C2 aperture.
Figure 6.2 shows a focused beam with a semi-angle of alpha passing the surface of a dielectric material at distance d between surface and beam axis. This means that d corresponds to the average distance at which an electron passes the surface. In this sample geometry, the maximum interaction length L, over which the beam can interact with the sample without hitting the sample directly, as a function of the desired value for d is given by:

$$L = \frac{2d}{\tan\alpha} = 2d \cdot \frac{f}{r_{\mathrm{C2}}}$$

For the experiments performed at the FEI Tecnai F20 microscope in the course of this work, assuming a focal length of $f \approx 6.5$ mm is appropriate in the 'nanoprobe

Die approbierte gedruckte Originalversion dieser Diplomarbeit ist an der TU Wien Bibliothek verfügbar
The approved original version of this thesis is available in print at TU Wien Bibliothek.
TU WIEN Bibliothek Your knowledge hub

mode' (the F20's setting for turning its mini condenser lens off), apertures can be selected down to a radius of $r_{C2} > 15$ µm. According to these simple assumptions, the interaction length for $d = 100$ nm is limited to $L \approx 87$ µm.
Another key limitation is the broad momentum distribution of the focused beam. As discussed in section 7 the final distribution of electron momentum is determined by a convolution of the initial distribution with the scattering cross section of the sample $\frac{d^2\sigma}{d\Omega dE}$, even if few other scattering processes play a role i.e. $\frac{d^2\sigma}{d\Omega dE} \approx \frac{d^2\sigma_{\text{coh}}}{d\Omega dE}$, the correlations in momentum can be completely obscured by too much uncertainty in the original electron momentum. The resolution on initial momentum is limited for a probe of a given size, for $d = 100$ nm, the maximum size of the probe is roughly $\Delta x < 100$ nm, consequently:

$$\Delta p_{\perp} > \frac{h}{100 \text{ nm}}$$

Therefore:

$$\Delta\alpha \approx \frac{\Delta p_{\perp}}{p_0} = \frac{h \cdot \frac{1}{100 \text{ nm}}}{h \cdot \frac{1}{\lambda_e}} = \frac{\frac{1}{100} \cdot \frac{1}{\text{nm}}}{\frac{1}{2.5 \text{ pm}}} = 25 \text{ µrad}$$

Which is on the same order of magnitude as the momentum transferred by the emission of a photon. This relation makes it clear that such a configuration is not suitable for studying momentum correlations in electron-photon pairs. Neverthe-less, it can be suitable in other scenarios, for example when studying correlations in energy, as it was done in [5](without time resolution in this case).
This factor can be reduced by simply illuminating a larger area and accepting that not all electrons will pass close enough to the sample to produce a photon, this consequently reduces the emission probability for each individual electron. [1]

One potential way of circumventing these limitations is the use of multi-slit masks, which will be discussed in section 9.3.

[1] An interesting side note to this option is, that one can still post-select those electrons, that emitted a photon. One would expect this subset to electrons to have passed within a small area close to the sample, they are therefore restricted in x but their momentum should be completely defined by the initial momentum, which has a narrow distribution and the momentum of the photon, which can be measured separately, potentially violating the uncertainty relation given above for these post-selected photons.

Die approbierte gedruckte Originalversion dieser Diplomarbeit ist an der TU Wien Bibliothek verfügbar
The approved original version of this thesis is available in print at TU Wien Bibliothek.
TU WIEN Bibliothek Your knowledge hub

7. Momentum Measurement in a Thin Membrane - Limitations and Sources of Error

Having introduced the measurement principles and the main source of coherent cathodoluminescence under consideration, this section will outline some complications which have to be considered when evaluating a potential setup for measuring electron-photon correlations. Firstly the influence of illumination will be discussed, secondly various sample interactions that interfere with our measurement, like elastic scattering and plasmon scattering will be introduced. Finally, the concepts treated thus far will be used to model a coincidence measurement in momentum.

7.1. Initial Momentum Distribution

As already discussed in section 2.2, the electron is emitted from the source and propagates according to some incident wave function ψ_{in}, the sample modifies that wave function in a certain way, e.g. according to Eq. 2.7:

$$\psi_{\mathrm{out}} = \psi_{\mathrm{in}} \cdot e^{-iCV_{\mathrm{p}}(x,y)}$$

In order to investigate the sample, ψ_{in} needs to be well known. As already mentioned in section 2.1 the intensity distribution of a collimated beam limited by a circular aperture in the far field is given by:

$$I = I_0 \frac{(2J_1(x))^2}{x^2}$$

with

$$x = \frac{2\pi R}{\lambda_{\mathrm{e}}} \sin(\theta)$$

where $J_i(x)$ is a Bessel function of the first kind, λ_e is the de Broglie wavelength of the electron and R is the radius of the aperture. This distribution is shown in figure 7.1, it includes side peaks which are significantly smaller than the central

Die approbierte gedruckte Originalversion dieser Diplomarbeit ist an der TU Wien Bibliothek verfügbar
The approved original version of this thesis is available in print at TU Wien Bibliothek.
TU WIEN Bibliothek Your knowledge hub

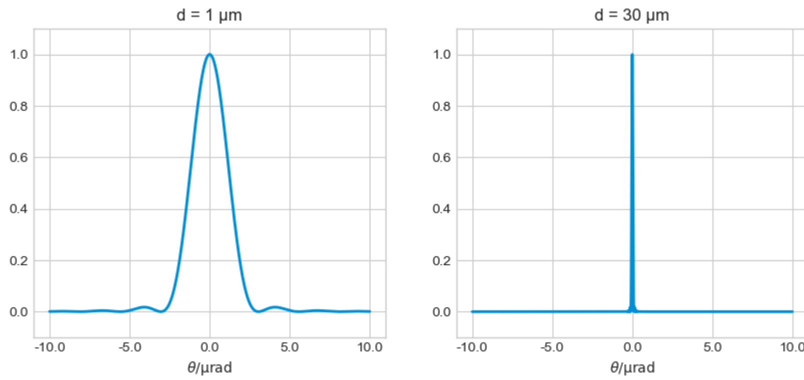

Figure 7.1.: For small apertures (left), the characteristic side lobes of the Airy function are visible, at realistic aperture sizes (right) the distribution is narrow compared to the expected photon recoil.

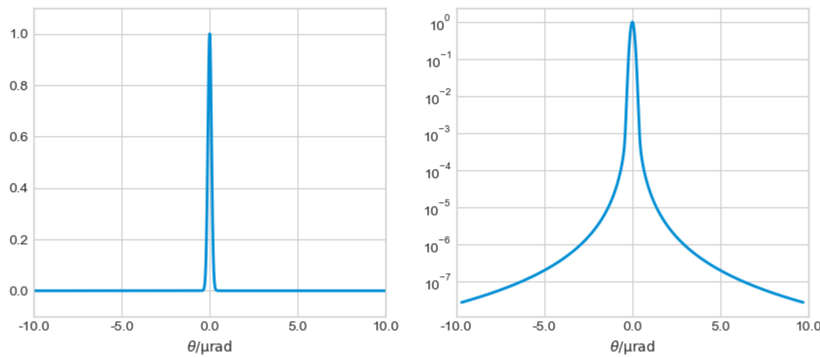

Figure 7.2.: Broadened distribution for sigma= 0.1 µrad in a linear scale (left) and logarithmic scale (right) normalized to $\rho'(0) = 1$

peak but decay comparatively slowly and therefore contribute to the intensity at higher deflection angles.

Aberrations contribute to further broadening, we will model these effects as Gaussian. The resulting final distribution is a convolution of the initial distribution $\rho(\theta)$ with the broadening function f :

$$\rho'(\theta) = (\rho * f)(\theta)$$

Figure 7.2 shows the resulting angular distribution of the beam.

Die approbierte gedruckte Originalversion dieser Diplomarbeit ist an der TU Wien Bibliothek verfügbar
The approved original version of this thesis is available in print at TU Wien Bibliothek.
TU WIEN Bibliothek Your knowledge hub

7.2. Elastic Scattering

As stated above, the final angular distribution is a convolution of the incoming distribution with a scattering function. To be more precise, elastic scattering and scattering due to the Cherenkov effect are independent processes, the total scattering function is a convolution of two individual functions representing these two processes.
As it is our goal to measure electron-photon correlations in momentum, we are interested in studying only scattering due to coherent photon emission, strong elastic scattering can obscure this effect and is therefore not desirable.
In both amorphous and poly-crystalline materials, elastic scattering is very broad compared to the deflection of electrons due to the Cherenkov effect. For all experiments that involve the electron transitioning through the sample, our results so far suggest that it will therefore be necessary to use single-crystalline samples.
Given the use of a single crystalline sample, the material can be modeled as a lattice of atoms with an effective atomic potential at each lattice site (see section 2.2). If that atomic potential was a delta function, only discrete deflection angles corresponding to the reciprocal lattice vectors would be possible, each diffraction spot would simply be a reproduction of the incoming beam, it would be possible to see additional deflection due to the Cherenkov effect and other inelastic processes around each diffraction spot, as well as around the fundamental peak (illustrated in figure 7.3).
In realistic samples however deviations from the ideal lattice introduce additional broadening. This includes thermal movement of the lattice atoms, referred to as thermal diffuse scattering (described by the Debeye-Waller factor [13, Chapter 5.9]) as well as due to large scale variations in the sample, i.e. inhomogeneities in the surface or the thickness of the sample. All of these effects are exacerbated by multiple scattering, which is unavoidable even in very thin samples.
In order to model the effect of elastic deflection, an elastic mean free path of 130 nm (see section 2.2.1) will be assumed, therefore about $1/e \approx 37\%$ of the initial electron current is still present in the fundamental peak for a 100 nm thick sample. The fundamental peak is equal to the incident beam with some additional broadening due to the effects mentioned above, a diffuse component to scattering with a probability of p_{TDS} adds background intensity.

7.3. Inelastic Scattering

In addition to the broadening caused by elastic scattering, inelastic effects like the emission of plasmons, Bremsstrahlung or the coupling to internal states of the sample also cause electron deflection.

Die approbierte gedruckte Originalversion dieser Diplomarbeit ist an der TU Wien Bibliothek verfügbar
The approved original version of this thesis is available in print at TU Wien Bibliothek.
TU WIEN Bibliothek Your knowledge hub

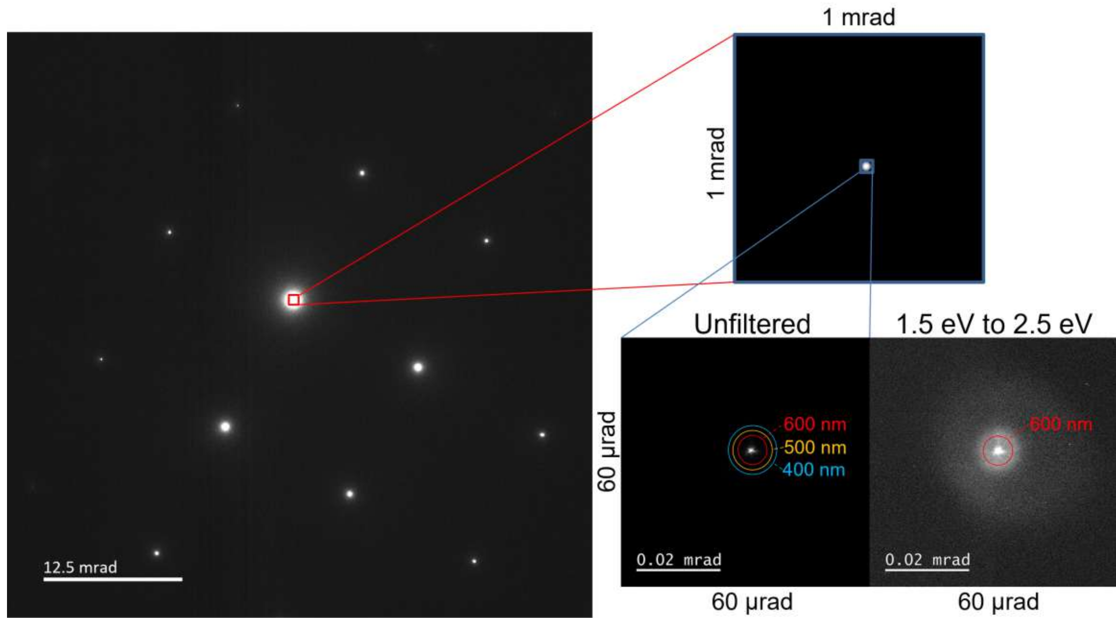

Figure 7.3.: Illustration of deflection angles corresponding to Bragg diffraction and photon emission. The crystal lattice of a silicon sample produces a diffraction pattern on the order of mrad. By increasing the camera length smaller deflection angles can be resolved. An energy filtered low angle diffraction measurement, set to record electrons that have lost 1.5 eV to 2.5 eV of energy reveals deflection on the µrad scale that is consistent with the momentum transfer from a single photon with an energy of 2 eV in vacuum.

Die approbierte gedruckte Originalversion dieser Diplomarbeit ist an der TU Wien Bibliothek verfügbar
The approved original version of this thesis is available in print at TU Wien Bibliothek.
TU WIEN Bibliothek Your knowledge hub

As already stated in section 2.2, the inelastic effects have a combined mean free path of approximately 145 nm making it likely for each electron transitioning through a 100 nm sample to undergo some kind of inelastic interaction.
These interactions are typically isotropic, i.e. their associated momentum transfer has a typical magnitude but no preferred direction. In the comparatively small range of deflection angles associated with the emission of a visible photon, they can be modeled as a constant background : each electron undergoes an inelastic process with a probability $p_{\text{inelastic}}$ and is deflected into any angle within the considered interval.
By using the microscope's energy loss filter, one can exclude those electrons that have lost a large amount of energy in an inelastic process. Bulk plasmon excitation in silicon as the most common of these processes is associated with an energy loss of 16.6 eV [54] and therefore clearly distinguishable from photon emission. It also allows for the exclusion of electrons that have undergone a photon emission in addition to some other inelastic process if the sum of both of these energy losses exceeds the range set by the filter. This option is particularly important, as these excitations can potentially be radiative: a plasmon may decay into visible photons within a very short lifetime, the associated electron may then be detected in coincidence with the photon.

7.4. Example: SNR of a Coincidence Measurement

In the most promising experimental configuration that has been investigated in this work, a thin ($\approx$ 100 nm) silicon membrane is illuminated by a collimated electron beam (see section 8.3). The sample is observed either in imaging or in diffraction mode and the photons are collected using the Vulcan system. The electron energy loss filter is tuned to exclude electrons that have lost a large amount of energy ($\Delta E > 8$ eV) e.g. due to bulk plasmon excitation.
Using the Timepix3 as a direct electron detector, it is possible to detect up to $5 \cdot 10^7$ events per second. As each electron typically triggers multiple detection events, this corresponds to a current of 10^7 e^-/s on the sensor. This figure limits the maximum number of electrons per second that can be detected in a coincidence experiment. Depending on the respective setup, this may also be the limiting factor on the maximum current that can be used in the experiment. The time resolution of the detector is limited by its jitter. Various groups have reported achieving time resolutions below 5 ns measured as the full width at half maximum of the arrival time distribution compared to a true arrival time given e.g. by a laser triggered electron source [8][55]. However these results involved potentially

Die approbierte gedruckte Originalversion dieser Diplomarbeit ist an der TU Wien Bibliothek verfügbar
The approved original version of this thesis is available in print at TU Wien Bibliothek.
TU WIEN Bibliothek Your knowledge hub

technically challenging calibration methods such as time-walk correction [56] and the use of machine learning [55]. There are various different implementations of an electron camera using the Timepix3 ASIC. The model used in the QOEPP project is the ePix camera by the company Advascope. At the time of writing it is not clear which time resolution will be attainable with this implementation and which additional calibrations will be necessary. In order to make a conservative estimate, we assume that we will be able to achieve at least the same time resolution as Schröder et al. get without any correction in [55], despite using a model from a different manufacturer. This means that we hope to achieve a time resolution of 10 ns FWHM.

Figure 7.4 shows the number of true and false coincidences calculated as described in section 5.3. For this calculation it is assumed that electrons are detected with a probability of $\alpha_e = 10\%$ due to elastic scattering into other Bragg peaks and inelastic scattering corresponding to a large energy loss, these processes are assumed to happen independently from coherent photon emission. Therefore, if the maximum permissible current at the detector is 10^7 e$^-$/s, the initial current used can be $\frac{1}{\alpha_e} = 10$ times higher, i.e. 10^8 e$^-$/s. Additionally the calculations for figure 7.4 assume no dark counts for the electron detector ($R_{\mathrm{eDC}} = 0$) which is appropriate for the Timepix3 sensor. The photon detector is assumed to have a dark count rate $R_{\gamma\mathrm{DC}}$ of 300 counts/s. According to our measurements in thin silicon samples, the joint probability per electron of producing and detecting a photon is (see 8.3):

$$\alpha_\gamma \cdot p_{\mathrm{coh}} = 10^{-5}$$

The probability that is contributed by incoherent processes is unknown, but we will assume it to be approximately 1/10 of the total signal:

$$\alpha_\gamma \cdot p_{\mathrm{in}} = 10^{-6}$$

This is suggested by results presented in [57]: A measurement of CL in a thick (700 nm) silicon sample decreases by a factor of approximately 25 in intensity over a spectral range between 400 nm and 900 nm as the accelerating voltage is decreased by a factor of 5 from 200 keV to 40 keV. The intensity of Cherenkov radiation depends on the energy of the exciting electron as discussed in 4, the intensity of incoherent contributions should typically only be proportional to the deposited energy. Additionally, the difference in *deposited* energy between the 200 keV and the 40 keV setting is certainly smaller than a factor of 5, because the stopping power for silicon is ≈ 0.5 keV/µm at 200 keV and ≈ 1.4 keV/µm [58]. We also assume the photon detection efficiency α_γ to be equal for both coherent and incoherent processes (as it was also done in [59]).

TU Bibliothek WIEN Your knowledge hub
Die approbierte gedruckte Originalversion dieser Diplomarbeit ist an der TU Wien Bibliothek verfügbar
The approved original version of this thesis is available in print at TU Wien Bibliothek.

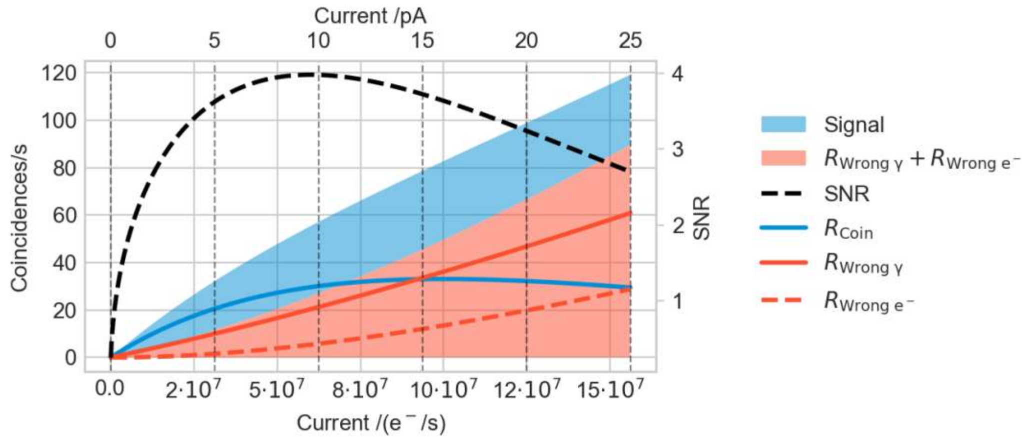

(a) Linear plot (Note that it starts at 10^{-3} pA)

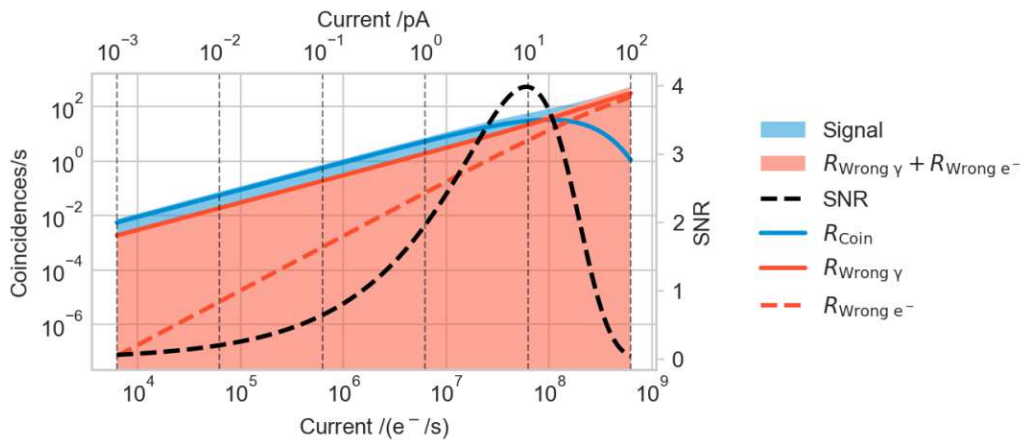

(b) Logarithmic plot

Figure 7.4.: Coincidence rates and signal to noise ratio as a function of current including the zero loss peak. Colored lines show individual contributions to the rate of true and false coincidence events according to the equations presented in section 5.3. The colored area in the background shows the fractions these contribution correspond to in the total signal. SNR was calculated assuming measurement time $T = 1$ s.

Die approbierte gedruckte Originalversion dieser Diplomarbeit ist an der TU Wien Bibliothek verfügbar
The approved original version of this thesis is available in print at TU Wien Bibliothek.
TU WIEN Bibliothek Your knowledge hub

Figure 7.4 shows that an experiment under these conditions should not be run at the maximum available current as the signal to noise ratio drops off rapidly with higher currents. This is mainly due to the limited temporal resolution of the detector. However, at lower currents the expected signal is twice to three times above the noise level, making for a clearly discernible result. Additionally, the SNR in figure 7.4 was calculated for measurement time $T = 1$ s and scales with $\sqrt{T}$, as stated by Eq. 5.14.
The situation can be further improved by changing the settings of the energy filter: so far we considered only filtering out energy ranges far above the energy corresponding to the visible spectrum, however all electrons below this threshold were equally likely to be detected. By also restricting the lower bound of the energy of the transmitted photons, we can exclude electrons that did not loose any energy, effectively filtering out the zero loss peak, which contains a large fraction of all transmitted electrons and does only contribute to the noise in the measurement.
The full width half maximum of the energy distribution of the initial beam is $\approx$ 0.7 eV for the Tecnai F20 used in this work. In the energy spectrum the electrons that have emitted a photon don't form a clearly distinct spectral feature, applying the filter can be regarded as introducing distinct detection probabilities for ZLP electrons and electrons that have emitted a photon: Electrons that have emitted a photon remain nearly unaffected and are still detected with $\alpha_{e\gamma} \approx \alpha_e$, photons from the zero loss peak are not detected with $\alpha'_e < \alpha_e$.
In the measurements presented in section 8.3, $\approx$ 90% of all counts present in the recorded EFTEM images fall into the energy range -0.5 eV to 0.5 eV, therefore, it seems safe to calculate with $\alpha_{e\gamma} = \alpha_e = 10\%$ and $\alpha'_e < \frac{\alpha_e}{10} = 1\%$. Figure 7.5 illustrates the result of the corresponding calculations: These modified settings should allow for a higher current to be used and therefore for a higher true coincidence rate to be achieved, simultaneously the signal to noise ratio is significantly improved.

Die approbierte gedruckte Originalversion dieser Diplomarbeit ist an der TU Wien Bibliothek verfügbar
The approved original version of this thesis is available in print at TU Wien Bibliothek.
TU WIEN Bibliothek Your knowledge hub

Die approbierte gedruckte Originalversion dieser Diplomarbeit ist an der TU Wien Bibliothek verfügbar
The approved original version of this thesis is available in print at TU Wien Bibliothek.
TU Bibliothek Your knowledge hub WIEN

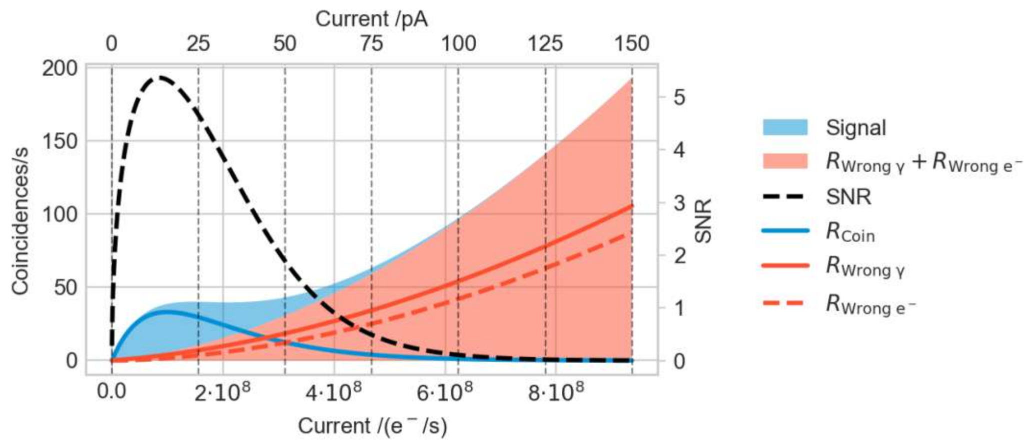

(a) Linear plot (Note that it starts at 10^{-3} pA)

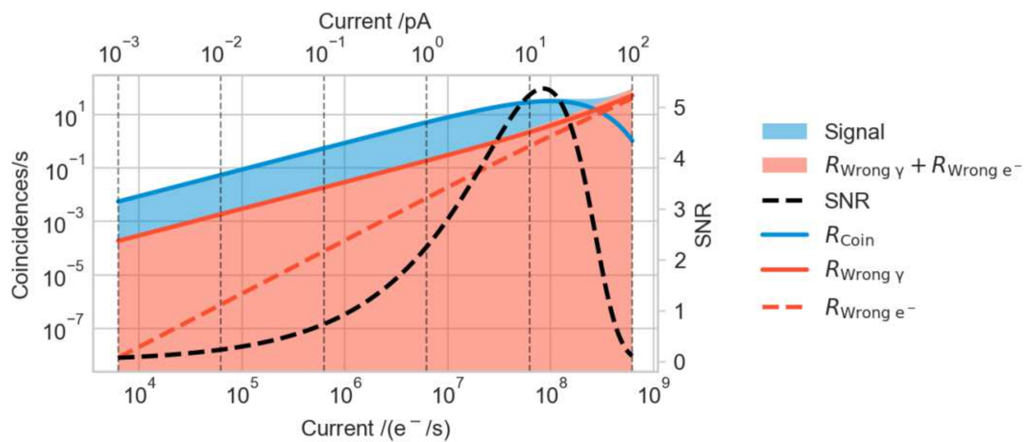

(b) Logarithmic plot

Figure 7.5.: Coincidence rates and signal to noise ratio as a function of current with filtered zero loss peak. Due to the effect of the electron filter, a lower electron detection efficiency $\alpha'_e < \frac{\alpha_e}{10}$ is assumed for electrons that did not emit a photon. Colored lines show individual contributions to the rate of true and false coincidence events according to the equations presented in section 5.3. The colored areas in the background show the fractions these contributions correspond to in the total signal. SNR was calculated assuming measurement time $T = 1$ s.

8. Thin Specimen

In this configuration, a thin piece of material is illuminated with a broad, well collimated electron beam. Figure 8.1 illustrates the setup: the collimated beam hits the sample, some electrons emit photons and are deflected by some angle θ_e. In diffraction mode (Figure 8.1 a), the deflection angles of the individual electrons are resolved. The angular distribution of the initial beam is much narrower than the momentum transfer that corresponds to the emission of a single photon, therefore undeflected electrons are imaged to a small spot on the center of the screen. As discussed in section 7, the signal for coincident detections is also going to be a convolution of the interaction cross section with the initial distribution of the beam. Figure 8.1 b shows the situation, when the microscope is set to imaging mode: electrons are imaged according to the position where they transition through the material, independent of their momentum.
Measurements in this configuration were done for 100 nm silicon nitride (Si_3N_4) layers (refractive index $n \approx 2.2$ [60]), mica layers of various thicknesses between 80 nm and 200 nm (refractive index $n \approx 1.6$) and silicon layers of various thicknesses (refractive index $n \approx 3.5$). Silicon turned out to be the most suitable for this type of experiment and section 8.3 will be dedicated exclusively to the results of these measurements. The measurements on Si_3N_4 and mica which are presented in the rest of this section will serve to explain the experiment in more detail and highlight some important requirements in sample material selection.

8.1. Thin Silicon Nitride

Silicon nitride is extremely easy to obtain and handle: silicon nitride membranes are inert, very stable and can be made with an extremely well defined geometry using well established techniques from MEMS fabrication. They are commonly used as support films for samples in electron microscopy, therefore ready made membranes mounted on 3 mm TEM grids are commercially sold in various thicknesses. We used a 100 nm thick film sold by the company Micro to Nano [61].
Unfortunately these convenient aspects of the silicon nitride sample were outweighed by two significant downsides: firstly they produced very low photon counts, secondly the amorphous structure of the material led to broad elastic scattering, which is not desirable when trying to resolve momentum, as already

Die approbierte gedruckte Originalversion dieser Diplomarbeit ist an der TU Wien Bibliothek verfügbar
The approved original version of this thesis is available in print at TU Wien Bibliothek.
TU Bibliothek WIEN Your knowledge hub

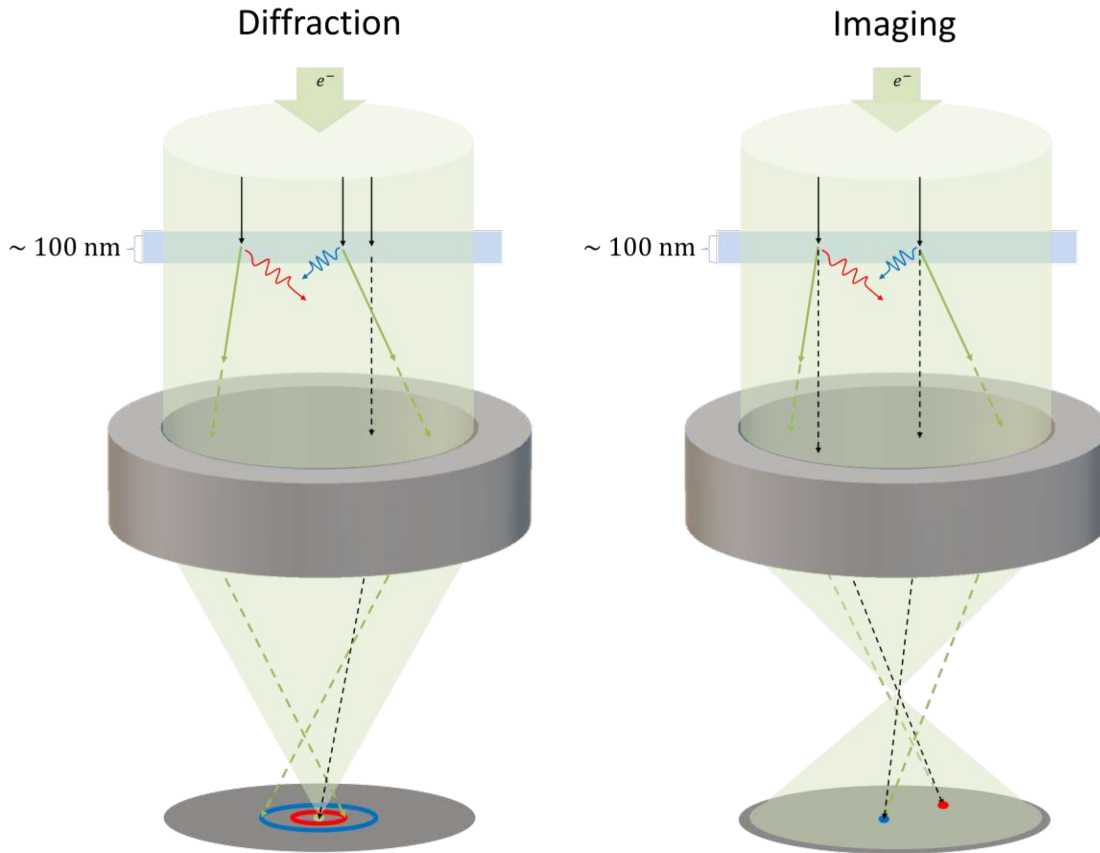

Figure 8.1.: Schematic of measurements in imaging and diffraction mode: Electrons pass through a thin membrane of dielectric material and emit photons. The electron wave function is represented in green, arrows are depictions of possible classical electron trajectories. Depending on the setting of its lenses, the microscope resolves the electron's transverse momentum (diffraction mode) or position in the sample plane (imaging mode).

Die approbierte gedruckte Originalversion dieser Diplomarbeit ist an der TU Wien Bibliothek verfügbar
The approved original version of this thesis is available in print at TU Wien Bibliothek.
TU WIEN Bibliothek Your knowledge hub

Die approbierte gedruckte Originalversion dieser Diplomarbeit ist an der TU Wien Bibliothek verfügbar
The approved original version of this thesis is available in print at TU Wien Bibliothek.

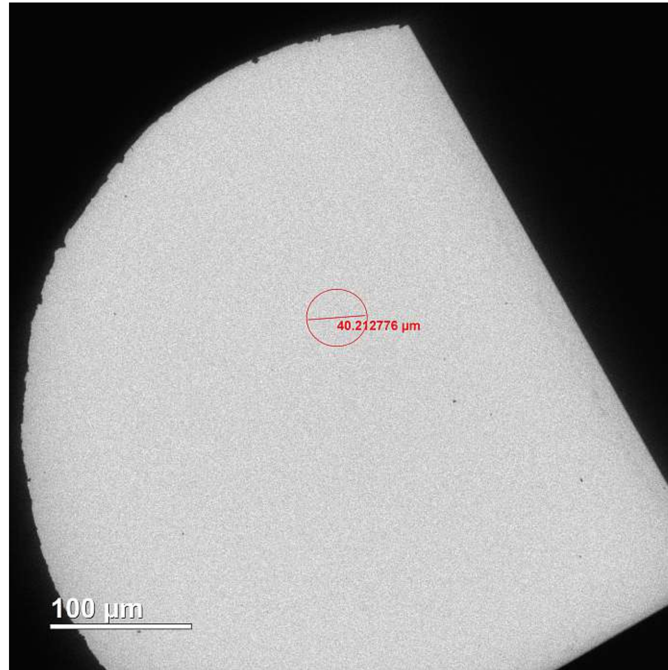

Figure 8.2.: Low magnification TEM image of a Si_3N_4 membrane, the red circle indicates the area that was illuminated during the photon measurements.

explained in section 7. We measured the amount of cathodoluminescence produced using the Gatan Vulcan holder and connecting its bottom port to the input of the Excelitas SPCM-AQRH-13-FC Single photon counting module using a multimode fiber cable (Thorlabs M76L02, NA = 0.39). We illuminated the sample with a current of 150 pA and moved the illuminated area on the sample in order to achieve maximum photon count rate. As the silicon nitride membrane looks very uniform in the TEM image, we assumed that the point of highest count rate corresponds to the focal point of the holders bottom mirror, the corresponding illuminated area is annotated in figure 8.2. At these settings 2200 counts/second were detected on average. A dark count rate of 250 counts/second was measured by closing the column valves of the electron microscope, thereby blocking the electron beam and all light from the gun from entering the column.
This results in a corrected count rate of 1950 counts/second which corresponds to 13 counts/(second · pA) or to a detection probability of approximately $2.1 \cdot 10^{-6}$ per electron.

According to Eq. 2.6, the elastic cross section for most materials is very large compared to the cross section due to photon emission. Elastic scattering in crystalline samples is clearly defined by the periodicity of the lattice. The resulting

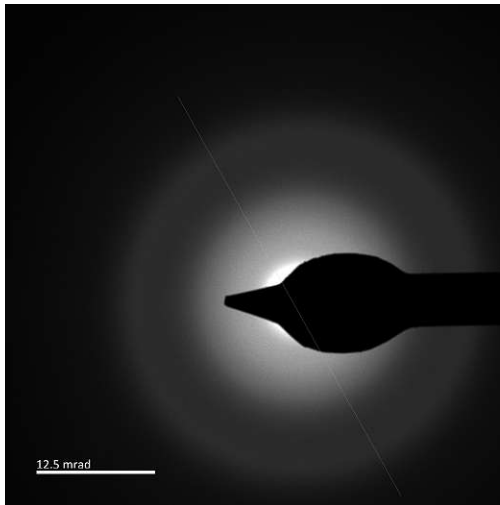

(a) Silicon Nitride (amorphous, 100 nm thickness)

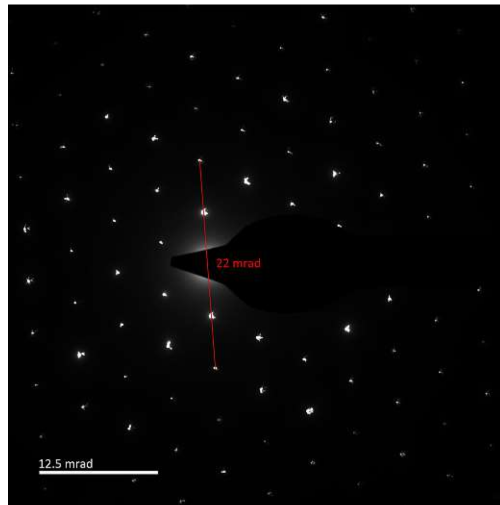

(b) Mica (crystalline, 80 nm thickness

Figure 8.3.: Comparison between diffraction pattern of a crystalline and an amorphous sample. While diffraction peaks are clearly defined for the single crystal, a washed out distribution is observed for elastic scattering in the amorphous material.

Bragg spots are separated by angles on the order of milliradians and are therefore easily distinguishable from the deflection caused by the emission of a photon. In amorphous samples, elastic scattering is broadly distributed and can therefore obscure the effect of photon emission. Figure 8.3 shows a comparison between the diffraction patterns of a silicon nitride membrane and crystalline mica membrane. While the crystalline sample shows sharp peaks, separated by an angle of $2.2\ \frac{1}{\mathrm{nm}} \approx 5.5$ mrad, the amorphous sample shows a broad intensity distribution. After these experiments we came to the conclusion, that it would be beneficial to use a crystalline material, therefore the next step was to use thin mica membranes.

8.2. Thin Mica

Like silicon nitride, mica is comparatively simple to handle: it's commonly used as a substrate for other samples because it can easily be split into very thin individual layers with respect to a preferred crystallographic direction. The sample depicted in figure 8.3b and figure 8.4 was produced by gluing a thin plate of mica, which is commercially available as a microscopy supply, to two microscopy slides, one on each side. Ripping off one of the two slides typically results in the delamination of a mica layer, this layer can consequently be placed on a TEM grid after removing

Die approbierte gedruckte Originalversion dieser Diplomarbeit ist an der TU Wien Bibliothek verfügbar
The approved original version of this thesis is available in print at TU Wien Bibliothek.
TU WIEN Bibliothek Your knowledge hub

the glue using a solvent (in this case acetone). As indicated in figure 8.4, the resulting layer in this case was only 80 nm thick (measured using the log-ratio method in EELS). CL measurements on a 110 nm mica film resulted in a photon detection probability of approximately 20 counts/(second $\cdot$ pA). This value was obtained by illuminating a point of known thickness (110 nm as determined by the log-ratio method in EELS) with a current of 600 pA (as determined by the current measurement device integrated in the Tecnai F20's viewing screen) and detecting a total count rate of approximately 20000 counts per second. Care was taken to make sure that the focal point of the Vulcan system overlapped with the investigated region. This corresponds to a detection probability of approximately $5.3 \cdot 10^{-6}$ per electron.
Using these mica sample we tried to resolve the electron deflection due to coherent photon emission. The microscope was set to diffraction mode and the energy filter was adjusted in order to select energy losses corresponding to the emission of visible photons. The camera length was increased in order to resolve angles on the scale of microradians (see section 3.1). Unfortunately, we were unable to detect any discernible signal that could be attributed to this effect over multiple iterations with different samples. One possible explanation for these observations is the comparatively low refractive index of mica. Following the assumptions presented in section 4.3, one would assume that a refractive index of approximately 1.6 ([62]) is sufficient to produce a detectable number of photons for 200 keV electrons. Taking into account the effect of the sample geometry this may no longer be the case: using a thin mica membrane reduces the effective refractive index that the electron interacts with. A theoretical investigation of a thin membrane with a dielectric function suitable for mica, such as the one for silicon done by Dr. Konečná (see section 6.1), would allow us to get a more educated estimate of the signal that is actually expected. As measurements on thin pieces of silicon showed more promising results, a further investigation of the mica membranes was not deemed to be a priority and consequently remains outside the scope of this work. In addition to this potential impediment, two technical problems complicated the experiment with mica membranes: firstly, strong charging was observed on multiple occasions, this is unsurprising as mica is a very good insulator. Secondly, the sample preparation was not very repeatable and control of the sample geometry was limited. This did not only exacerbate the charging issues but also frequently led to distortions in the beam due to elastic scattering.

Die approbierte gedruckte Originalversion dieser Diplomarbeit ist an der TU Wien Bibliothek verfügbar
The approved original version of this thesis is available in print at TU Wien Bibliothek.
TU WIEN Bibliothek Your knowledge hub

Die approbierte gedruckte Originalversion dieser Diplomarbeit ist an der TU Wien Bibliothek verfügbar
The approved original version of this thesis is available in print at TU Wien Bibliothek.
TU WIEN Bibliothek Your knowledge hub

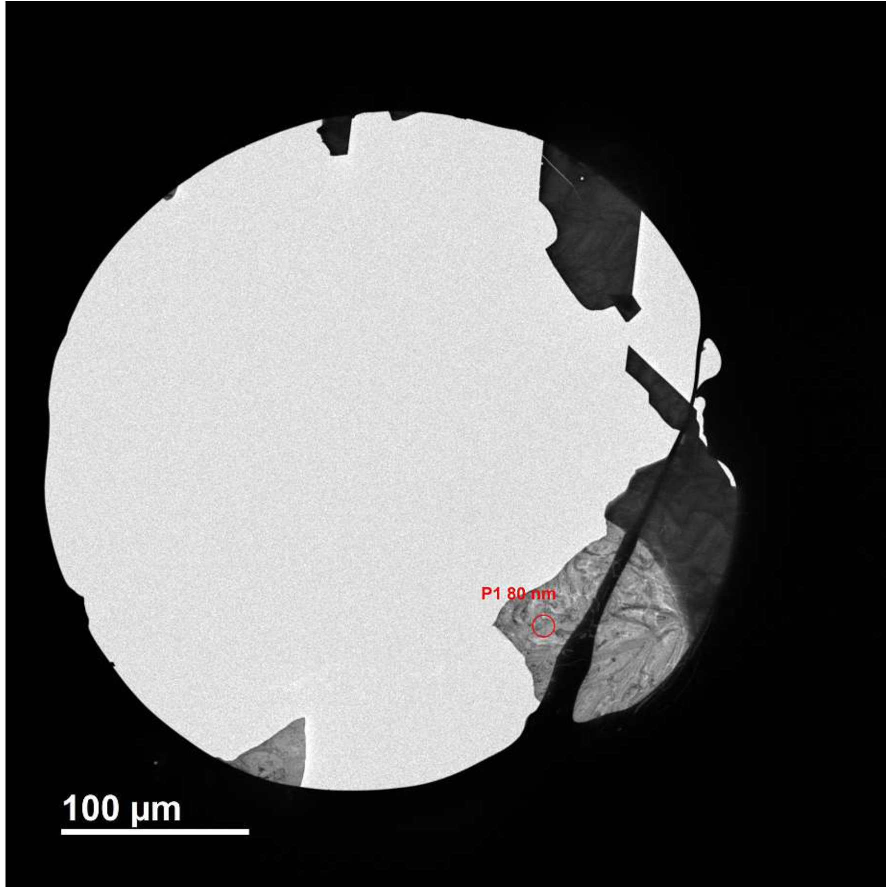

Figure 8.4.: Overview image of one mica sample. The thickness in position P1 was measured using EELS, resulting in a value of approximately 80 nm. The thin membrane seen in gray around P1 covers only a small fraction of the observed area, this is probably due to damage during sample preparation.

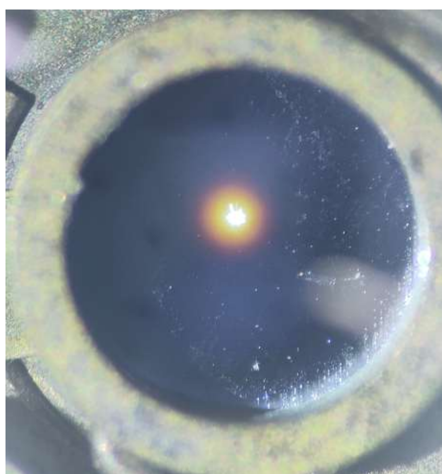

Figure 8.5.: Photograph of thin silicon sample prepared by grinding and ion polishing. The same sample is also shown in figure 8.6.

8.3. Thin Crystalline Silicon

A thin silicon sample was prepared from a standard silicon wafer by mechanical grinding and polishing down to a thickness of a few nanometers. It was then placed on a standard copper TEM grid. The silicon was further thinned using the Gatan precision ion polishing system (PIPS II, Argon bombardment at 4.5 keV) until it was completely perforated in one spot, figure 8.5 shows an image of the resulting sample.

The sample was again illuminated broadly and viewed in diffraction mode with a camera length of 31 m before the energy filter, which corresponds to an effective camera length of 558 m, when taking the magnification of the Gatan image filter (i.e. 18 x) into account. In this setting, each pixel on the spectrometer camera corresponds to 0.025 µrad. The energy filter was set to transmit energy intervals of 1 eV, images were taken at central energies between -1 eV and + 6 eV of energy loss (i.e. at a central energy of 0 eV, electrons between -0.5 eV and 0.5 eV are imaged onto the sensor.).

The left column of figure 8.7 shows the resulting images. The bright spot in the center of each image stem from electrons in the Zero loss peak that are transmitted through the filter due to the width of the initial beam's energy distribution. As this artifact is typically the brightest feature in each image, the intensity of the color map has been clipped to an intensity value below the measured maximum.

The images clearly show a circular intensity distribution around the central peak. While the 0.5 eV to 1.5 eV interval only shows a slight broadening around the central beam a distinct ring becomes visible at 2.5 eV to 3.5 eV. The radius of these

Die approbierte gedruckte Originalversion dieser Diplomarbeit ist an der TU Wien Bibliothek verfügbar
The approved original version of this thesis is available in print at TU Wien Bibliothek.
TU WIEN Bibliothek Your knowledge hub

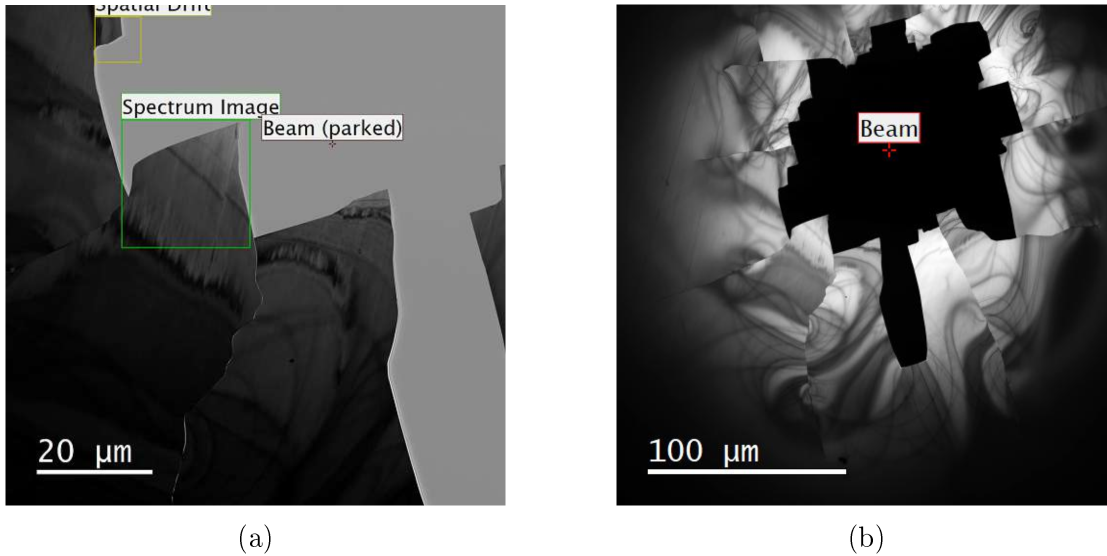

(a) (b)

Figure 8.6.: STEM Images of the silicon sample.

rings corresponds to the deflection angle of the electrons and should consequently reflect the magnitude of the photon recoil. As one would expect, it increases with the selected electron energy loss.
The graphs shown in the right column of figure 8.7 illustrate the radial intensity distribution of the image. They were obtained by integrating the image intensity in an annular area, corresponding to an interval in radius $\Delta r = 0.5$ µm. In order to do this, the intensity data was linearly interpolated.
Figure 8.7 also includes simulations presented in section 6.1, these simulations represent probabilities per electron, in order to make them comparable to the data, the intensity in each pixel has been normalized using the sum over all intensity in all images. This is preferable to normalizing the intensity using the total number of electrons in the incident beam, because both elastic scattering and plasmon excitation are assumed to be independent from photon emission:
By selecting a small collection angle, elastically scattered electrons are excluded both from the measured intensities and from the normalizing factor. Equivalently, plasmon excitation is excluded by using the energy filter, therefore electrons that have excited plasmons contribute neither to the measured intensity nor to the normalization factor.
Figure 8.8 shows the energy distribution of the incident electron beam. In typical operating condition it has a full width half maximum of around 1 eV; this can be reduced by lowering the extractor voltage. Due to this comparatively broad distribution, some electrons that start out with a lower initial energy are going to be transmitted through the filter. Figure 8.8a shows the expected number of

Die approbierte gedruckte Originalversion dieser Diplomarbeit ist an der TU Wien Bibliothek verfügbar
The approved original version of this thesis is available in print at TU Wien Bibliothek.
TU WIEN Bibliothek Your knowledge hub

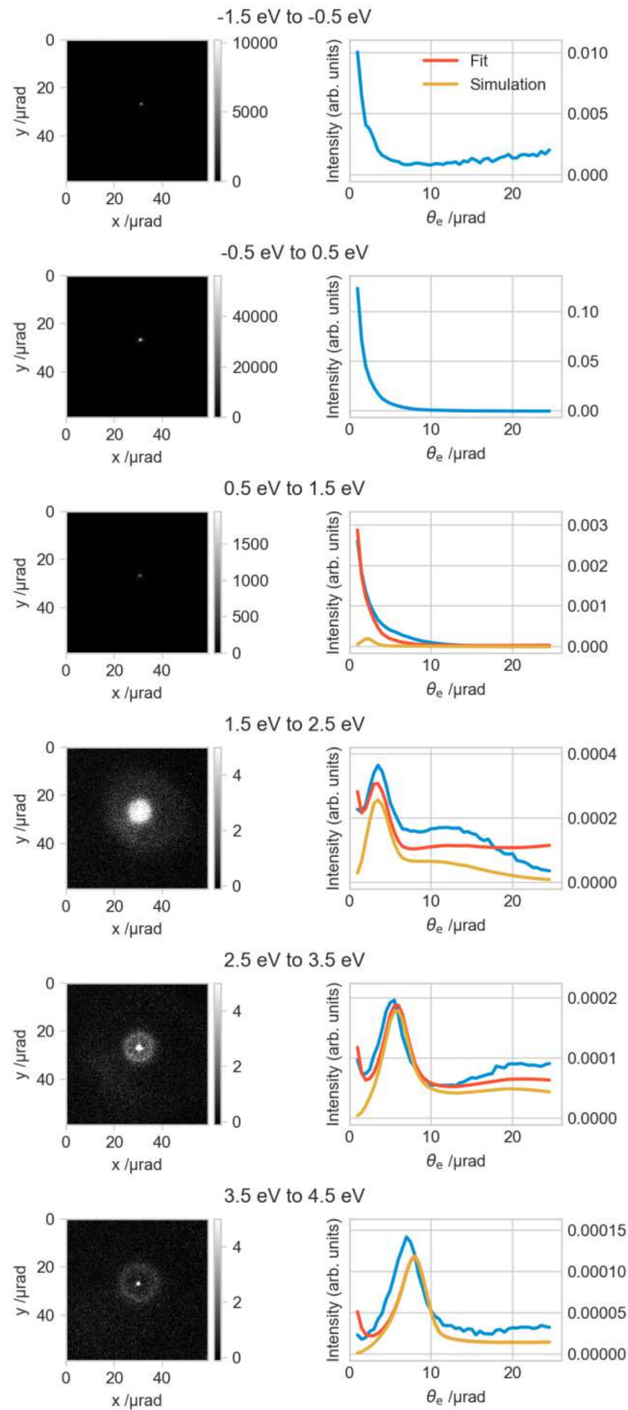

Figure 8.7.: Energy filtered low angle diffraction images of a 100 nm silicon membrane (left) and radial distributions with respect to the central maximum (right). The right plots include the simulations presented in section 6.1. The fit accounts for the contribution of the central beam (modeled by the distribution at 0 eV energy loss) and a constant background.

Die approbierte gedruckte Originalversion dieser Diplomarbeit ist an der TU Wien Bibliothek verfügbar
The approved original version of this thesis is available in print at TU Wien Bibliothek.
TU WIEN Bibliothek Your knowledge hub

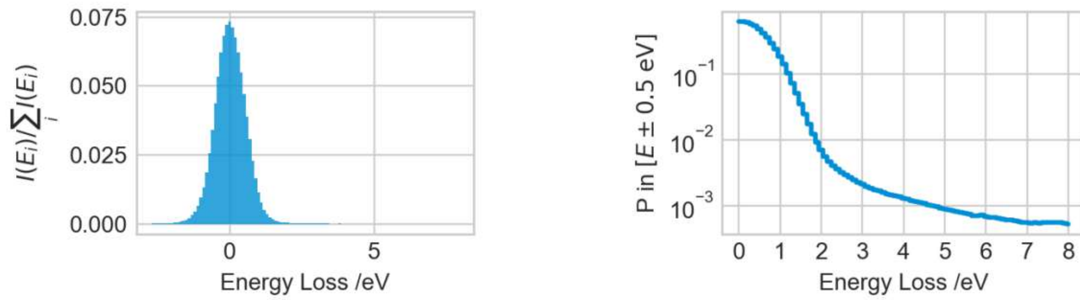

(a) Energy distribution of the electron beam.

(b) Energy distribution of the electron beam: probability of finding the electron in a ± 0.5 eV interval around the respective energy loss value.

Figure 8.8.: Energy distribution of the electron source without sample interaction.

electrons to be transmitted in a 1 eV energy interval centered around a given value. This means that a large contribution from the zero loss peak is to be expected and that it makes sense to correct our estimates in order to account for this source of background.
Elastic scattering, in particular thermal diffuse elastic scattering, may contribute a background to the signal, as already mentioned in section 7. It therefore makes sense to also consider a constant background on the image. Figure 8.7 therefore includes a fit accounting for these factors, the effective intensity $I(r)$ is given by:

$$I(r) = I_{\text{sim}}(\theta_{\text{e}}) + A \cdot I_{\text{ZLP}}(\theta_{\text{e}}) + B \cdot 2\pi\theta_{\text{e}}$$

The background function I_{ZLP} can either be modeled as described in section 7.1 or by assuming that the shape of the central beam at 0 eV energy loss can be used to approximate the background at any energy. In figure 8.7 the contribution from the zero loss beam has been fitted using the distribution at 0 eV energy loss, in figure 8.9 a Gaussian distribution with a standard deviation of $\sigma = 1$ mrad has been used.
In general the model represents many of the key features of the data very well; from 2 eV onward the maximum of the distribution, which corresponds to the light line, agrees well with the prediction for the recoil of a photon of the corresponding energy in vacuum. The simulation actually predicts two concentric rings in the intensity, one corresponding to the light line while the other corresponds to a guided mode in the silicon membrane. This second ring can be seen very faintly in the 1.5 eV to 2.5 eV interval and in the 2.5 eV to 3.5 eV interval and is clearly

TU WIEN Bibliothek Your knowledge hub
Die approbierte gedruckte Originalversion dieser Diplomarbeit ist an der TU Wien Bibliothek verfügbar
The approved original version of this thesis is available in print at TU Wien Bibliothek.

Die approbierte gedruckte Originalversion dieser Diplomarbeit ist an der TU Wien Bibliothek verfügbar
The approved original version of this thesis is available in print at TU Wien Bibliothek.
TU Bibliothek WIEN Your knowledge hub

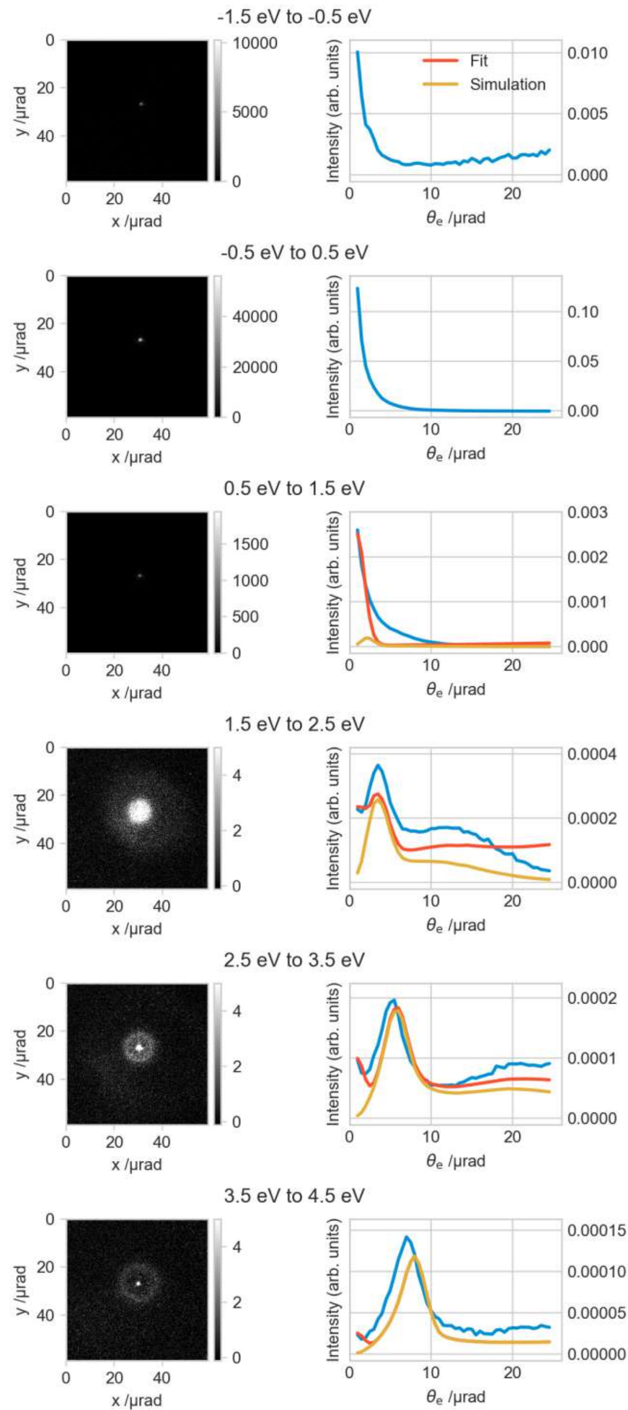

Figure 8.9.: Energy filtered low angle diffraction images of a 100 nm silicon membrane (left) and radial distributions with respect to the central maximum (right). The right plots include the simulations presented in section 6.1. The fit accounts for the contribution of the central beam (modeled by a Gaussian distribution with a standard deviation of 1 μm and a constant background.

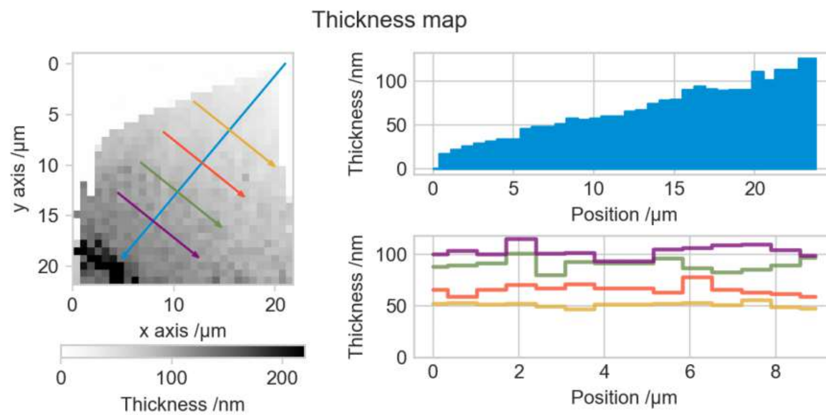

Figure 8.10.: Thickness map of a thin crystalline silicon sample (left), colored lines indicate regions of interest. Line profiles of the thickness along these regions of interest are depicted on the right. The blue line corresponds to the direction of maximum slope (top right), the other lines are perpendicular to the direction of maximum slope (bottom right) and consequently show almost constant thickness.

discernible in the radial intensity distribution.
However it does not always match the predicted distribution perfectly, this can easily be explained, when considering the imperfect geometry of the sample. Figure 8.10 shows a mapping of the thickness distribution of the sample. The line profile plotted on the right and indicated by the blue line on the thickness map corresponds to the direction of maximum slope. The other line profiles consequently show a more or less constant thickness in the direction orthogonal to the blue line. In the direction of maximum slope the thickness changes from zero to 125 nm over a distance of about 25 μm. This corresponds to an angle of $\alpha = 5$ mrad which is less than a third of a degree.
As previously discussed, a large area of the sample has to be illuminated in order to allow for good angular resolution. Even though α is comparatively small, it is still a significant deviation from the idealized situation that the simulations correspond to.
This sample geometry is a result of the preparation method: the iron polishing machine bombards the sample with a beam of argon ions at an angle of approximately 3 degrees. In this configuration the thinning of the sample is evidently non-uniform; in order to prepare a sample that matches the desired geometry more closely, a different preparation method is needed. Further experiments with better samples produced using Micro-Electro-Mechanical Systems (MEMS) manufacturing technology will be conducted as a follow up to this project.
Until the issue of sample geometry is addressed, we are unable to determine pre-

Die approbierte gedruckte Originalversion dieser Diplomarbeit ist an der TU Wien Bibliothek verfügbar
The approved original version of this thesis is available in print at TU Wien Bibliothek.
TU WIEN Bibliothek Your knowledge hub

cisely how well the simulations given in section 6.1 represents the experiment. Bearing these reservations in mind, we conclude nevertheless that the qualitative observation of deflection corresponding to guided modes and the good quantitative agreement of the deflection angle on the light line indicate that photons are indeed produced and that their momentum should be correlated to the detected electrons. These observations on the electron side suggest that this setup is indeed very promising for measuring correlations in electron-photon pairs.

Measurements on the photon side also confirms that we are able to detect and time photons with reasonable efficiency. Using the single photon counting modules and irradiating the sample with 3.3 nA of current in STEM mode, we observed approximately 150 000 photon counts per second (depending on sample and measurement site) near the focal point of the Vulcan system. This corrensponds to a joint probability of producing and detecting a photon of $\alpha_\gamma p \approx 7.3 \cdot 10^{-6}$.

Figure 8.11 illustrates measurements taken with the Vulcan systems spectrometer: Counts given here represent arbitrary units and are not directly comparable to results obtained with the single photon counting modules. Data was recorded in two separate runs scanning the same area under the same parameters, once only collecting signal from the top mirror, once only collecting signal from the bottom mirror. The top left heat map shows the measured total intensity obtained by summing over the total intensity in the spectrum over both runs at that respective point.The top right heat map in figure 8.11 shows the fraction of total intensity collected in the top mirror. The blue line in the heat map marks the selected region for the total intensity line profile shown below. It is overlaid with the thickness profile shown in figure 8.10 which was acquired at the same positions. The dashed lines mark the regions of interest from which the spectra below are extracted, each of these spectra represents the mean of all spectra recorded in the respective region of interest, the shaded regions in the background indicate the standard deviation between the spectra. In a sample like this one, the recorded spectrum should depend on the thickness of the material at the measured position [52]. As shown in figure 8.10, the regions corresponding to the dashed lines in figure 8.11 are selected such as to have an approximately constant thickness, therefore the resulting spectra within one region are expected to be similar. The thickness dependence can indeed be observed in the recorded spectra.

Die approbierte gedruckte Originalversion dieser Diplomarbeit ist an der TU Wien Bibliothek verfügbar
The approved original version of this thesis is available in print at TU Wien Bibliothek.
TU WIEN Bibliothek Your knowledge hub

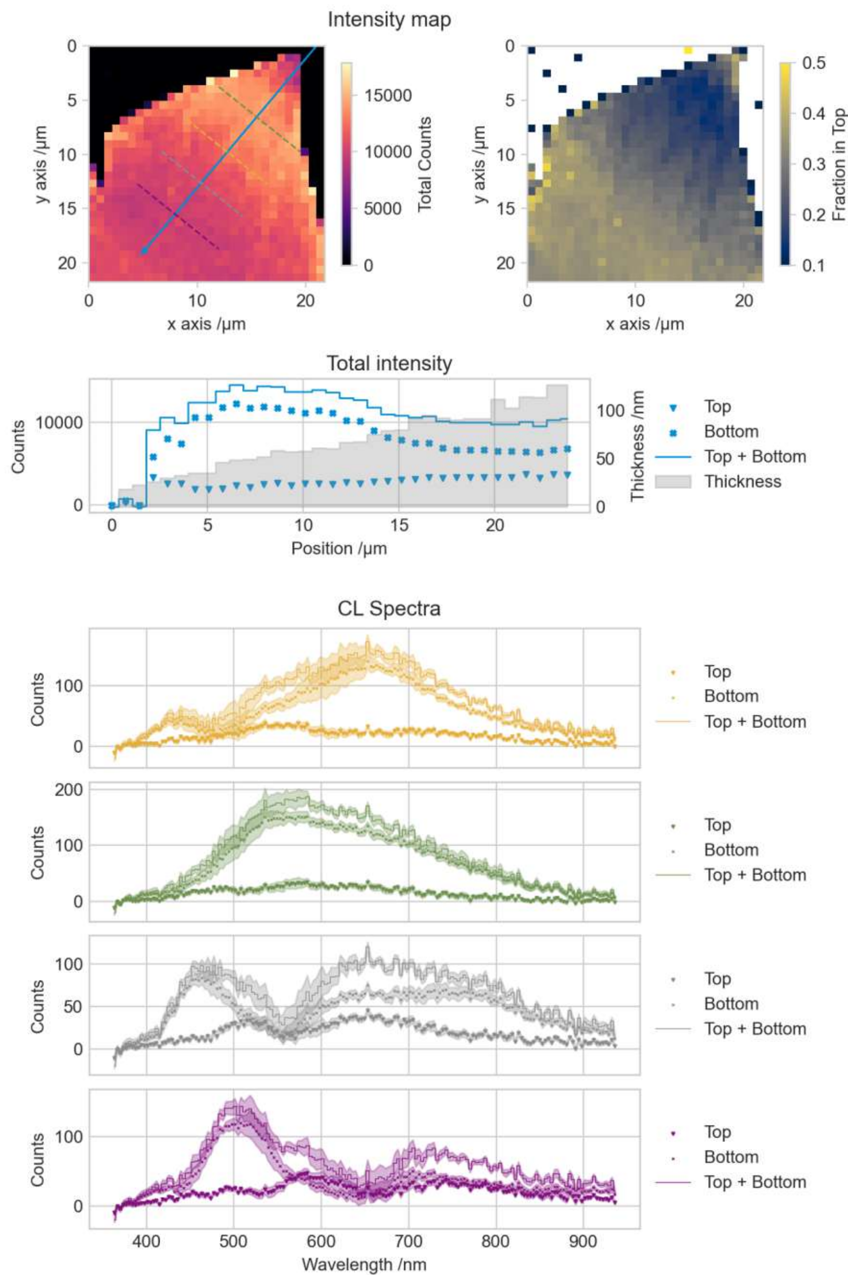

Figure 8.11.: CL measurement on thin crystalline silicon sample. A mapping of total intensity (top left) shows colored lines marking regions of constant thicknesses. The top right plot shows a mapping of the fraction of total intensity collected in the top mirror. The total intensity plot shows intensity in the region of interest that corresponds to the direction of maximum slope in thickness (blue line) and the corresponding thickness of the sample. Four CL spectra show the average spectrum and its standard deviation for each of the regions marked above (dashed lines in top left mapping). Minima and maxima shift with different sample thickness as expected.

Die approbierte gedruckte Originalversion dieser Diplomarbeit ist an der TU Wien Bibliothek verfügbar
The approved original version of this thesis is available in print at TU Wien Bibliothek.
TU WIEN Bibliothek Your knowledge hub

9. Further Setups

9.1. Microspheres

A very promising approach to realize aloof excitation is the use of microspheres. More specifically, spheres made from transparent dielectric materials, with a radius on the order of micrometers. This setup is significantly easier to handle, as microspheres can be bought ready made from various materials and in various sizes. The spheres, which are obtained in dry form (resembling a powder), can simply be placed on a TEM grid that is prepared with a surface modification like lacey carbon or a formvar film. The alignment with respect to the beam is very simple because of the rotational symmetry of the sphere. CL from the resulting sample can simply be measured using the Gatan Vulcan system. Microspheres are a particularly interesting kind of sample, as they exhibit mode selection when irradiated with electrons, this has already been shown in [5].
The modes present in such spherical structures are referred to as whispering gallery modes and have been described in various works [5] [63] [64]. The name "whispering gallery mode" stems from a phenomenon known from acoustics: in circular domes, even faintest noises emitted near the edge of the dome travel very far along its circumference as the sound waves are reflected from the outer walls. An expression for a pseudo free spectral range, which is the difference in frequency between two modes that only differ in quantum number l by $\Delta l = 1$ (see [63]):

$$\Delta\nu \approx \frac{c}{2\pi R \cdot n}$$

Where R is the radius of the sphere and n is the refractive index of the material. In the picture of ray optics, l can be identified with the number of wavelength equal to one circumference, i.e.:

$$2\pi R = l \cdot \frac{\lambda}{n}$$

The situation in our measurement is illustrated in figure 9.1: The electron beam passes close to the microsphere and emits a photon into one of its allowed modes via the Cherenkov effect. Due to mode selection, we expect to see modulations on the otherwise broadly distributed Cherenkov radiation. The visibility of these fringes

Die approbierte gedruckte Originalversion dieser Diplomarbeit ist an der TU Wien Bibliothek verfügbar
The approved original version of this thesis is available in print at TU Wien Bibliothek.
TU WIEN Bibliothek Your knowledge hub

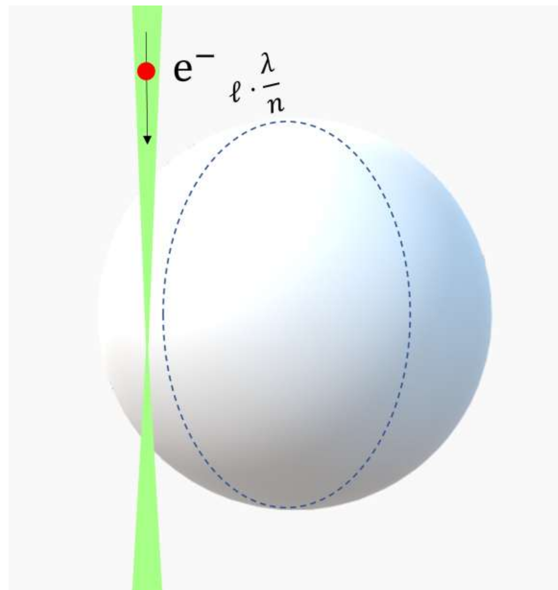

Figure 9.1.: Schematic depiction of an electron beam coupling to a whispering gallery mode in a dielectric microsphere. The length of the circumference (dashed blue line) must be a multiple of the wavelength λ/n of the emitted light in the material, with λ being the wavelength in vacuum and n referring to the materials refractive index. How many wavelengths fit within the circumference for a particular mode is given by l.

Die approbierte gedruckte Originalversion dieser Diplomarbeit ist an der TU Wien Bibliothek verfügbar
The approved original version of this thesis is available in print at TU Wien Bibliothek.
TU WIEN Bibliothek Your knowledge hub

is determined by the quality factor of the resonator (among other influences). Typically a higher refractive index, a precise sample geometry and a larger radius contribute to a high quality factor.
The experiment has been conducted with two types of microspheres: firstly we used silicon dioxide microspheres with Refractive index of 1.45 and a diameter of 1.5 µm (Bangs Laboratories, Inc.; product number SS04001 [65]), mounted on a lacey carbon grid, this sample is depicted in figure 9.3a, secondly we used barium titanate with a refractive index between 1.9 and 2.2 according to the manufacturer and a radius of approximately 1.5 µm (Cospheric LLC, product number BTGMS-4.15 [66]) mounted on a formvar film (See Figure 9.2a). Figures 9.3b and 9.2b show the results of the cathodoluminescence measurements for the respective samples. On both samples a line scan was done, taking spectra at regularly spaced positions. The trajectories of the line scans are indicated in figures 9.3a and 9.2b respectively. For the barium titanate sample the line scan started at vacuum position and progressed towards the center of the sphere, for the silicon dioxide sample the line scan started inside the sphere and moved out radially into vacuum. The respective plots presenting data collected by the high angle annular dark field (HAADF) detector (titled "HAADF signal") indicate whether electrons were scattered too high angles at the corresponding beam position and consequently show whether the beam was hitting the sample directly. Fringes indicating mode selection are visible in the spectra for both samples, however more clearly so for the barium titanate sample. For this sample, the spectrum indicated by the orange line clearly shows that CL emission is visible in an aloof beam position, as the beam approaches the sphere one observes a change in the detected modes, the electron seems to couple into different sets of modes at different positions.
To conclude: this setup is fairly easy to prepare and allows for detection of cathodoluminescence and electrons in aloof configuration. It is therefore suitable for observing correlated electron-photon pairs. One characteristic aspect of this setup to consider is the fact that the electric field is oriented in parallel to the beam trajectory for this geometry, therefore the electron is not deflected laterally when emitting a photon: when it loses energy it is slowed down parallel to the beam axis.

9.2. Aloof Experiments

The most straightforward geometry for achieving aloof photon excitation via the Cherenkov effects is simply to let the electron beam pass close to the surface of a bulk piece of dielectric. As discussed in section 6.2 the emission probability, compared to the probability in the bulk material, depends on the distance to the surface according to the equation given by [35]. Samples of this type were produced

Die approbierte gedruckte Originalversion dieser Diplomarbeit ist an der TU Wien Bibliothek verfügbar
The approved original version of this thesis is available in print at TU Wien Bibliothek.
TU Bibliothek WIEN Your knowledge hub

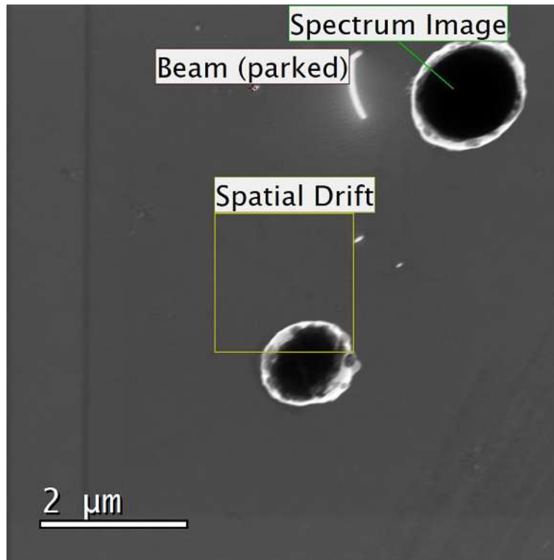

(a) STEM image of barium titanate microsphere on lacy carbon grid

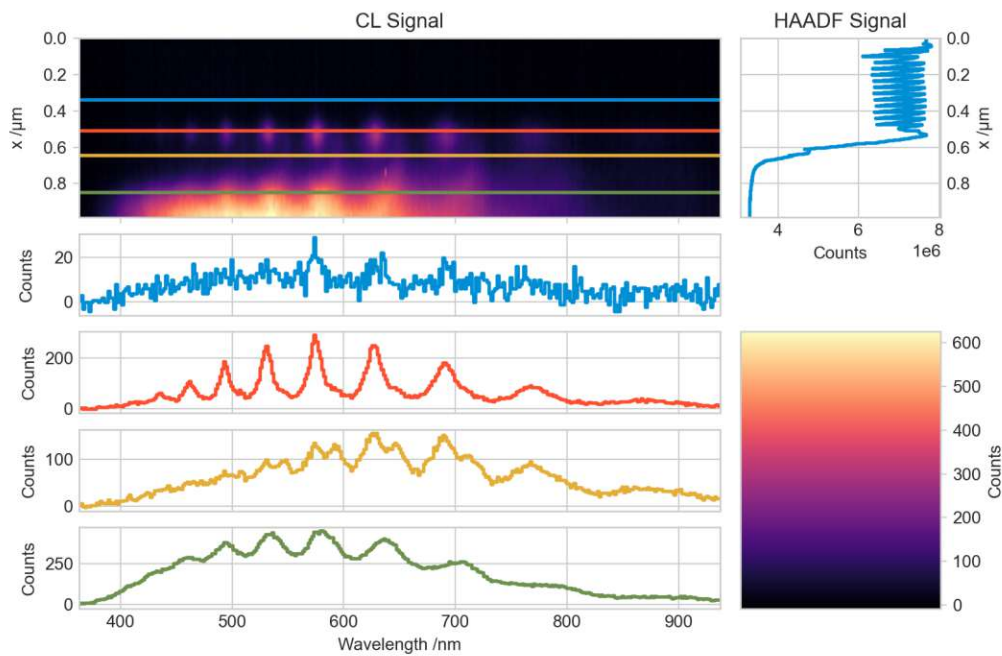

(b) Mode selection in silicon dioxide microspheres indicated by fringes in the CL spectrum. Spectra are recorded at different positions x along the green line shown in (a) and plotted as a mapping. Solid lines indicate where the spectra shown below were taken. HAADF signal shows elastic scattering by the sample (blue line is far away from the sample, green line is close).

Figure 9.2.

Die approbierte gedruckte Originalversion dieser Diplomarbeit ist an der TU Wien Bibliothek verfügbar
The approved original version of this thesis is available in print at TU Wien Bibliothek.
TU WIEN Bibliothek Your knowledge hub

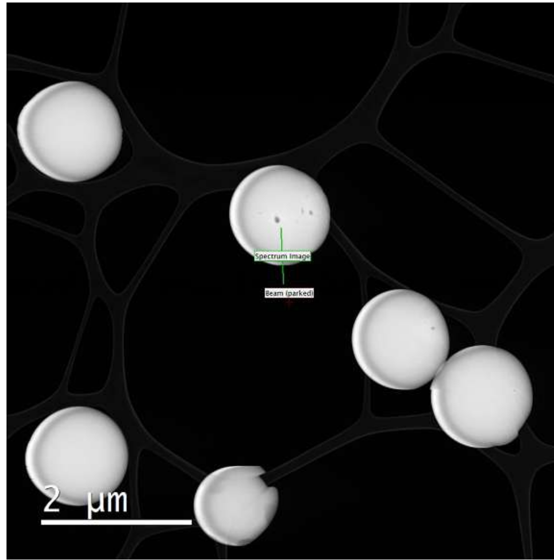

(a) STEM image of silicon dioxide microspheres.

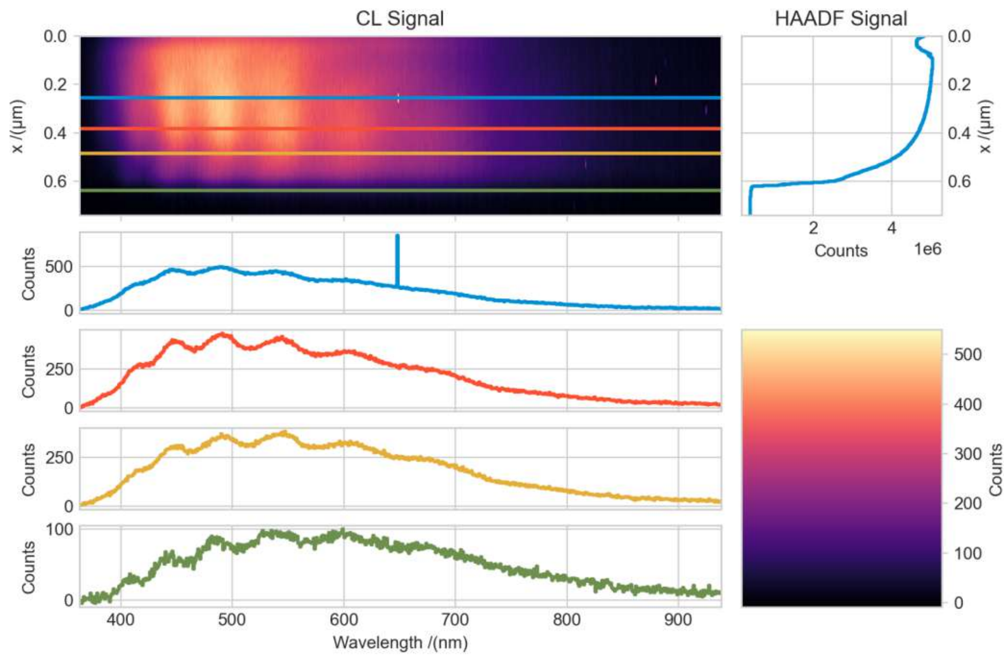

(b) Mode selection in silicon dioxide microspheres indicated by fringes in the CL spectrum. Spectra are recorded at different positions x along the green line shown in (a) and plotted as a mapping. Solid lines indicate where the spectra shown below were taken. HAADF signal shows elastic scattering by the sample. Note that HAADF contrast in (a) is inverted with respect to figure 9.2. Here the HAADF signal is high at the sample and low far away from the sample (blue line is close to the sample, green line is far away).

Figure 9.3.

Die approbierte gedruckte Originalversion dieser Diplomarbeit ist an der TU Wien Bibliothek verfügbar
The approved original version of this thesis is available in print at TU Wien Bibliothek.
TU WIEN Bibliothek Your knowledge hub

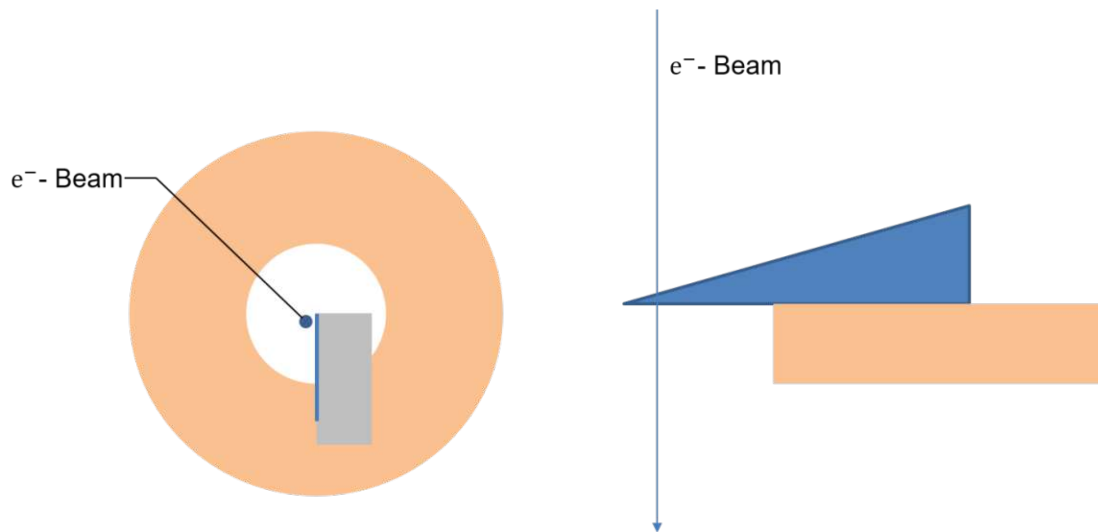

Figure 9.4.: Schematic image of a sample for aloof excitation in top view (left) and side view (right). A wedge shaped piece of dielectric material (gray) is glued onto a standard copper TEM grid, the electron beam (blue arrow) passes close to the sample surface. The interaction surface should be as well polished as possible.

following two approaches:
The first approach is illustrated in figure 9.4: a wedge shaped piece of dielectric material is placed on a standard TEM copper grid; cathodoluminescence can be measured using the Vulcan system.
Figure 9.5 shows the last of three samples which were prepared in order to test this approach. The dielectric material used is a 450 nm band pass filter. This filter consisted of alternating layers of two distinct dielectric materials on a silica substrate. The filtering effect is achieved by engineering the thicknesses of the individual layers in the system, thereby modifying the photonic density of states. The wedge shape of the sample makes it possible to vary the interaction length of the electron. As discussed previously, it is rather difficult to align the beam to the sample therefore it is advantageous to be able to start with a small interaction length and gradually improve the alignment.
The sample was prepared by Dominik Hornof as part of his bachelor's thesis by cutting the filter with a wire saw. At its tip the interaction region is approximately 5 micrometers long.
A practical advantage of starting from the filter is the very high quality surface, that allows for a homogeneous interaction region for the electron. Another interesting feature of this sample is the fact that filtering is achieved by engineering the allowed modes in the material, one would therefore assume that the Cherenkov

Die approbierte gedruckte Originalversion dieser Diplomarbeit ist an der TU Wien Bibliothek verfügbar
The approved original version of this thesis is available in print at TU Wien Bibliothek.
TU WIEN Bibliothek Your knowledge hub

(a) Top view

(b) Side view of the sample showing the interaction region at the tip of the wedge.

Figure 9.5.: Microscope images of the filter wedge sample also illustrated in figure 9.4.

radiation produced will also be restricted to those allowed modes. Clear disadvantages as a first approach for generating photons in the aloof configuration are the comparatively low refractive index of silica and the added complexity of the sample due to the alternating layers.

Multiple measurements on samples of this type were made and some seem to show a small but clearly discernible probability for aloof Cherenkov emission, however more experiments would be needed before giving decisive confirmation.

Figure 9.6 illustrates an alternative approach: a thin piece of dielectric material, in this case zirconia (crystalline zirconium dioxide) is prepared using focused ion beam milling. It is placed on the end face of a multimode optical fiber. Heating the fiber makes it possible to bend it at a radius of the few millimeters, which makes it possible to orient the fiber in such a way that the end phase can be aligned in parallel to the beam. As Cherenkov emission takes place at the Cherenkov angle we assume that it is advantageous to polish the fiber in such a way as to tilt the fiber end-face with respect to the fiber cross section.

Figure 9.7 shows such a sample, 9.7a and 9.7b show SEM images of the zirconia piece on the optical fiber. The top view in 9.7b indicated that the lamella should be long enough to allow for the unperturbed passage of the beam. Figure 9.7c shows the same view in the TEM, the lamella is clearly distinguishable from the supporting fiber in this projected view. By connecting the end of the multimode fiber to a single photon counting module, one can measure the cathodoluminescence produced in the zirconia lamella. The detected photon rate is significant (approximately 300 counts/pA/s) when hitting the edge of the zirconia lamella however

Die approbierte gedruckte Originalversion dieser Diplomarbeit ist an der TU Wien Bibliothek verfügbar
The approved original version of this thesis is available in print at TU Wien Bibliothek.
TU WIEN Bibliothek Your knowledge hub

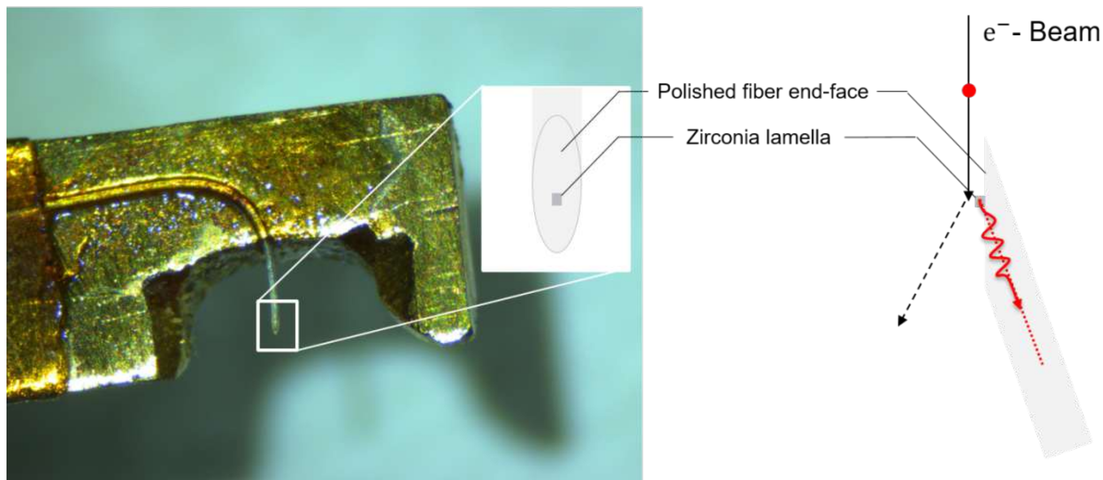

Figure 9.6.: Schematic image of a zirconia lamella attached to a multimode fiber polished at a 70° angle. The bent multimode fiber is glued onto a specimen holder (photograph on the left). The fiber carries a small piece of zirconia for the electron beam (black arrow) to pass close to and emit a photon (red arrow).

strong charging is observed and the electron beam is visibly distorted even at a relatively large distance from the sample. Scans of both cathodoluminescence and the signal on the HAADF detector were made but the results are inconclusive as to whether the cathodoluminescence actually originates from aloof excitation. Figure 9.7d confirms that the photon detection efficiency was actually high enough to detect photon coincidences. For this measurement, a Hanbury-Brown and Twiss interferometer was used, detected photons on both channels were time tagged and the differences between individual photon detection times were computed for all detections within a sliding time window of 130 nanoseconds. The graph shows a histogram of these time differences. As described in reference [59], the peak at delta t = 0 indicates the coherent emission of the photons.

While this setup seems to allow for efficient photon collection, the preparation of the fiber as well as the management of the charging introduces significant experimental overhead and complicates the interpretation of the measurements. Using an optical fiber as part of a TEM sample introduces a comparatively large piece of insulator into the microscope making these issues very hard to avoid in this configuration. For all these reasons, this approach was not pursued further after some initial experiments. Correlated measurements of electron photon pairs may still be possible with a more refined version of this setup.

Die approbierte gedruckte Originalversion dieser Diplomarbeit ist an der TU Wien Bibliothek verfügbar
The approved original version of this thesis is available in print at TU Wien Bibliothek.
TU WIEN Bibliothek Your knowledge hub

Die approbierte gedruckte Originalversion dieser Diplomarbeit ist an der TU Wien Bibliothek verfügbar
The approved original version of this thesis is available in print at TU Wien Bibliothek.
TU Bibliothek Your knowledge hub WIEN

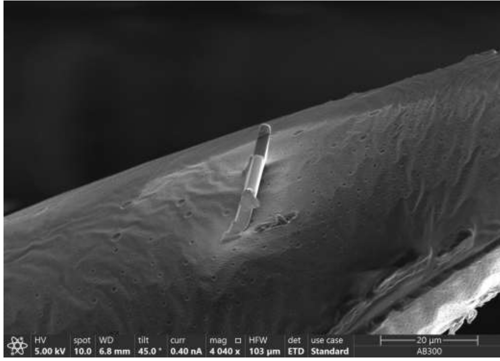

(a) SEM image of fiber sample (oblique view)

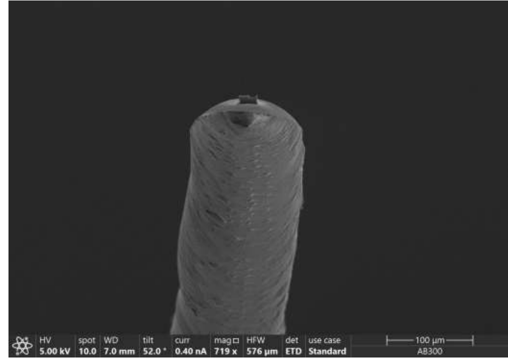

(b) SEM image of fiber sample (top view)

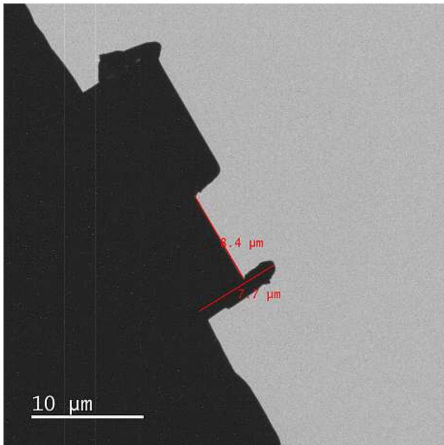

(c) TEM image of fiber sample (top view)

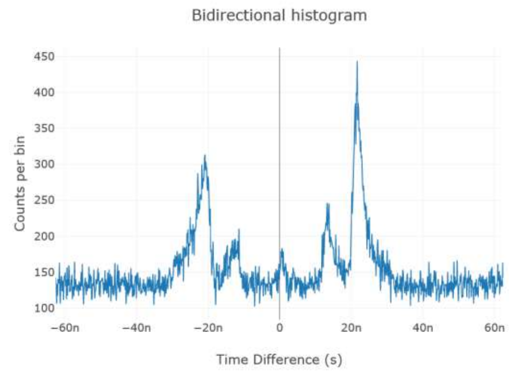

(d) Temporal photon-photon correlations measured at the edge of the zirconia piece using a Hanbury-Brown Twiss interferometer.

Figure 9.7.: Zirconia lamella mounted on angled multimode fiber as illustrated in figure 9.6.

9.3. Multi-slit Masks

Another potentially interesting setup that would allow for aloof Cherenkov emission is the use of multi-slit masks. In this setup a membrane from a material with a high refractive index is used. If necessary, it is coated with an additional layer of high-Z material in order to make it intransparent to electrons. Finally focused ion beam milling is used to cut an array of slits into the membrane. When the sample is illuminated with electrons only those electrons that pass through the slits are transmitted, this technique is often used in electron holography [67][68] . If the slits are narrow enough, each electron that is transmitted, will pass in very close proximity to some dielectric material and has a probability of emitting a Cherenkov photon. Figure 9.8 illustrates this measurement scheme. This setup is interesting for multiple reasons: firstly it provides all the advantages of the aloof configuration: a thicker membrane can potentially allow for a longer interaction region, there is no need to use crystalline material, other incoherent processes are strongly suppressed compared to Cherenkov emission because of their higher energy transfer and elastic scattering of the electrons is very sharply defined by the lattice constant of the multi-slit. Another interesting aspect is the fact that the elastic scattering can be engineered to be on the same order of magnitude as the deflection due to Cherenkov emission, which could allow for interference of electrons from two separate interference maxima.
Only some very limited preliminary measurements have been made on this type of sample. Figure 9.10 shows an overview image of the mask that has been used. The period of this mask is approximately 315 nanometers which corresponds to a deflection of about 7.7 µrad for a 200 keV electron. By illuminating an area that is approximately twice as large in diameter as the mask itself, setting the microscope to low angle diffraction mode, selecting a long camera length and adjusting the objective lens current in order to obtain sharp peaks, the elastic scattering from this slit array can be resolved, its diffraction pattern is shown in figure 9.9.
The sample shown in figure 9.10 consists of a 100 nm silicon nitride membrane coated with a 200 nm layer of platinum, The layout of the mask is such that the slits are equally wide as the intransparent parts, which is about 157.5 nm. The measured amount of cathodoluminescence is consistent with what has also been measured for a simple silicon nitride membrane (see section 8.1). When scanning the sample with a focused probe, and measuring the total CL produced using the Vulcan systems photomultiplier tube, it is evident, that CL is also detected when passing the focused beam through its slits. As the photon emission probabilities both for this sample as for the simple silicon nitride membrane are very low, the setup would need to be adapted and further experiments would have to be made in order to make it suitable for the detection of correlated electron photon pairs. This approach has not pursued further in this project however I am convinced that

Die approbierte gedruckte Originalversion dieser Diplomarbeit ist an der TU Wien Bibliothek verfügbar
The approved original version of this thesis is available in print at TU Wien Bibliothek.
TU WIEN Bibliothek Your knowledge hub

Die approbierte gedruckte Originalversion dieser Diplomarbeit ist an der TU Wien Bibliothek verfügbar
The approved original version of this thesis is available in print at TU Wien Bibliothek.

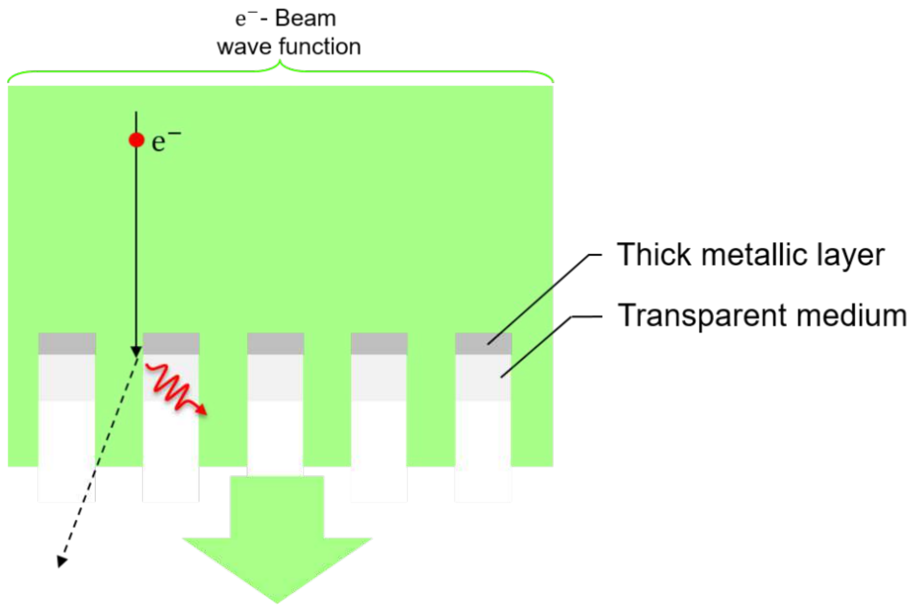

Figure 9.8.: Schematic of multi-slit setup. The electron wave function (green) broadly illuminates a multi-slit mask cut from a dielectric membrane. As the slits are narrow, electrons passing through have a high probability of aloof photon excitation on the mask. The black arrow shows an arbitrary example of a possible classical electron trajectory.

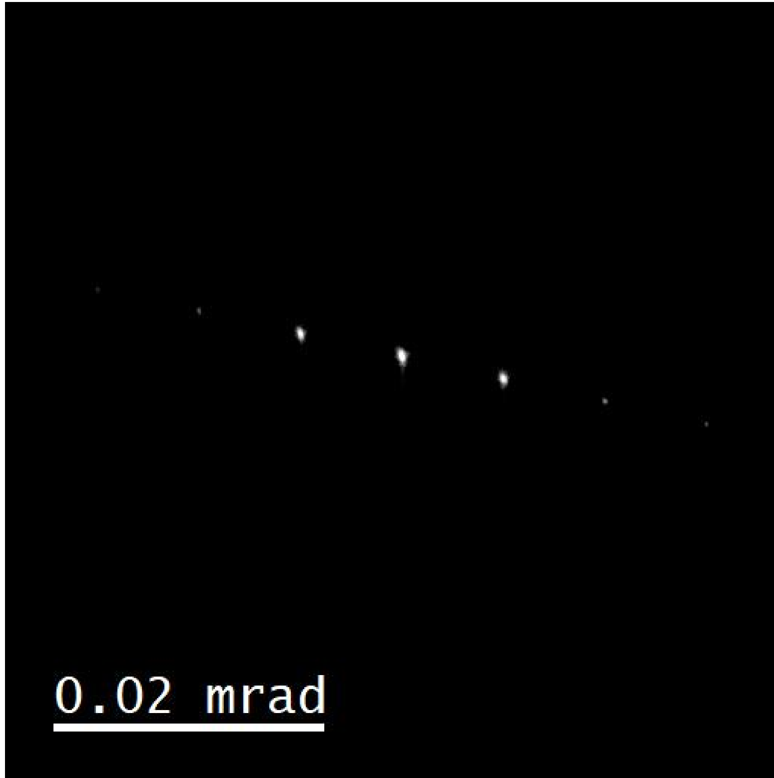

Figure 9.9.: Diffraction Pattern produced by the multi-slit mask shown in figure 9.10

Die approbierte gedruckte Originalversion dieser Diplomarbeit ist an der TU Wien Bibliothek verfügbar
The approved original version of this thesis is available in print at TU Wien Bibliothek.
TU Bibliothek Your knowledge hub WIEN

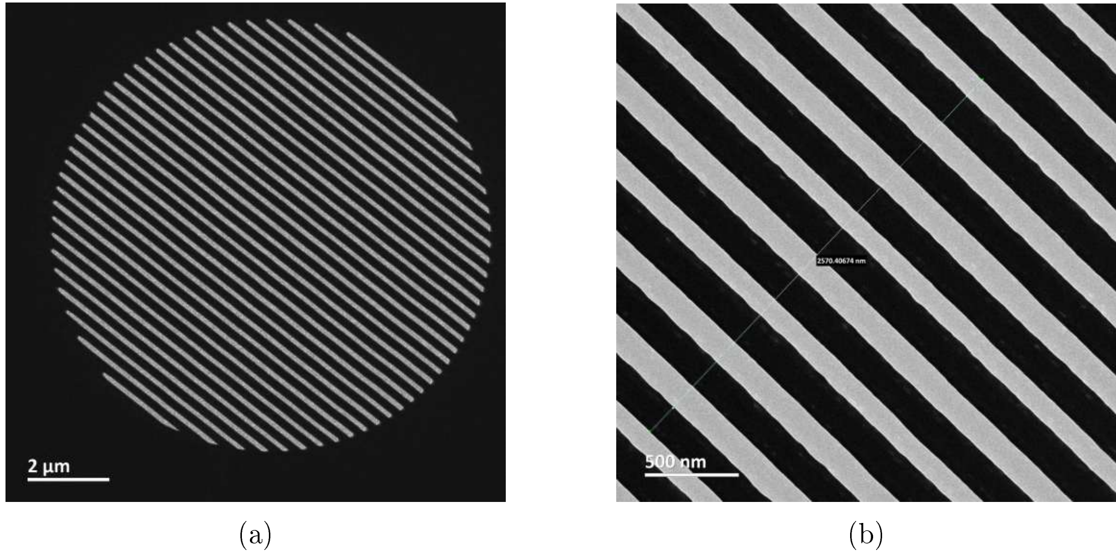

(a) (b)

Figure 9.10.: TEM images of a multi-slit mask with a periodicity of 321 nm, made from platinum coated silicon nitride (as illustrated in figure 9.8).

it would make for an interesting direction in future experiments.

Die approbierte gedruckte Originalversion dieser Diplomarbeit ist an der TU Wien Bibliothek verfügbar
The approved original version of this thesis is available in print at TU Wien Bibliothek.
TU WIEN Bibliothek Your knowledge hub

10. Conclusion and Outlook

This work is a contribution to Prof. Haslinger's Quantum Optics with Electron Photon Pairs (QOEPP) project, which I joined at a very early stage. While its goal and its theoretical foundation were already established, experimental work on the transmission electron microscope, in particular on samples that allowed for the simultaneous detection of electrons and photons was only starting. During this exploratory phase of the project a lot of effort was put into trying out different experimental approaches, many of which turned out to be impractical. In this work, four promising experimental configurations (sample plus measurement scheme) were identified and investigated experimentally. For each of them it was possible to measure the distribution of the electron, either in position, momentum or energy and a photon emission rate was measured. The thin crystalline silicon membrane was identified as a viable platform for a correlated coincidence measurement of electron and photon momentum. The corresponding measurement setup and procedure was described, a detailed theoretical description for energy loss and deflection probabilities for this sample was obtained and experimentally verified. An investigation of potential interfering effects and sources of noise concluded, that the proposed experiment should be viable. In the meantime, the USTEM has upgraded the Tecnai F20 with a Timepix3 camera, as required for the described experiment. In the short term the QOEPP project will complete the setup described previously by synchronizing the timing of electron and photon detection and programming suitable control and data analysis software. Having completed this step, we will finally be able to conduct coincidence measurements in momentum, energy and position. In the medium term, a large goal of the QOEPP project is to develop schemes for verifying entanglement between electrons and coherently emitted photon. A success on this goal would form a promising starting point for exploring further experiments that investigate concepts from the field of quantum optics in the context of electron-photon pairs.

TU WIEN Bibliothek Your knowledge hub
Die approbierte gedruckte Originalversion dieser Diplomarbeit ist an der TU Wien Bibliothek verfügbar
The approved original version of this thesis is available in print at TU Wien Bibliothek.

Acknowledgments

I want to extend my heartfelt gratitude to the people and organizations who have played an essential role in making my Master's thesis a reality. Their unwavering support, guidance, and dedication have been indispensable throughout this project.
First and foremost, I would like to express my appreciation to Professor Philipp Haslinger, my supervisor. His mentorship has been invaluable in shaping my understanding of our field, and I am genuinely grateful for the numerous engaging discussions, the guidance, and the incredible opportunities he has provided. Professor Haslinger's passion for experimental physics has been a constant source of motivation.
My gratitude also goes out to Thomas Schachinger, for his exceptional patience and commitment with which he helped me learn the intricacies of transmission electron microscopy and explained a multitude of other aspects in electron microscopy to me. His willingness to share his expertise has been indispensable in the development of this thesis.
A special note of appreciation is due to Dominik Hornof for his outstanding contributions to this project. His tireless dedication and hard work, were central to the progress of the QOEPP project and thereby also contributed greatly to the completion of this work.
I would also like to acknowledge the USTEM team and the other members of the Haslinger group for their camaraderie, support, and readiness to assist whenever I needed their guidance or insights. Their collaboration has made this research experience both enjoyable and productive.
Additionally, I want to express my gratitude to the Austrian Science Fund (FWF) for their generous support of the QOEPP project, to which this thesis was a contribution to. Without their financial backing this work would of course not have been possible.
Finally, I want to convey my profound appreciation to my family and friends for their unwavering encouragement and understanding throughout this academic journey.
To all those mentioned above, and to anyone else who may have contributed in any way, I extend my sincere thanks. It has been a privilege to collaborate with all of you.

Die approbierte gedruckte Originalversion dieser Diplomarbeit ist an der TU Wien Bibliothek verfügbar
The approved original version of this thesis is available in print at TU Wien Bibliothek.
TU WIEN Bibliothek Your knowledge hub

Bibliography

[1] T. Coenen and N. M. Haegel, "Cathodoluminescence for the 21st century: learning more from light", Applied Physics Reviews **4**, 031103 (2017).

[2] B. G. Yacobi and D. B. Holt, "Cathodoluminescence scanning electron microscopy of semiconductors", Journal of Applied Physics **59**, R1–R24 (1986).

[3] A. Losquin and M. Kociak, "Link between cathodoluminescence and electron energy loss spectroscopy and the radiative and full electromagnetic local density of states", ACS Photonics **2**, 1619–1627 (2015).

[4] I. C. Bicket, E. P. Bellido, S. Meuret, A. Polman, and G. A. Botton, "Correlative electron energy loss spectroscopy and cathodoluminescence spectroscopy on three-dimensional plasmonic split ring resonators", Microscopy **67**, i40–i51 (2018).

[5] Y. Auad, C. Hamon, M. Tencé, H. Lourenço-Martins, V. Mkhitaryan, O. Stéphan, F. J. García de Abajo, L. H. Tizei, and M. Kociak, "Unveiling the coupling of single metallic nanoparticles to whispering-gallery microcavities", Nano Letters **22**, 319–327 (2022).

[6] D. Jannis, K. Müller-Caspary, A. Béché, A. Oelsner, and J. Verbeeck, "Spectroscopic coincidence experiments in transmission electron microscopy", Applied Physics Letters **114**, 143101 (2019).

[7] N. Varkentina, Y. Auad, S. Y. Woo, A. Zobelli, L. Bocher, J.-D. Blazit, X. Li, M. Tencé, K. Watanabe, T. Taniguchi, O. Stéphan, M. Kociak, and L. H. G. Tizei, "Cathodoluminescence excitation spectroscopy: nanoscale imaging of excitation pathways", Science Advances **8**, eabq4947 (2022).

[8] A. Feist, G. Huang, G. Arend, Y. Yang, J. W. Henke, A. S. Raja, F. J. Kappert, R. N. Wang, H. Lourenço-Martins, Z. Qiu, J. Liu, O. Kfir, T. J. Kippenberg, and C. Ropers, "Cavity-mediated electron-photon pairs", Science **377**, 777–780 (2022).

[9] R. Marchand, R. Šachl, M. Kalbáč, M. Hof, R. Tromp, M. Amaro, S. J. V. D. Molen, and T. Juffmann, "Optical near-field electron microscopy", Physical Review Applied **16**, 014008 (2021).

Die approbierte gedruckte Originalversion dieser Diplomarbeit ist an der TU Wien Bibliothek verfügbar
The approved original version of this thesis is available in print at TU Wien Bibliothek.
TU WIEN Bibliothek Your knowledge hub

[10] S. A. Koppell, M. Mankos, A. J. Bowman, Y. Israel, T. Juffmann, B. B. Klopfer, and M. A. Kasevich, “Design for a 10 keV multi-pass transmission electron microscope”, Ultramicroscopy **207**, 112834 (2019).

[11] D. Rätzel, D. Hartley, O. Schwartz, and P. Haslinger, “Controlling quantum systems with modulated electron beams”, Physical Review Research **3**, 023247 (2021).

[12] D. B. Williams and C. B. Carter, *Transmission electron microscopy : a textbook for materials science*, 2nd ed. (Springer, New York, 2009).

[13] J. C. H. Spence, *High-resolution electron microscopy*, 4th ed. (Oxford University Press, Oxford, 2013).

[14] R. Egerton, *Physical principles of electron microscopy : an introduction to TEM, SEM and AEM*, 2nd ed. (Springer, New York, 2016).

[15] W. Heisenberg, *Die physikalischen Prinzipien der Quantentheorie* (Hirzel, Leipzig, 1930).

[16] J. M. Zuo and J. C. H. Spence, *Advanced transmission electron microscopy* (Springer, New York, 2017).

[17] O. L. Krivanek, N. Dellby, T. C. Lovejoy, N. J. Bacon, G. J. Corbin, P. Hrncirik, Z. S. Szilagyi, T. Aoki, R. W. Carpenter, P. A. Crozier, J. Zhu, P. Rez, R. F. Egerton, and P. E. Batson, “Exploring phonon signals by high energy / high spatial resolution EELS”, Microscopy and Microanalysis **20**, 66–67 (2014).

[18] R. Egerton, *Electron energy-loss spectroscopy in the electron microscope*, 3rd ed. (Springer, New York, 2011).

[19] K. Iakoubovskii, K. Mitsuishi, Y. Nakayama, and K. Furuya, “Mean free path of inelastic electron scattering in elemental solids and oxides using transmission electron microscopy: atomic number dependent oscillatory behavior”, Physical Review B - Condensed Matter and Materials Physics **77**, 104102 (2008).

[20] P. L. Potapov, “The experimental electron mean-free-path in Si under typical (S)TEM conditions”, Ultramicroscopy **147**, 21–24 (2014).

[21] K. Iakoubovskii and K. Mitsuishi, “Elastic scattering of 200 keV electrons in elemental solids: experimental observation of atomic-number-dependent oscillatory behavior”, Journal of Physics: Condensed Matter **21**, 155402 (2009).

[22] J. Langmore, “The collection of scattered electrons in dark-field electron microscopy”, Optik **38**, 335–350 (1973).

[23] F. Zernike, “Phase contrast, a new method for the microscopic observation of transparent objects”, Physica **9**, 686–698 (1942).

TU WIEN Bibliothek Your knowledge hub
Die approbierte gedruckte Originalversion dieser Diplomarbeit ist an der TU Wien Bibliothek verfügbar
The approved original version of this thesis is available in print at TU Wien Bibliothek.

[24]F. Zernike, “Phase contrast, a new method for the microscopic observation of transparent objects part II”, Physica **9**, 974–986 (1942).

[25]E. J. Kirkland, *Advanced computing in electron microscopy*, 2nd ed. (Springer, New York, 2010).

[26]J. Madsen and T. Susi, “abTEM: ab initio transmission electron microscopy image simulation”, Microscopy and Microanalysis **26**, 448–450 (2020).

[27]N. W. Ashcroft and N. D. Mermin, *Festkörperphysik*, 3rd ed., reprinted with corrections (Oldenbourg, Munich, 2007).

[28]E. Kvaalen, wikimedia.org, published under the CC BY-SA 4.0 license, `https://commons.wikimedia.org/wiki/File:Schematic_view_of_imaging_and_diffraction_modes_in_TEM.tif`.

[29]J. B. Pawley, “Points, pixels, and gray levels: digitizing image data”, in *Handbook of biological confocal microscopy*, edited by J. B. Pawley (Springer US, Boston, MA, 2006), pp. 59–79.

[30]Excelitas Technologies Corp., *SPCM-AQRH, single-photon counting module, silicon avalanche photodiode*, (2023) `https://www.excelitas.com/product/spcm-aqrh` (visited on 08/08/2023).

[31]W. Crookes, “On radiant matter; a lecture delivered to the british association for the advancement of science, at sheffield, friday, august 22, 1879”, American Journal of Science **3**, 241–262 (1879).

[32]M. Kociak and L. F. Zagonel, “Cathodoluminescence in the scanning transmission electron microscope”, Ultramicroscopy **176**, 112–131 (2017).

[33]C. M. Parish and P. E. Russell, “Scanning cathodoluminescence microscopy”, Advances in Imaging and Electron Physics **147**, 1–135 (2007).

[34]S. J. Smith and E. M. Purcell, “Visible light from localized surface charges moving across a grating”, Physical Review **92**, 1069 (1953).

[35]A. Howie, “Surface reactions and excitations”, Ultramicroscopy **11**, 141–148 (1983).

[36]P. A. Čerenkov, “Visible radiation produced by electrons moving in a medium with velocities exceeding that of light”, Physical Review **52**, 378 (1937).

[37]I. Tamm and I. Frank, “Coherent radiation of fast electrons in a medium”, in Dokl. akad. nauk sssr, Vol. 14, 3 (1937), pp. 107–112.

[38]J. D. Jackson, *Classical electrodynamics*, 3rd ed. (Wiley, New York, 1999).

[39]D. Ehrt, “Deep-UV materials”, Advanced Optical Technologies **7**, 225–242 (2018).

Die approbierte gedruckte Originalversion dieser Diplomarbeit ist an der TU Wien Bibliothek verfügbar
The approved original version of this thesis is available in print at TU Wien Bibliothek.
TU WIEN Bibliothek Your knowledge hub

[40] A. C. Thompson, D. T. Attwood, E. M.Gullikson, M. R. Howells, J. B. Kortright, A. L. Robinson, J. H. Underwoody, K.-J. Kim, J. Kirz, I. Lindau, P. Pianetta, H. Winick, G. P. Williams, and J. H. Scofield, *Center for x-ray optics - advanced light source - x-ray data booklet*, edited by A. Thompson, 3rd ed. (eScholarship Publishing, Berkeley, 2001).

[41] D. E. Aspnes and A. A. Studna, “Dielectric functions and optical parameters of Si, Ge, GaP, GaAs, GaSb, InP, InAs, and InSb from 1.5 to 6.0 eV”, Physical review. B, Condensed matter **27**, 985–1009 (1983).

[42] L. V. R.-d. Marcos, J. I. Larruquert, J. A. Méndez, and J. A. Aznárez, “Self-consistent optical constants of SiO2 and Ta2O5 films”, Opt. Mater. Express **6**, 3622–3637 (2016).

[43] E. Hecht, *Optics*, eng, 4th ed. (Addison-Wesley, San Francisco, 2002).

[44] N. Osakabe and T. Kodama, “Time-resolved electron microscopy by means of electron counting”, Physical Review B **56**, 5156 (1997).

[45] V. D. Giulio, M. Kociak, and F. J. García de Abajo, “Probing quantum optical excitations with fast electrons”, Optica **6**, 1524–1534 (2019).

[46] Y. Adiv, H. Hu, S. Tsesses, R. Dahan, K. Wang, Y. Kurman, A. Gorlach, H. Chen, X. Lin, G. Bartal, and I. Kaminer, “Observation of 2D cherenkov radiation”, Physical Review X **13**, 011002 (2023).

[47] D. Jannis, K. Müller-Caspary, A. Béché, and J. Verbeeck, “Coincidence detection of EELS and EDX spectral events in the electron microscope”, Applied Sciences **11**, 9058 (2021).

[48] F. J. García De Abajo, A. Rivacoba, N. Zabala, and N. Yamamoto, “Boundary effects in cherenkov radiation”, Physical Review B **69**, 155420 (2004).

[49] E. Kröger, “Berechnung der Energieverluste schneller Elektronen in dünnen Schichten mit Retardierung”, Zeitschrift fur Physik **216**, 115–135 (1968).

[50] A. Konečná, personal communication, Feb. 20, 2023.

[51] C. Schinke, P. C. Peest, J. Schmidt, R. Brendel, K. Bothe, M. R. Vogt, I. Kröger, S. Winter, A. Schirmacher, S. Lim, H. T. Nguyen, and D. Macdonald, “Uncertainty analysis for the coefficient of band-to-band absorption of crystalline silicon”, AIP Advances **5**, 067168 (2015).

[52] N. Yamamoto, H. Sugiyama, and A. Toda, “Cherenkov and transition radiation from thin plate crystals detected in the transmission electron microscope”, Source: Proceedings: Mathematical, Physical and Engineering Sciences **452**, 2279–2301 (1996).

[53] L. D. Marks, “Observation of the image force for fast electrons near an MgO surface”, Solid State Communications **43**, 727–729 (1982).

Die approbierte gedruckte Originalversion dieser Diplomarbeit ist an der TU Wien Bibliothek verfügbar
The approved original version of this thesis is available in print at TU Wien Bibliothek.
TU WIEN Bibliothek Your knowledge hub

[54] C. H. Chen, J. Silcox, and R. Vincent, "Electron-energy losses in silicon: bulk and surface plasmons and čerenkov radiation", Physical Review B **12**, 64 (1975).

[55] A. Schröder, L. van Velzen, M. Kelder, and S. Schäfer, "Improving the temporal resolution of event-based electron detectors using neural network cluster analysis", arXiv:2307.16666 [physics.ins-det] (2023).

[56] D. Turecek, J. Jakubek, and P. Soukup, "Usb 3.0 readout and time-walk correction method for timepix3 detector", Journal of Instrumentation **11**, C12065 (2016).

[57] M. Stöger-Pollach, K. Bukvišová, S. Schwarz, M. Kvapil, T. Šamořil, and M. Horák, "Fundamentals of cathodoluminescence in a stem: the impact of sample geometry and electron beam energy on light emission of semiconductors", Ultramicroscopy **200**, 111–124 (2019).

[58] M. Berger, J. Coursey, M. Zucker, and J. Chang, "Stopping-power and range tables for electrons, protons, and helium ions, nist standard reference database 124", National Institute of Standards and Technology (NIST), Physical Measurement Laboratory (PML) (2017).

[59] M. Scheucher, T. Schachinger, T. Spielauer, M. Stöger-Pollach, and P. Haslinger, "Discrimination of coherent and incoherent cathodoluminescence using temporal photon correlations", Ultramicroscopy **241**, 113594 (2022).

[60] H. R. Philipp, "Optical properties of silicon nitride", Journal of The Electrochemical Society **120**, 295 (1973).

[61] Micro to Nano, *EM Tec silicon nitride support films and membranes for EM*, (2023) `https://www.microtonano.com/EM-Tec-silicon-nitride-support-films-and-membranes-for-EM.php` (visited on 08/17/2023).

[62] A. I. Bailey and S. M. Kay, "Measurement of refractive index and dispersion of mica, employing multiple beam interference techniques", British Journal of Applied Physics **16**, 39 (1965).

[63] G. C. Righini, Y. Dumeige, P. Feron, M. Ferrari, G. Nunzi Conti, D. Ristic, and S. Soria, "Whispering gallery mode microresonators: fundamentals and applications", La Rivista del Nuovo Cimento **34**, 435–488 (2011).

[64] G. Schunk, J. U. Fürst, M. Förtsch, D. V. Strekalov, U. Vogl, F. Sedlmeir, H. G. L. Schwefel, G. Leuchs, and C. Marquardt, "Identifying modes of large whispering-gallery mode resonators from the spectrum and emission pattern", Opt. Express **22**, 30795–30806 (2014).

[65] Bangs Laboratories inc., *Non-functionalized silica*, (2023) `https://www.bangslabs.com/products/silica-microspheres/non-functionalized-silica` (visited on 08/16/2023).

TU WIEN Bibliothek Your knowledge hub
Die approbierte gedruckte Originalversion dieser Diplomarbeit ist an der TU Wien Bibliothek verfügbar
The approved original version of this thesis is available in print at TU Wien Bibliothek.

[66]Cosperic LLC, *Retroreflective spheres for motion tracking in medical device applications*, (2020) https://www.cospheric.com/BTGMSc_solid_glass_spheres_beads_microns.htm (visited on 08/16/2023).

[67]T. Schachinger, P. Hartel, P.-H. Lu, S. Löffler, M. Obermair, M. Dries, D. Gerthsen, R. Dunin-Borkowski, and P. Schattschneider, "Experimental realization of a $\pi/2$ vortex mode converter for electrons using a spherical aberration corrector", Ultramicroscopy **229**, 113340 (2021).

[68]P. Schattschneider, M. Stöger-Pollach, and J. Verbeeck, "Novel vortex generator and mode converter for electron beams", Phys. Rev. Lett. **109**, 084801 (2012).

TU Bibliothek WIEN Your knowledge hub
Die approbierte gedruckte Originalversion dieser Diplomarbeit ist an der TU Wien Bibliothek verfügbar
The approved original version of this thesis is available in print at TU Wien Bibliothek.

A. Reciprocal Space

For an infinite three-dimensional lattice with the primitive vectors$(\vec{a_1}, \vec{a}_2, \vec{a}_3)$, any lattice point $\vec{R}_i$ is given by:

$$\vec{R}_i = n_1\vec{a}_1 + n_2\vec{a}_2 + n_3\vec{a}_3$$

with (n_1, n_2, n_3) being integer numbers.
Its reciprocal lattice is given by

$$\vec{G}_i = k_1\vec{b}k_1 + k_2\vec{b}_2 + k_3\vec{b}_3$$

with (k_1, k_2, k_3) again being integers.
Its three reciprocal primitive vectors $\left(\vec{b_1}, \vec{b}_2, \vec{b}_3\right)$ can be determined using the following expressions from [27]:

$$\vec{b}_1 = 2\pi\frac{\vec{a}_2 \times \vec{a}_3}{\vec{a}_1 \cdot (\vec{a}_2 \times \vec{a}_3)} \tag{A.1}$$

$$\vec{b}_2 = 2\pi\frac{\vec{a}_3 \times \vec{a}_1}{\vec{a}_1 \cdot (\vec{a}_2 \times \vec{a}_3)} \tag{A.2}$$

$$\vec{b}_3 = 2\pi\frac{\vec{a}_1 \times \vec{a}_2}{\vec{a}_1 \cdot (\vec{a}_2 \times \vec{a}_3)} \tag{A.3}$$

Die approbierte gedruckte Originalversion dieser Diplomarbeit ist an der TU Wien Bibliothek verfügbar
The approved original version of this thesis is available in print at TU Wien Bibliothek.
TU WIEN Bibliothek Your knowledge hub